NAVAL POSTGRADUATE SCHOOL

MONTEREY, CALIFORNIA

THESIS

MODELING NONLINEAR WAVE-INDUCED LOADS ON A SUBMERGED BODY

by

Mehmet Bahadir

June 2022

Thesis Advisor: Joseph T. Klamo
Second Reader: Clifford A. Whitcomb

THIS PAGE INTENTIONALLY LEFT BLANK

REPORT DOCUMENTATION PAGE			*Form Approved OMB No. 0704-0188*

1. AGENCY USE ONLY *(Leave blank)*	**2. REPORT DATE** June 2022	**3. REPORT TYPE AND DATES COVERED** Master's thesis

4. TITLE AND SUBTITLE
MODELING NONLINEAR WAVE-INDUCED LOADS ON A SUBMERGED BODY

5. FUNDING NUMBERS

6. AUTHOR(S) Mehmet Bahadir

7. PERFORMING ORGANIZATION NAME(S) AND ADDRESS(ES)
Naval Postgraduate School
Monterey, CA 93943-5000

8. PERFORMING ORGANIZATION REPORT NUMBER

9. SPONSORING / MONITORING AGENCY NAME(S) AND ADDRESS(ES)
N/A

10. SPONSORING / MONITORING AGENCY REPORT NUMBER

11. SUPPLEMENTARY NOTES The views expressed in this thesis are those of the author and do not reflect the official policy or position of the Department of Defense or the U.S. Government.

12a. DISTRIBUTION / AVAILABILITY STATEMENT
Approved for public release. Distribution is unlimited.

12b. DISTRIBUTION CODE
A

13. ABSTRACT (maximum 200 words)

The wave-induced linear loads on a submerged underwater vehicle are well understood for canonical shapes. An analytical solution even exists for arbitrary body-of-revolution shapes. Wave-induced nonlinear loads, on the other hand, are not nearly as well predicted. Assuming inviscid flow, complicated potential functions provide solutions for the nonlinear loads but require large computer resources to solve. This thesis investigates wave-induced nonlinear loads on a fully submerged cylindrical body in a wave field consisting of two superimposed regular waves. A dynamic verification of a load cell was first performed to ensure that the small loads could be accurately measured. The load cell dynamic measurement error was calculated at less than 8%. Then, through experimental measurements, the study empirically developed a contour map of these nonlinear loads. These loads are presented as functions of the wave height and wavelength of each of the two underlying waves. By covering a large parameter space of wavelengths and looking at two different wave heights, this thesis created contour maps of the nonlinear loads at a fine wavelength resolution and demonstrated how to collapse the nonlinear loads for any wave height. These contour maps can be used during the design process with model-based systems engineering tools for predicting the loads on an underwater vehicle to ensure it meets maneuvering and stability requirements.

14. SUBJECT TERMS
dynamic validation, nonlinear wave-induced loads, wave effects, fully submerged underwater vehicle, wave-induced load prediction, model-based systems engineering

15. NUMBER OF PAGES
137

16. PRICE CODE

17. SECURITY CLASSIFICATION OF REPORT	**18. SECURITY CLASSIFICATION OF THIS PAGE**	**19. SECURITY CLASSIFICATION OF ABSTRACT**	**20. LIMITATION OF ABSTRACT**
Unclassified	Unclassified	Unclassified	UU

NSN 7540-01-280-5500

Standard Form 298 (Rev. 2-89)
Prescribed by ANSI Std. 239-18

THIS PAGE INTENTIONALLY LEFT BLANK

Approved for public release. Distribution is unlimited.

MODELING NONLINEAR WAVE-INDUCED LOADS ON A SUBMERGED BODY

Mehmet Bahadir
Captain, United States Army
BS, Sakarya University, Adapazari/Turkey, 2003

Submitted in partial fulfillment of the
requirements for the degree of

MASTER OF SCIENCE IN SYSTEMS ENGINEERING

from the

NAVAL POSTGRADUATE SCHOOL
June 2022

Approved by: Joseph T. Klamo
Advisor

Clifford A. Whitcomb
Second Reader

Oleg A. Yakimenko
Chair, Department of Systems Engineering

THIS PAGE INTENTIONALLY LEFT BLANK

ABSTRACT

The wave-induced linear loads on a submerged underwater vehicle are well understood for canonical shapes. An analytical solution even exists for arbitrary body-of-revolution shapes. Wave-induced nonlinear loads, on the other hand, are not nearly as well predicted. Assuming inviscid flow, complicated potential functions provide solutions for the nonlinear loads but require large computer resources to solve. This thesis investigates wave-induced nonlinear loads on a fully submerged cylindrical body in a wave field consisting of two superimposed regular waves. A dynamic verification of a load cell was first performed to ensure that the small loads could be accurately measured. The load cell dynamic measurement error was calculated at less than 8%. Then, through experimental measurements, the study empirically develops a contour map of these nonlinear loads. These loads are presented as functions of the wave height and wavelength of each of the two underlying waves. By covering a large parameter space of wavelengths and looking at two different wave heights, this thesis created contour maps of the nonlinear loads at a fine wavelength resolution and demonstrated how to collapse the nonlinear loads for any wave height. These contour maps can be used during the design process with model-based systems engineering tools for predicting the loads on an underwater vehicle to ensure it meets maneuvering and stability requirements.

THIS PAGE INTENTIONALLY LEFT BLANK

Table of Contents

THIS PAGE INTENTIONALLY LEFT BLANK

List of Figures

List of Tables

THIS PAGE INTENTIONALLY LEFT BLANK

List of Acronyms and Abbreviations

AMTI	Advanced Mechanical Technology INC.
CFD	computational fluid dynamics
CI	confidence interval
DAQ	data acquisition
DOD	Department of Defense
gm	grams
GUI	Graphical User Interface
Hz	hertz
in.	inches
lbs	pounds
MBSE	model-based systems engineering
NI	National Instrument
NIST	National Institute of Standards and Technology
NPS	Naval Postgraduate School
sec	second
US	United States
USA	United States Army
USN	United States Navy
UUVs	unmanned underwater vehicles

THIS PAGE INTENTIONALLY LEFT BLANK

Acknowledgments

I would like to express my most profound appreciation to Dr. Klamo for his undivided support, invaluable guidance, and pearls of wisdom, and to thank Prof Whitcomb for his willingness to be a second reader to make this research better. I am also extremely grateful to all of the professors and staff in the Systems Engineering department at the Naval Postgraduate School. I would not be at this point without their exemplary and unending support.

Most importantly, I would like to thank my loving and incredibly supportive wife, Gulsah, and my wonderful son, Kevin, who always believe in me.

Lastly, I would like to thank my mother, Kadriye, my sister, Fulya, and my brother, Fatih, whose love is always with me.

THIS PAGE INTENTIONALLY LEFT BLANK

CHAPTER 1:
Introduction

1.1 Background

When underwater vehicles operate deeply submerged, they are at a depth that makes the influence from waves on the surface negligible. As such, they do not experience wave-induced loads. However, when underwater vehicles perform operations such as snorting a diesel engine, using the periscope, and traveling through shallow seaways, they must operate near the surface and consequently experience wave-induced loads. The wave-induced loads can limit the underwater vehicle's operational capabilities and effectiveness when near the surface. This is because wave-induced loads can cause undesired roll, yaw, and pitch movements along with difficulty in maintaining a consistent depth when near the surface.

Wave-induced loads have a linear and nonlinear component caused by each underlying wave component in an irregular seaway. Each wave component individually produces a linear force. These linear loads occur at the encounter frequency of each wave. This means that although these loads are larger than the nonlinear ones, they occur at a much shorter time scale. This time scale is usually too short for large underwater vehicles to respond to, so they are more of a concern for smaller underwater vehicles. Nonlinear loads result from interactions between waves, including a wave with itself, and occur at the sum and difference of the frequencies of the interacting waves. Therefore, we can get a mean (0 Hz frequency) nonlinear load and a double harmonic (twice the encounter frequency) nonlinear load from waves interacting with themselves. We also get a nonlinear load at every difference and sum combination of frequencies of all the underlying waves in the seaway. These loads are much smaller than the linear ones but happen over much longer time scales; waves with very nearly the same frequency will produce a nonlinear force that has an extremely long period. Therefore, under the right conditions, these loads are a significant issue for larger underwater vehicles since the response time of their control systems is slow. These loads are usually negligible for smaller vehicles and their control systems can usually respond fast enough to deal with them.

1.2 Motivation

The understanding of linear and nonlinear wave-induced loads on underwater vehicles, and their effects on vehicle performance, will allow future vehicle design to address these loads early in the design process and increase the underwater vehicles' operational dependability and effectiveness. This would allow underwater vehicles to be fully capable of conducting operations such as snorting and periscoping near the surface. When using the periscope or snorting near the surface at certain depths, underwater vehicles can experience wave-induced forces and moments due to complex sea states that result in a suction effect that draws the underwater vehicles to the surface. This can increase the likelihood of the vehicle broaching the surface and being detected [1].

Historically, there has been less focus on the nonlinear wave-induced loads. Currently, linear loads are better understood, and the parameters that influence the loads are known. The loads are modeled accurately enough, including the existence of analytical solutions for body-of-revolution shapes for most engineering purposes. However, nonlinear loads are less understood. Predicting them requires solving complicated potential functions from the inviscid flow. These solutions require great computing efforts.

1.3 Previous Work

There are experimental and numerical studies conducted in the past to investigate linear and nonlinear wave-induced forces and moments on fully submerged structures. This section first summarizes experimental investigations and then numerical studies.

Crossland [1] performed a series of experimental tests to understand wave-induced loads effects on a semi-captive underwater vehicle with a variety of speeds, directions, and sea states. As a result, Crossland [1] demonstrated that the understanding of these horizontal and vertical wave-induced loads may again influence the design of future underwater vehicles.

Khalil's [2] experimental research focused on two-dimensional wave-induced loads on long horizontal cylinder structures submerged parallel to waves in a towing tank. The experiments were performed by using a wavemaker creating sinusoidal waves with lengths of 1.57 and 3.14 m traveling over circular and rectangular cylinders distinctly to predict the impact of the these different geometrical shapes on the wave-induced loads [2]. During these

experiments, the horizontal and vertical wave-induced forces exerted on the submerged cylinders at different depths were measured using a multi-component load cell and then evaluated and compared to existing data in previous studies. Khalil's main finding is that the development of nonlinear wave forces is predominantly caused by waves breaking behind a submerged cylinder near the surface. Wave-breaking is responsible for the negative drifting force acting on a submerged cylinder as this drifting force seems to disappear when the submergence depth is increased [2].

Whitmer's [3] study is an experimental one for predicting wave-induced forces and moments on a submerged body near the surface. In his study, the applicability of linear superposition is investigated to estimate the wave-induced forces and moments on a submerged structure [3]. The author studied the ability to predict the individual linear drag and vertical forces, along with the pitching moment, in a complex two-component seaway. By solving Cummins' equations 1.1, 1.2, and 1.3 and comparing them to the experimental measurements, the study examined their accuracy in general.

$$F_x = -\frac{\pi}{2}\rho g A_o h\left(\frac{1}{\lambda^*}\right)e^{-2\pi H'} b_0 \cos\left(\omega_e t\right) \tag{1.1}$$

$$F_z = -\pi\rho g A_o h\left(\frac{1}{\lambda^*}\right)e^{-2\pi H'} b_0 \sin\left(\omega_e t\right) \tag{1.2}$$

$$M_y = -\frac{\pi}{2}\rho g A_o L h\left(\frac{1}{\lambda^*}\right)e^{-2\pi H'} a_1 \cos\left(\omega_e t\right) \tag{1.3}$$

Expanded discussions about Cummins's equations on linear wave-induced forces and moments can be found in Cummins' [4], Whitmer's [3], [5] and Hermsen's [6] studies. Whitmer [3] concluded that for the studied wave heights and frequencies, that linear superposition is a viable analysis to predict the wave-induced forces and moments on shallowly submerged structures.

Klamo et al. [7] and Turner et al. [8] conducted experimental studies to investigate the wave-induced loads on a fully submerged body by focusing on surge force, heave force, and pitch moment in a towing tank. Their research concentrated on modeling the linear first-order

wave-induced forces on the body while evaluating the accuracy of an analytical solution. The studies identified the theoretical assumptions in the analytical solution and then studied the importance of these assumptions during an accuracy assessment. They used equations that Cummins [4] derived for "an arbitrary, slender, body-of-revolution submerged under a monochromatic wave" to investigate the first-order linear surge force, heave force, and pitch moment. Both studies only looked at zero-speed instances and waves traveling down the longitudinal axis of the body. Their research concluded that when the wavelengths are greater than the body length, the analytical solution can precisely forecast the wave-induced heave and surge forces. They found that the analytical pitch moment solution has the least level of precision.

A subsequent study from Klamo et al. [9] experimentally evaluated the impact of the cross-sectional geometry on the magnitude and phase of wave-induced linear loads on an underwater vehicle near the surface. Their experimental research focused on measuring the wave-induced loads and moments on three different types of geometrical cross-sectional bodies with hemispheric end caps. These bodies, a square cross-sectional cylinder, a horizontal rectangle, and a vertical rectangle, had aspect ratios of 1, 4, and 1/4, respectively. They performed the experimental tests in a towing tank with wave-making capability. Their investigation concluded that simple theoretical predictions regarding the influence of the aspect ratio of a rectangle on the linear heave force did not agree with the experimental findings. They also discovered that the loads were proportional to the rectangle's aspect ratio [9].

Cho et al. [10] conducted constrained model experiments to analyze an X-plane submarine's maneuverability and agility. To determine the submarine's maneuvering coefficients, they conducted captive model experiments with various mechanisms, including horizontal and vertical motion mechanisms, and then used the maneuvering coefficients acquired from the experimental measurements to execute maneuvering simulations. Cho et al. [10] demonstrated that CFD simulations may be used to produce reliable X-plane submarine movement coefficients. These coefficients can then be used in maneuvering simulations and algorithms to enhance future underwater vehicle designs.

One of the numerical studies was performed by Hayatdavoodi and Ertekin who conducted a parametric analysis using "the nonlinear and unsteady Green-Naghdi equations (Level I)" to

approximate the nonlinear wave-induced loads exerted on the bottom and top of a horizontal and stationary flat plate submerged in shallow water [11]. The authors first discussed the theory that is applicable to the nonlinear wave-induced forces on a submerged structure and then explained the application of the G-N theory to the nonlinear wave-induced forces on submerged structures in shallow water. The definition of the components used in the Level I equations 1.4 and 1.5 and can be found in Hayatdavoodi and Ertekin [11]. The "solitary and periodic solutions" example of the following G-N equations (Level I) are addressed in Ertekin [12]. There are also three dimensional G-N equations discussed in Ertekin et al. [13].

$$\eta_{,t} + (h + \eta - \alpha)u_x = \alpha_t \tag{1.4}$$

$$\dot{u} + g\eta_x + \frac{\hat{p}_x}{\rho} = -\frac{1}{6}[2\eta + \alpha]_x\ddot{\alpha} + [4\eta - \alpha]_x\ddot{\eta} + (h + \eta - \alpha)[\ddot{\alpha} + 2\ddot{\eta}]_x \tag{1.5}$$

For this study, the domain is divided into four regions to examine the application of the G-N equations in each one [11]. Hayatdavoodi and Ertekin developed Figure 1.1 to address the entire domain.

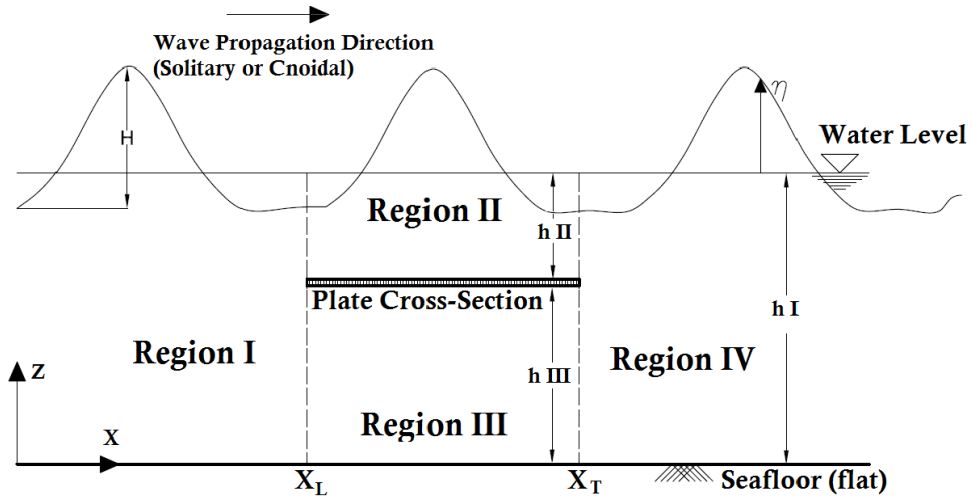

Figure 1.1. A diagram of nonlinear waves traveling over a horizontally submerged plate through four regions. Source: [11].

Hayatdavoodi and Ertekin's numerical study proves that the nonlinear wave-induced forces on the bottom and the top of the submerged flat plate can be calculated by solving the G-N equations. The significance of this study can be supplemental to a variety of experimental

research for investigating nonlinear forces on shallowly submerged structures.

1.4 Objective and Significance

The main objective of this thesis is to generate a mathematical model in the form of a contour map for predicting the nonlinear components of wave-induced loads on a fully submerged body. Three different loads, heave force, surge force, and pitching moment, are measured and studied as functions of the wave height and wavelength of the two underlying waves making up the wave environment. This thesis also aims to achieve three sub-objectives: (1) developing a map that has a fine resolution of wave 1 and wave 2 wavelengths; (2) developing a better understanding of uncertainty in the map by performing more repeat test conditions; (3) being able to examine the effect of wave height on the map. This thesis builds on Hermsen's [6] research and expands the parameter space.

The significance of this study is to support the model-based systems engineering tools used to design future underwater vehicles to ensure the vehicles' performance and mission effectiveness meet the requirements.

The contour map mathematical model developed in this thesis can be used to capture how the nonlinear components vary as a function of the specific wave environment experienced by the fully submerged vehicle. It can also be used with a model-based systems engineering (MBSE) approach for future designs in both civilian and defense communities. Overall, this study will be beneficial to the Navy regarding its use of underwater vehicles, the Department of Defense (DOD), and the other civilian engineering communities. The results will provide a better understanding of the nonlinear forces and moments that can affect the underwater vehicles' performance and mission effectiveness.

CHAPTER 2:
Instrumentation and Sensors

This chapter introduces the instruments and sensors used for the dynamic validation and experimental test runs. There were two different types of sensors used to collect data during testing and a number of instruments to power the sensors and collect the signals from them. This chapter will first describe sensors and then the supporting instrumentation. In the end, there are graphical representations showing the overall components assembly.

2.1 Load Cell

This study used an Advanced Mechanical Technology Inc. (AMTI) UDW3 waterproof strain-gauge load cell to measure the three forces and moments of interest on the body. The load cell is oil-filled, and its structure is made out of heat-treated stainless steel. It has a built-in pressure bladder that balances the load cell's internal and exterior pressures. Therefore, even though it is submerged to depth, precise force and moment readings are possible. The load cell can be attached to other hardware using the four 1/4"-20 threaded holes on either end of the device. Figure 2.1 depicts a picture of a UDW3 load cell. Figure 2.2 shows a sketch of UDW3 load cell dimensions. More information about the load cells with a variety of load capacities can be found on the AMTI's website [14].

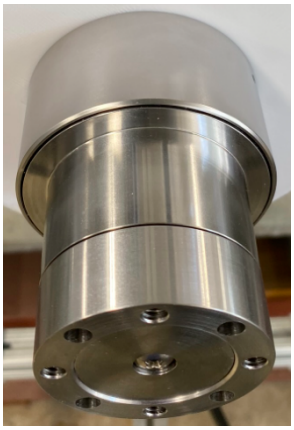

Figure 2.1. UDW3 load cell.

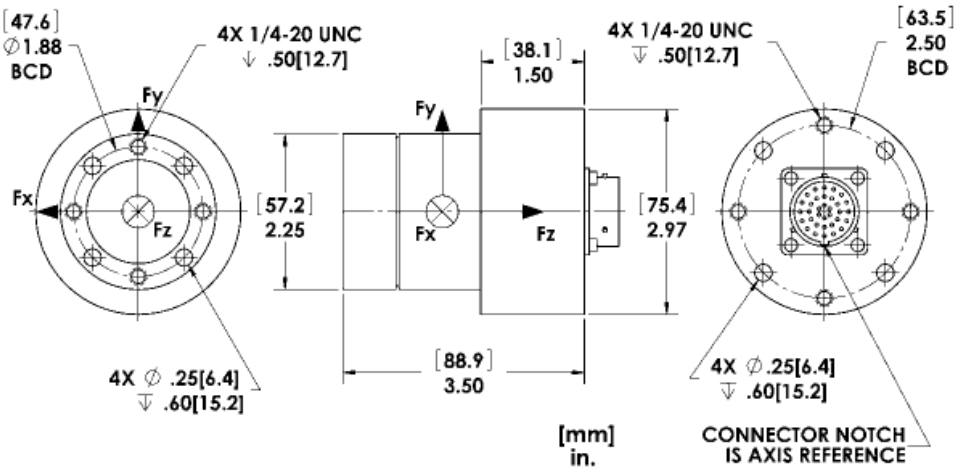

Figure 2.2. UDW3 load cell dimensions. Source: [14].

2.2 Senix Accoustic Probes

The experimental setup used ultrasonic probes to make two different distance measurements. Ultrasonic probes work by sending out an acoustic pulse and then measuring the time to return for the reflected pulse. This time is turned into a distance with the assumption that the medium was air. Specifically, we used SENIX ToughSonic 14 probes (model #: TSPC-30S1-485), which have an operating range of 4 inches to 168 inches. Figure 2.3 depicts a ToughSonic 14 probe. The first application of the probes was to measure the wave elevation by pointing four probes down at the water surface from above the towing tank. By removing the measured calm water distance before testing, the distance measured during a test run is converted into the wave elevation. The second application of the probes was to verify the motion of the wavemaker wedge during testing by mounting a single probe above a horizontal bar that moved with the oscillating wedge.

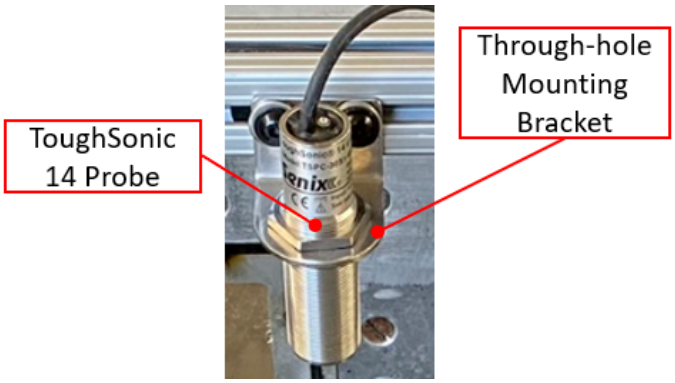

Figure 2.3. ToughSonic 14 probe.

SenixVIEW software is used to configure the sensors. The sensor needs +24 DC power to operate and communicates with a provided terminal board. The terminal board outputs 0 to 10 volts corresponding to the measurement range set for the probe in the software. Figures B.1 – B.5 in Appendix B depict screenshots of the SenixVIEW settings used for all the probes. For probes 1 through 4, which measured wave elevation, they were set with a gain of 1V corresponding to 1 inch. For the wavemaker wedge probe, it was set with a gain of 1V corresponding to 2 inches. Figures 2.4 and 2.5 display the location of the wedge probe and the probes 1 through 4, respectively.

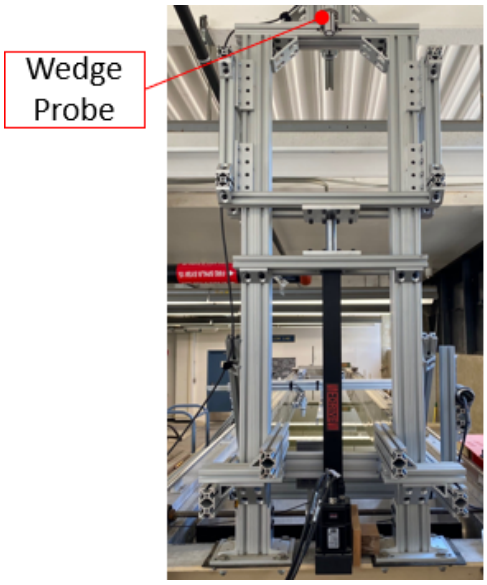

Figure 2.4. Location of wedge probe.

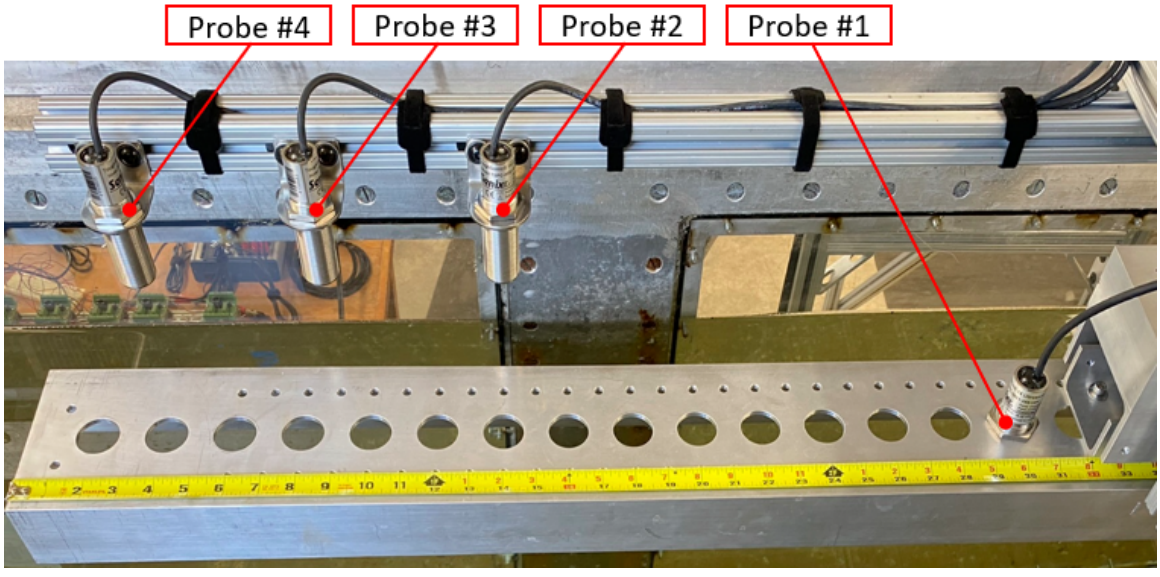

Figure 2.5. Locations of experimental measurement wave probes.

Table 2.1. Settings for each of the five probes.

Probe Identification	Minimum Distance (inch)	Maximum Distance (inch)	Output Range (volts)	Gain (inch/volt)
wedge probe	8	28	0 – 10	−2
wave probes 1-4	8	18	0 – 10	−1

2.3 Signal Conditioner

The AMTI Gen 5 is an amplifier providing the capability to independently configure the six load cell channels. The user sets the desired excitation voltages and gains for each channel by using the provided AMTI software. Due to limitations with the number of pins on the waterproof connector, the excitation voltage had to be the same across all 6 channels, but the gains could be different. The Gen 5 amplifier also compensates for the cable length.

For this thesis, the amplifier received the load cell output signals via a connector cable. It processed the signals according to the user-selected excitation voltage levels and gains and then provided them as analog output voltages. Figure 2.6 displays a picture of the AMTI Gen 5 amplifier used for this study.

Figure 2.6. AMTI Gen 5 Amplifier used for the dynamic validation and experimental measurements.

2.4 Data Acquisition (DAQ) Instrument

This thesis used an NI USB-6363 DAQ instrument board to discretely sample the analog signals from the Gen 5 signal conditioner at the requested sampling rate. Figure 2.7 shows the NI USB-6363 DAQ instrument used in this study. The instrument was connected to the computer via a USB cable during the dynamic validation and the experimental measurements.

Figure 2.7. NI USB-6363 DAQ instrument used for the dynamic validation and experimental measurements.

2.5 Power Supplies

DC power for this research was supplied by a Keysight E3631A programmable power unit. It supplies the +24V DC power to the five Senix probes through the probe's terminal circuit cards. Figure 2.8(a) depicts a picture of the Keysight power unit.

A TRIPP-LITE Line Conditioner LC2400 AC power unit was used to supply regulated, noise controlled power to the AMTI Gen 5 signal conditioner, the NI USB-6363 DAQ Instrument, and the Keysight power unit. It was also used to protect the components from excessive voltages and power surges. Figure 2.8(b) shows the TRIPP-LITE Line Conditioner unit used.

(a) DC power supply unit

(b) AC power supply unit

Figure 2.8. Power supply units.

2.6 Component Assembly

Figure 2.9 is a diagram of all components used in the experimental setup. It helps visualize the relationships of the overall components in this thesis. The layout of the dynamic validation system's components are discussed in the dynamic validation setup section in the next chapter. Figure 2.10 is a photo showing the data collection station setup portion of Figure 2.9.

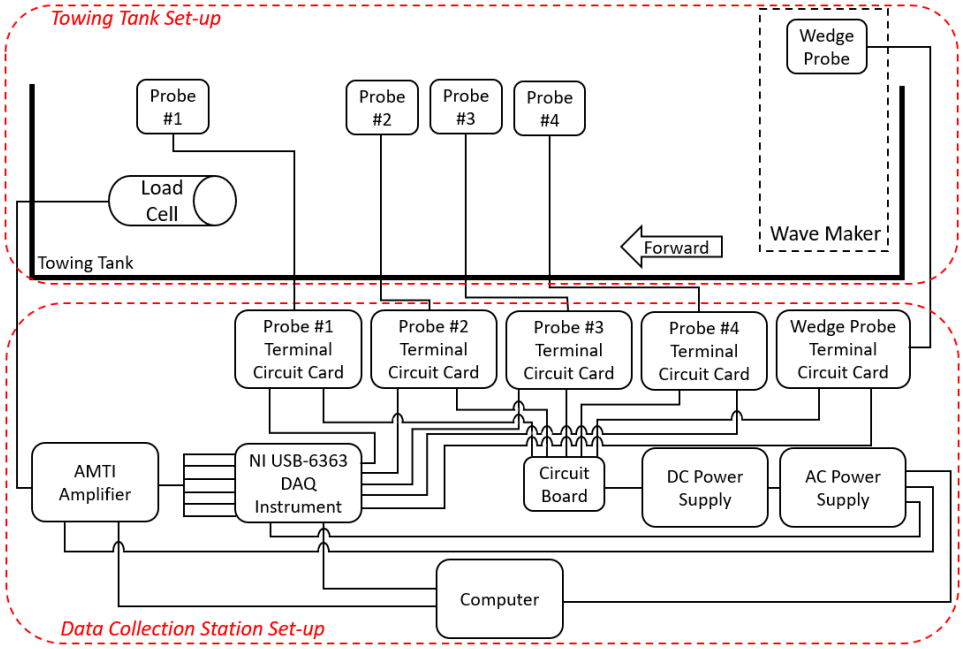

Figure 2.9. A block diagram of overall components and their physical relationships for experimental measurements setup.

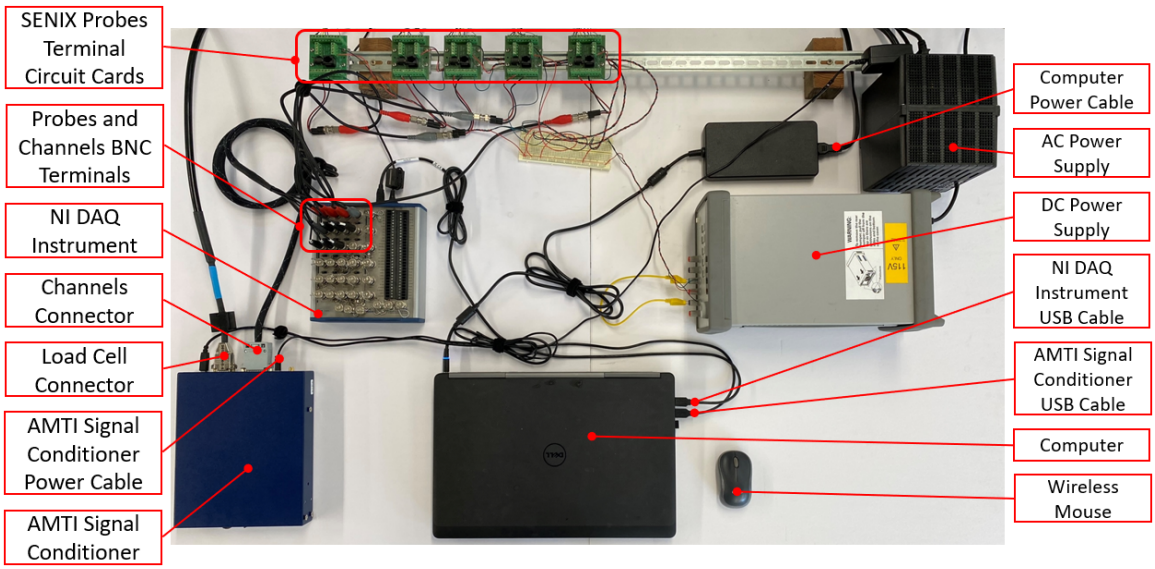

Figure 2.10. Overall components assembly for the experimental measurements.

CHAPTER 3:
Facilities and Equipment

This chapter discusses the testing facility and equipment used for this thesis. The design of the dynamic calibration are first discussed. Then the towing tank and its components are addressed. Lastly, the testing fixture and the cylindrical body are explained in this chapter.

3.1 Dynamic Validation Setup

The data collection station setup for the dynamic validation is a simplified version of the experimental data collection station setup shown in the previous chapter. However, the dynamic validation assembly is different than the experimental testing fixture. The dynamic validation's overall components and their physical relationships are shown in Figure 3.1. More discussion of the whole assembly can be found toward the end of this section.

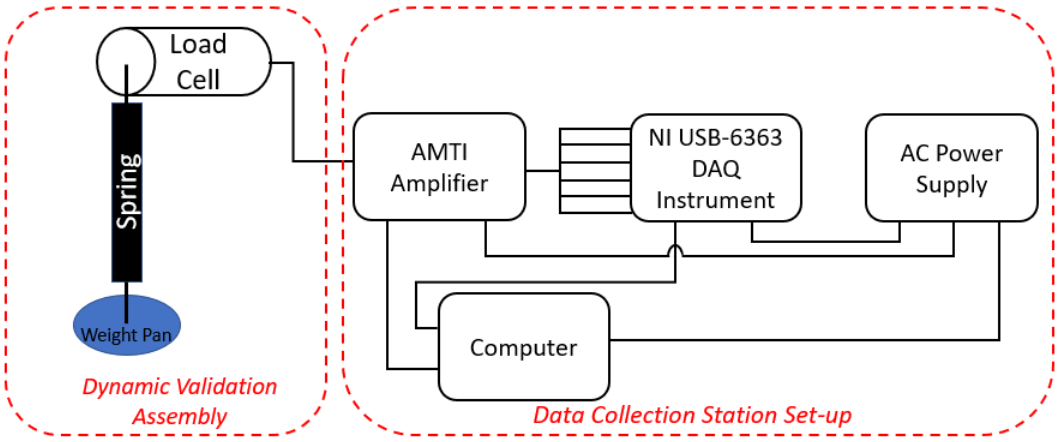

Figure 3.1. A block diagram of overall components and their physical relationships for dynamic validation setup.

A picture of the fully assembled dynamic validation system is shown in Figure 3.2. The dynamic validation assembly was installed on an 80/20 aluminum structure. The connector side adapter of the load cell attached the validation assembly to the 80/20 structure. On the other side of the load cell, a very soft spring was hanging from the payload side adapter.

A weight pan was attached at the other end of the spring to hold the validation weights. Ideally, the validation setup would involve the load cell being rotated along its long axis with an axial bearing attached to the payload side. A weight hanging off the bearing would stay fixed. The load cell measurement origin would rotate with the load cell so that the applied load would be transferred between the two orthogonal measurement directions and be dynamic. The issue with that design is that we need a slip-ring for the cable connection, or else the cable will eventually get twisted.

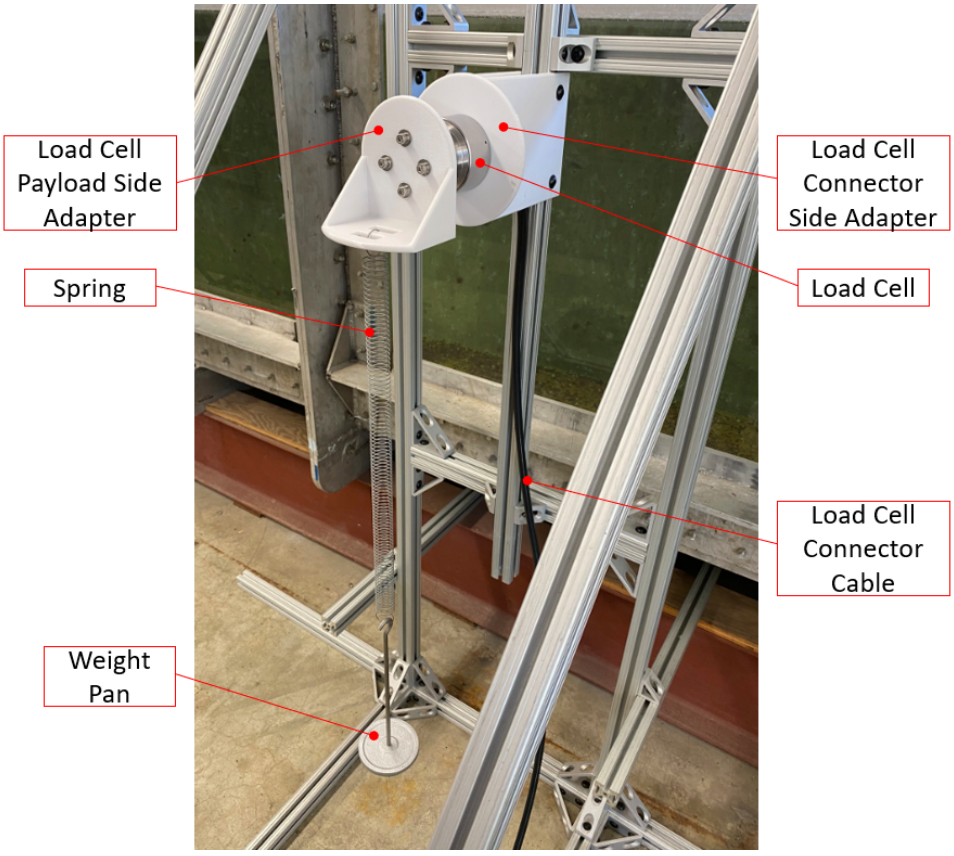

Figure 3.2. Fully assembled system for dynamic validation.

The thesis required that the load cell be validated under dynamic loading to ensure the small nonlinear loads could be accurately measured. Traditional validations and accuracy assessments were done on static loads looking at mean values of the collected load cell signal. However, we were interested in dynamic loading, since wave-induced loads are periodic.

Therefore, this study needed to look at the accuracy of the load cell when measuring a dynamic load and our ability to determine the amplitude of the signal.

For the dynamic validation design, a mass-spring system was used. The payload side adapter attached to the load cell and had a spring hanging perpendicular to the ground. There was a weight pan at the end of the spring, which could hold different weights. When the weights were removed, the spring's displaced length increased and decreased periodically, creating oscillatory forces on the load cell. We wanted a very soft spring, with corresponding low damping, to create an adequate oscillation for a sufficient amount of time. More details about the assembly are discussed at the end of this section.

Two adapters, the connector side and the payload side, were used for the dynamic validation assembly. They were printed using rapid prototyping technology and are made of polycarbonate. The material provided strength and durability for carrying the weight of the load cell, which is significant since it is made of stainless steel, and the validation weights on the weighing pan. Figures 3.3 and 3.4 show pictures of the connector side and the payload side adapters, respectively. Also, the engineering drawings of both adapters are shown in Appendix A (Figures A.1 and A.2, respectively).

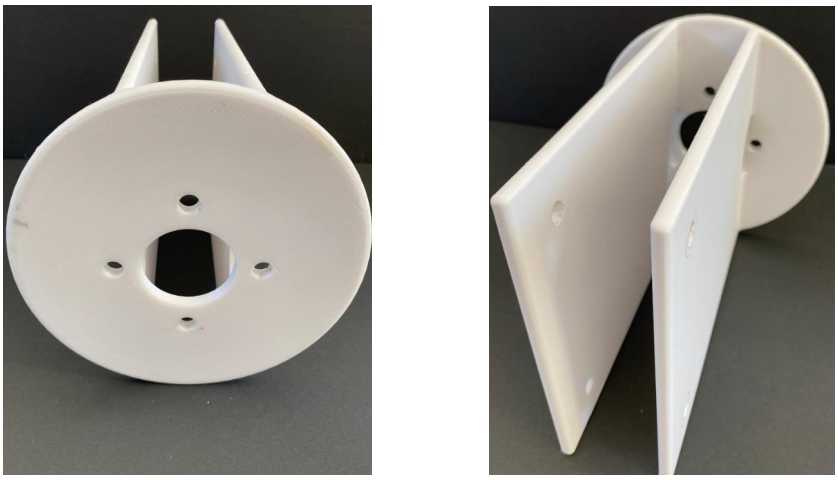

(a) Front view (b) Rear view

Figure 3.3. Connector side adapter of the load cell.

(a) Front view (b) Side view

Figure 3.4. Payload side adapter of the load cell.

For the validation weights, we used National Institute of Standards and Technology (NIST) calibrated weights for 1 lbs and 0.5 lbs, and made custom weights for the lighter weights. These light weights were made using some wire and a set of PASCO weights. Figure 3.5 shows a picture of the validation weights. The exact weight was achieved by using the appropriate length of wire and confirmed using digital scale. The loop at the top of the wire served as a holder that allowed quick removal of the weight from the weight pan without creating any unwanted disturbances to the spring.

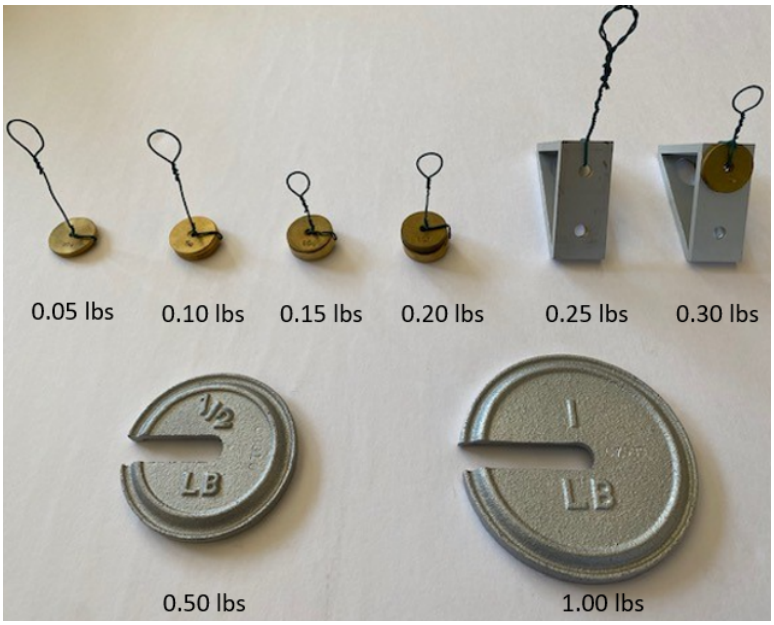

Figure 3.5. Dynamic validation weights.

Table 3.1. Dynamic validation weights.

lbs	gm
0.05	22.680
0.10	45.359
0.15	68.389
0.20	90.719
0.25	113.398
0.30	136.078
0.50	226.796
1.00	453.592

3.2 Towing Tank with Wavemaker

This study used the towing tank with wavemaking capability at NPS to perform the experiments. The 3 ft (W) x 4 ft (H) x 36 ft (L) towing tank is constructed with aluminum material and has eight identical see-through Plexiglas panels installed to observe activities inside the tank. More information about the towing tank can be found in [15].

The wavemaker is positioned at one end of the towing tank. It is constructed using 80/20 aluminum extrusions, teflon slide rollers, an electrical motor, a wedge, an actuator, and a Senix probe. The wavemaker is controlled by custom software. The desired frequency and amplitude of the wavemaker wedge are manually entered into the software. These commands are then sent to the electrical motor to move the vertical actuator to create waves by moving the wedge upward and downward inside the tank. Figure 3.6 shows a front and rear view of the wavemaker. Information about the wavemaker's dimensions can be found in Whitmer's [3] study.

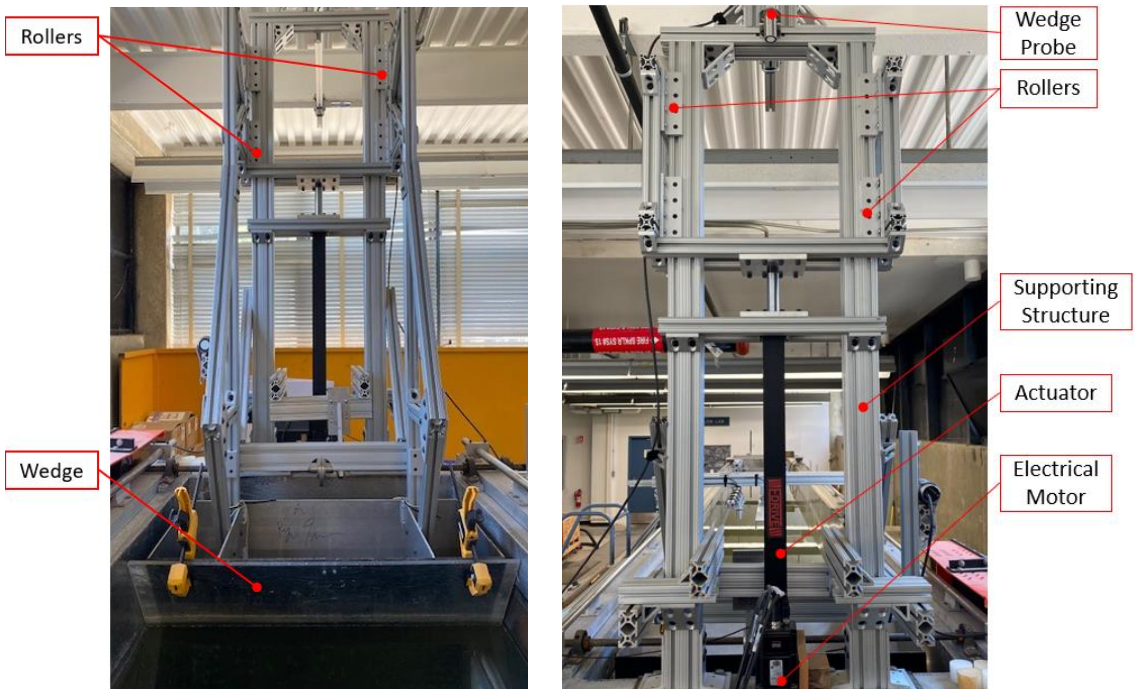

(a) Front view (b) Rear view

Figure 3.6. Wavemaker used for the experimental measurements.

A wave dampening beach is located at the other end of the tank to minimize any wave reflections that would travel back down the tank. The beach is constructed using a pair of perforated acrylic sheets with holes in staggered rows. These holes absorb the waves and prevent them from traveling back down the tank. The designed installation was 12 degrees. After installing the beach, the actual angle was measured as 12.4 degrees. The dimensions of the dampening beach are shown in Figure 3.7. More details about the beach can also be found in Hermsen's [6] and Turner's [16] studies.

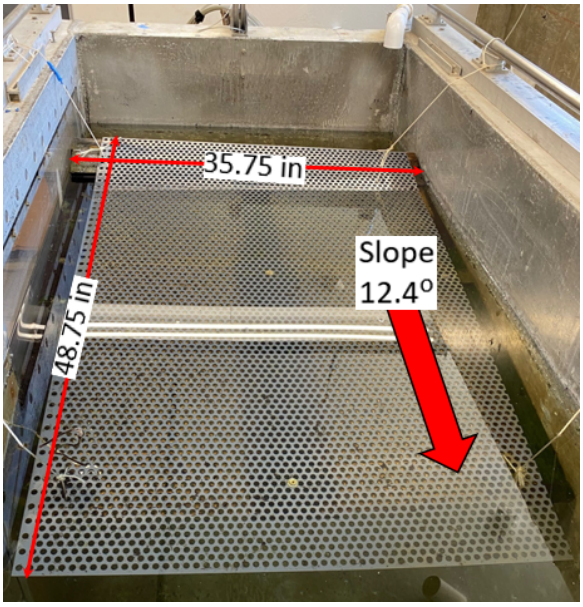

Figure 3.7. Wave-dampening beach at the end of the towing tank.

A stationary bridge, composed of 80/20 aluminum extrusions and mounting brackets, provided a structure to hang the testing fixture. The bridge has two vertical structures, one on each side of the towing tank, as shown in Figure 3.8. The bridge was used to isolate the test fixture and cylindrical body from the towing tank itself. The wavemaker is attached directly to the tank and creates vibrations within the tank structure itself when operating. These vibrations would be manifested as noise in the recorded signal if the bridge was not utilized.

(a) Left side (b) Right side

Figure 3.8. Left and right side of the vertical support structures for the stationary bridge over the towing tank.

3.3 Testing Fixture

There are two different load cell adapters used in the testing fixture. Figure 3.9 shows a picture of both adapters attached to the load cell. The adapter on the left connects the horizontal sting to the load cell on the connector side. This adapter is hollow, like the horizontal sting, to allow the power and signal cable to pass through and be connected to the load cell. The adapter on the right secures the load cell to the cylindrical test body with screws and contains recessed grooves to allow water to move past when submerging the body. Hermsen [6] previously designed both adapters for use with her thesis work and fabricated them out of polycarbonate using rapid prototyping technology.

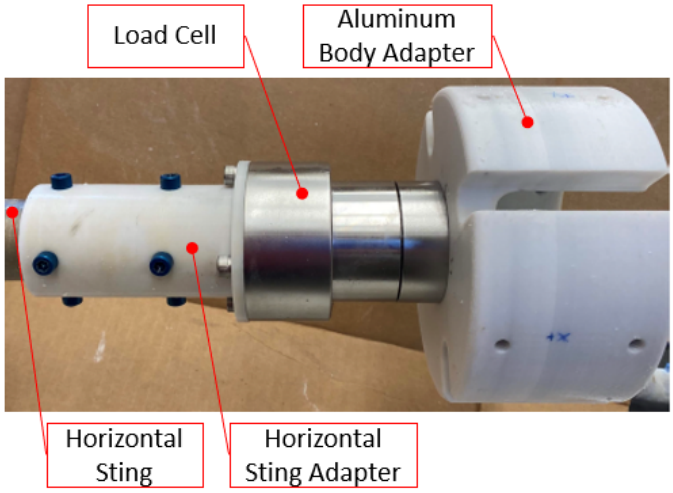

Figure 3.9. Load cell testing assembly inside the aluminum body. (Adapted from [6]).

There were three different components attached to the stationary bridge. A U-channel, that held the sting mechanism and cylindrical body, was attached to the stationary bridge using the two aluminum stiffeners. An 80/20 extrusion bar was also attached to the stationary bridge. Probes 2 - 4 were held by this bar ahead of the bow of the body to measure the incoming wave elevation profile. Finally, to help stabilize the vertical portion of the sting and prevent vibration during wave propagation, a stabilizing structure was attached to the stationary bridge and vertical sting.

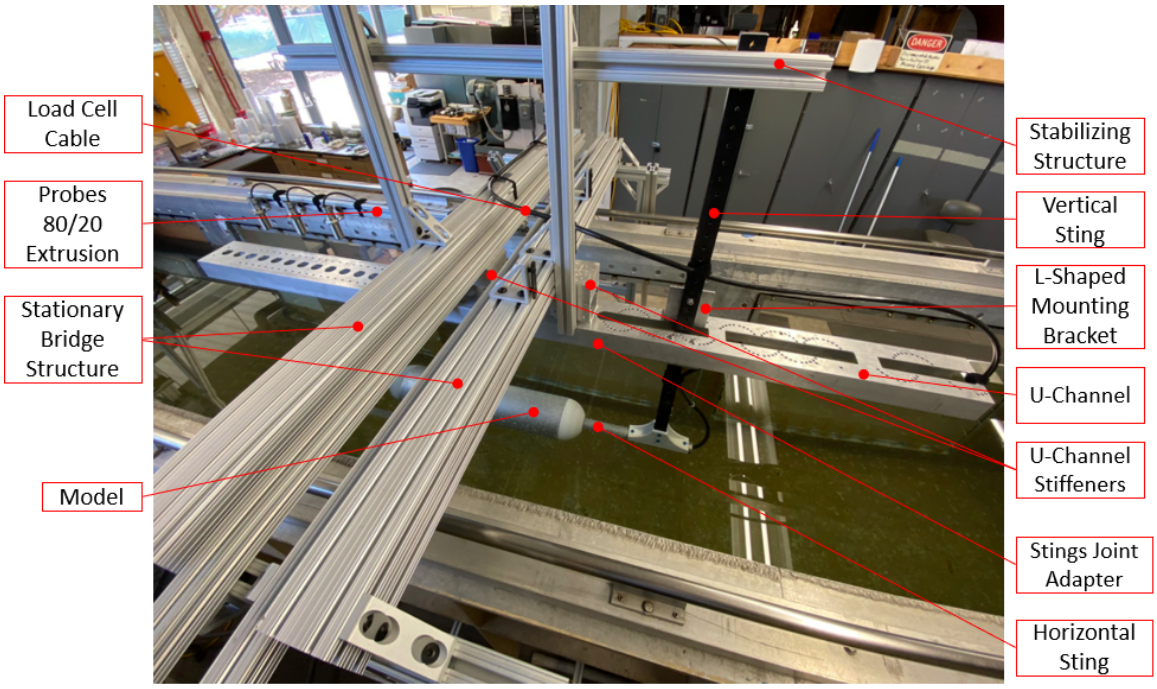

Figure 3.10. Fully assembled testing fixture for the experimental test runs.

The fully assembled vertical and horizontal stings are shown in Figure 3.10. The 46-inch vertical aluminum sting is a 1 inch by 1.5 inches anodized aluminum bar. It provides support by carrying the whole weight of the cylindrical body while submerged in the water. It has holes in increments of 1 inch. These holes allow for adjusting the testing depth of the body in the towing tank. The vertical sting attaches to the U-channel via the two L-shaped mounting brackets and the stabilizing structure. The vertical sting is connected to the horizontal sting via a joint adapter with a 90-degree angle. The horizontal sting is a hollow aluminum rod with a 1.5 inch diameter. The hollow horizontal sting was sized to allow the cable that connects to the load cell to pass through. A detailed discussion about the horizontal and vertical stings can be found in Hermsen's [6] study.

The U-channel and the stiffener are supporting elements of the test setup. The U-channel is attached to the stationary bridge via two rectangular block stiffeners. The two stiffeners attach the U-channel to the bottom of the supporting bridge and support the whole testing fixture to prevent it from moving freely and vibrating. Each stiffener is secured on the U-channel by a bolt and a nut shown in Figure 3.11. The U-channel also has holes in

increments of 2 inches along its center line to help locate the placement of the Senix probes measuring the incoming waves. Probe 1 was positioned over the midpoint of the cylinder body using one of these holes.

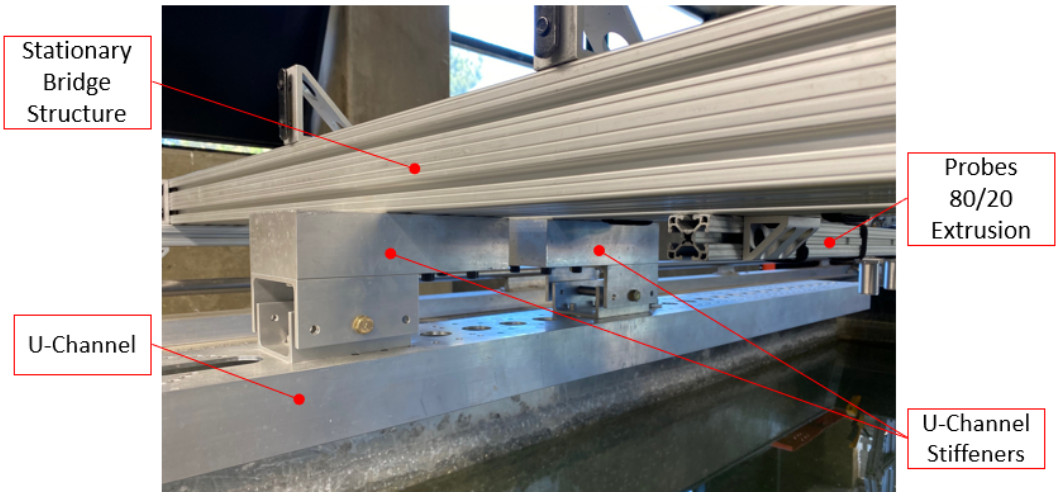

Figure 3.11. Fully assembled stiffeners attaching U-channel to the supporting bridge.

3.4 Body Profile

The cylindrical body shown in Figure 3.12 has a total length of 30 inches, including the end caps, for a length to diameter, L/D, of 5. The body is made from aluminum with a diameter of 6 inches and a thickness of 1/8 inches. The body was a free-flooding design. As such, there were a number of 1/8 inch bleed holes machined in the aluminum body for air to escape while the body was being submerged. The body has two hemispherical end caps that were fabricated by using rapid prototyping technology. The stern end cap has a 2 inch diameter clearance hole to permit the sting to pass through without any contact. The polycarbonate end caps did not need any sanding or surface modifications. They were used "as fabricated."

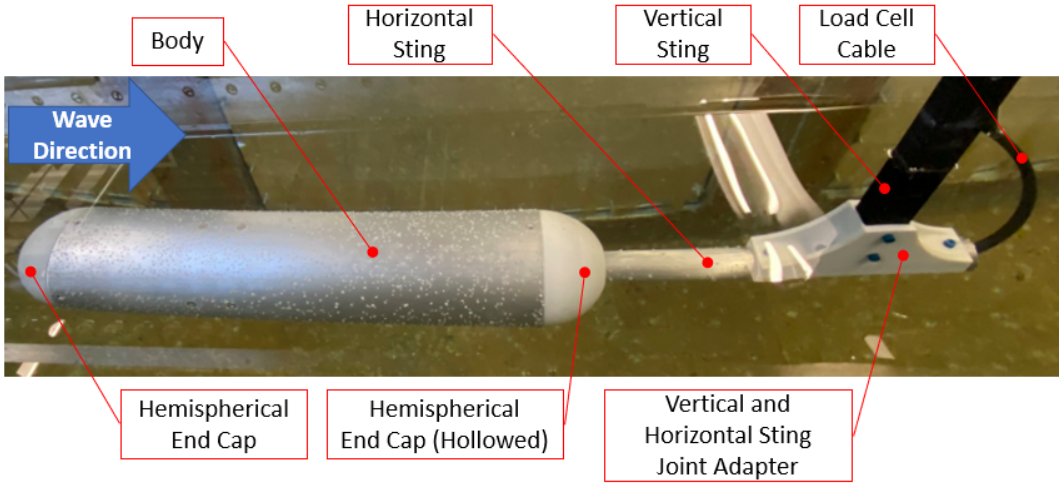

Figure 3.12. Assembled cylindrical body in the towing tank.

CHAPTER 4:
Methodology and Procedures

This chapter explains the dynamic validation process and the experimental measurement steps in detail to understand how the results were produced. It then discusses the sources of uncertainty, including test section blockage, water depth effects for longer waves, wave breaking effects for shorter wavelengths, and the load cell measurement error.

4.1 Dynamic Validation Test Procedure

The setup described in Section 3.1 was used to perform the dynamic validation tests. One load cell was employed, and two different orientations were examined by applying oscillating forces on the F_x and F_y measurement axes. Figure 4.1 shows the two different orientations of the load cell.

Once the components were assembled and installed, the load cell settings were verified using the AMTI software. Table 4.1 displays the AMTI settings for dynamic validation. The cable length of 24.00 feet was also put in the settings to allow for the appropriate compensation by the signal conditioner. Then a poke test on the load cell was performed by using a finger and applying a gentle force to each coordinate of the load cell to ensure that the force signals were on the correct coordinates. The hard zero was then performed on the AMTI software Graphical User Interface (GUI) and the AMTI physical unit.

Table 4.1. AMTI amplifier settings for the dynamic validation.

Configuration Information						
	F_x (lbs)	F_y (lbs)	F_z (lbs)	M_x (in-lbs)	M_y (in-lbs)	M_z (in-lbs)
Platform Capacity	250.00	250.00	500.00	500.00	500.00	250.00
Amplifier Range (max)	20.67	20.89	81.43	15.15	14.90	21.42
Amplifier Range (min)	−20.67	−20.89	−81.43	−15.15	−14.90	−21.42
Analog Outputs (max)	20.00	20.00	83.33	20.00	20.00	20.00
Analog Outputs (min)	−20.00	−20.00	−83.33	−20.00	−20.00	−20.00
Current Configuration						
	F_x	F_y	F_z	M_x	M_y	M_z
Excitation (Volts)	10	10	10	10	10	10
Gain	4000	4000	4000	4000	4000	4000
Zero Set Point (percent)	0.00	0.00	0.00	0.00	0.00	0.00
Analog Sensitivities (mV/lb) (Conditioned)	250.00	250.00	60.00	250.00	250.00	250.00

An actual validation run consisted of creating the oscillating load on the load cell axis of interest. Each weight was placed on the weight pan and after allowing sufficient time for the weight pan to settle, the custom data collection script was started. After 30 seconds elapsed, the weight was quickly removed by hand from the weight pan, and subsequently, the spring and weight pan started oscillating upward and downward. The data collection script was still running and collected this data for an additional 60 seconds. Figure 4.2 shows the weight on the pan just before it was removed. Occasionally, zero files were collected for 30 seconds to ensure the appropriate electrical offset could be removed from the load cell data. These zeros were collected periodically between runs as seen under the "Zero Before Run" column in the test matrix. During data collection, the data collection script also real-time plotted the collected voltage signal from the NI USB-6363 instrument to ensure the quality of the data.

A dynamic validation test matrix shown in Table C.1 in Appendix C was created to validate eight different weights in random order. The dynamic validation data collection test matrix consisted of five runs for each validation weight. The F_y axis was tested first, followed by the F_x axis using the same procedure.

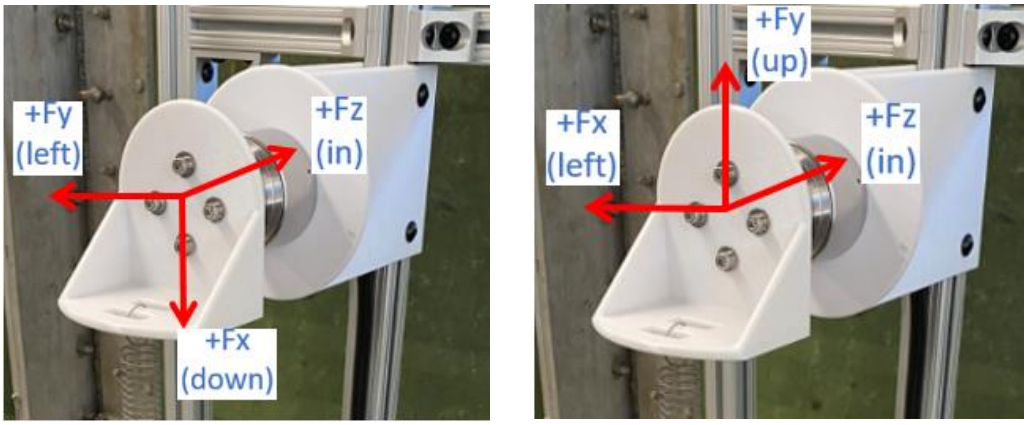

(a) Signal on F_x (b) Signal on F_y

Figure 4.1. Applications of forces on the load cell for the dynamic validation.

Figure 4.2. Removing a weight from the weight pan.

4.2 Wave-Induced Loads Collection Procedure

The experimental setup, described previously in Section. 3.3, was used to perform the testing. The setup used the same load cell that was used for the dynamic validation. This allowed us to ensure that the testing results were collected accurately. The cylindrical body was placed in the towing tank and attached to the testing fixture. Probes 1-4 were installed on the test fixture as discussed previously. Table 4.2 displays the AMTI settings used for measuring the wave-induced loads.

Table 4.2. AMTI amplifier settings for the experimental measurements.

Configuration Information						
	F_x (lbs)	F_y (lbs)	F_z (lbs)	M_x (in-lbs)	M_y (in-lbs)	M_z (in-lbs)
Platform Capacity	250.00	250.00	500.00	500.00	500.00	250.00
Amplifier Range (max)	20.67	20.89	81.43	30.34	14.90	21.42
Amplifier Range (min)	−20.67	−20.89	−81.43	−30.34	−14.90	−21.42
Analog Outputs (max)	20.00	20.00	83.33	33.33	16.67	20.00
Analog Outputs (min)	−20.00	−20.00	−83.33	−33.33	−16.67	−20.00
Current Configuration						
	F_x	F_y	F_z	M_x	M_y	M_z
Excitation (Volts)	10	10	10	10	10	10
Gain	4000	4000	4000	2000	4000	4000
Zero Set Point (percent)	0.00	0.00	0.00	0.00	0.00	0.00
Analog Sensitivities (mV/lb) (Conditioned)	250.00	250.00	60.00	150.00	300.00	250.00

The start-up procedure used for testing is similar to the dynamic validation start-up procedure, but with two additional steps. The common steps included entering the setting for the load cell and performing a poke test. The settings for the load cell were very similar to the previous settings but M_x was larger to account for the moment on the body. The poke test ensured that the load cell was responding to loads and was oriented properly. Unlike the

dynamic validation, a hardware zero was not performed on the load cell. The first additional step was to power on the wave probes by applying +24V from the DC power supply. The second additional step was to power on and initialize the wavemaker using the provided control software.

Similar to the dynamic validation procedure, a custom data collection script, written in MATLAB, was used for real-time plotting and collecting the test data from the NI USB-6363 instrument. Each test run consisted of first starting the wavemaker to generate the desired wave environment. Then, after waiting for the initial waves to pass the cylindrical body, the data collection program was started. Data was collected for 60 seconds and during that time the collection program displayed a real-time plot of the collected channels. Before the first test run of the day, and periodically during testing, a zero file was collected for 60 seconds. Like for dynamic validation testing, this zero file allowed for the electrical offset of the load cell and the wave probes to be removed from the data

The test matrix for this thesis consisted of a number of test sequences. For each test sequence, the wave environment in the towing tank was generated by combining two constant amplitude and frequency regular waves to create an irregular seaway. The frequency of the first regular wave, denoted as wave 1, was held fixed for a given test sequence. During the test sequence, the frequency of the second wave, wave 2, was varied over the range of interest. Then, another test sequence was undertaken by changing the frequency of wave 1 to a new fixed value. In total, nine different test sequences were conducted corresponding to wave 1 frequencies that resulted in non-dimensional wavelengths, λ/L, of 1.00, 1.25, 1.50, 1.75, 2.00, 2.25, 2.50, 2.75, and 3.00. For this study, the test sequences were conducted in two different wave environments, a baseline wave environment and a large wave environment. The baseline wave environment consisted of wave 1 with a fixed amplitude of 0.5 inch and wave 2 with a fixed amplitude of 1.0 inches. The large wave environment was where wave 1 and wave 2 both had fixed amplitudes of 1.0 inches. Appendix D contains the experimental testing matrices which show the complete combination of wave frequencies tested.

The irregular seaway was created by providing both waves as the combined input signal to the wavemaker controller. The command signal of the wedge was given by Equation 4.1 where c_i is the desired wedge displacement, ω_i is the desired wedge frequency, t is time, and ϕ_i is the phase of the i^{th} wave component.

$$z_w(t) = \sum_{i=1}^{2} c_i \sin(\omega_i t) + \phi_i \tag{4.1}$$

All test runs within a given test sequence were conducted in random order. The test matrices also show the actual run numbers utilized for this study. The desired wave frequency and amplitude were entered in the wedge parameters file. After all the parameters were checked for accuracy, the wavemaker was started via its software to read the parameters file and then generate the desired waves.

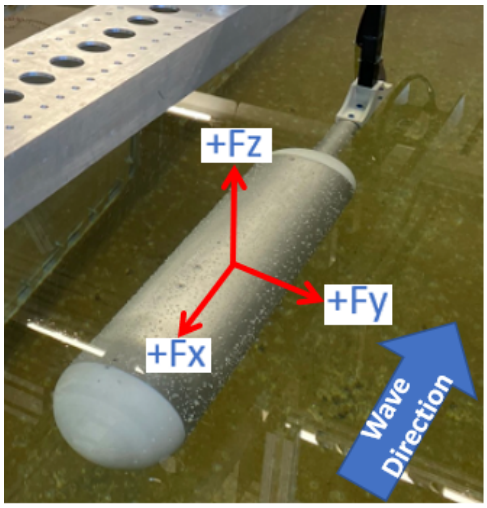

Figure 4.3. Coordinate system of the body and the wave traveling direction.

4.3 Source of Uncertainty

The selected diameter of the body used for testing was a compromise. If the body diameter was too small, the forces exerted on the body, especially the nonlinear ones, would be too small to measure accurately. On the other hand, if the body diameter was too large, the cross-sectional area of the body would cause blockage and wall effects in the tow tank. The body tested had a diameter of 6 inches and resulted in the tank width (W) to body diameter (D) ratio of 6. Klamo et al. [7] discussed their measurements of the wave-induced linear loads on fully submerged bodies with W/D ratios of 6 and 8. They measured the same loads on the bodies and concluded that blockage and the wall effects were negligible for the larger

diameter body. This thesis also compared the linear loads to the theoretical predictions for a fully submerged body in an unbounded fluid, and the results were consistent with the theory. This further proves that blockage and wall effects were negligible.

If the submerged body is too close to the free surface, then it will interact with the passing waves and cause them to break. This will result in different loads on the body. To ensure the body did not interact with the waves, the tests were performed at a depth of 1.5 diameters. Turner, Klamo, and Kwon [16] proved that interactions occurred when the body was at 1.0 diameters below the free surface. Furthermore, since the measured linear loads were consistent with Cummins' theoretical predictions, free surface effects were also negligible.

This study also involved intermediate water depth effects for the longest waves tested. A general ocean engineering rule of thumb is that the deep water wave assumption is valid if the water depth is at least half the passing wavelength or greater. If it is less than that, then the orbital motion of fluid particles, caused by a passing wave, interacts with the bottom. This interaction will disturb the classic deep-water assumptions. Although most wavelengths used in this study, considering the 38 inches of water depth, satisfied the deep water assumption, non-dimensionalized wavelengths (λ/L) greater than 2.50 did not. However, the rule of thumb is simply guidance that suggests where intermediate water effects begin to occur. The fact that our linear results agreed with Cummins' theoretical predictions suggests that intermediate water depth effects were also negligible.

Wave breaking for the shortest wavelengths tested was also a source of uncertainty for this study. According to linear wave theory, waves are unstable and must break when the wave steepness is larger than 1/7. This is under ideal conditions; in practice, waves can break with a steepness as low as 1/10. To avoid any wave breaking the steepest waves tested in this study were 1/11. During testing, the wave profiles were visually observed and no distinct wave breaking was seen.

The load cell measurement error was estimated from the dynamic validation results. The difference between the measured and applied forces was quantified and examined. According to the validation runs repeated for each weight, the load cell's measurement error was calculated at a mean of less than 8%. More discussion about the load cell's measurement accuracy can be found in Chapter 6.

A final source of uncertainty is with the repeatability of the generated waves. All the desired 1-inch amplitude waves generated had actual wave amplitudes between 0.8 and 1.1 inches. All the desired 0.5-inch amplitude waves had actual wave amplitudes between 0.6 and 0.4 inches. This study discusses wave generation repeatability in further detail with Figure 6.3 in Chapter 6.

CHAPTER 5:
Data Reduction

5.1 Data Cleaning

This study collected the analog output voltages from the load cell, and wave probes when used, and stored them in a single ".dat" file for each run. All output files were cleaned, using custom scripts to remove electrical offsets from the data. This cleaning process also applied the gain values to each channel to convert from measured voltages to physical units. Finally, the cleaning process also applied the load cell orientation matrix to align the local load cell coordinate system with the body's coordinate system, shown in Figure 4.3.

5.2 Dynamic Validation

Figure 5.1 shows an example of the data from a validation run. This investigation performed each run for approximately 90 seconds. The first 30 seconds of each run had the validation weight resting on the weight pan without any disturbance. This created a steady load for each run during this part of the test run. The weight was then removed after 30 seconds. The spring started oscillating following the removal of the weight which caused an oscillating load signal.

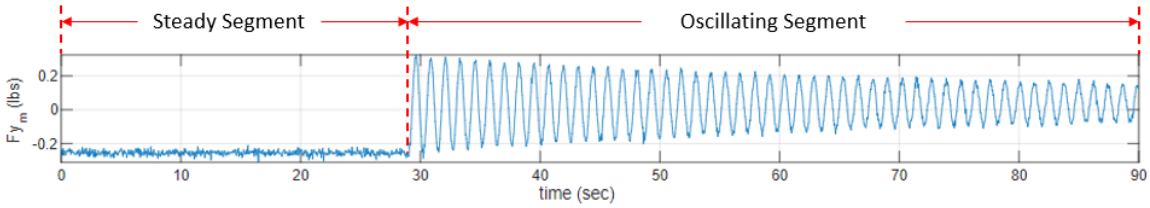

Figure 5.1. An example of load time history (weight=0.30 lbs, signal on F_y).

This study analyzed the steady load to determine the accuracy of the load cell when measuring a static load. Figure 5.2 shows an example of the steady segment from Figure 5.1 for the 0.30 lbs validation weight. The investigation used the steady segment and calculated

the mean value of that data set. The red line shows the calculated mean value, which is approximately 0.255 lbs. The validation process compared the calculated mean values to the validation weights to estimate the accuracy of the load cell when measuring static loads from 0.05 to 1.00 lbs.

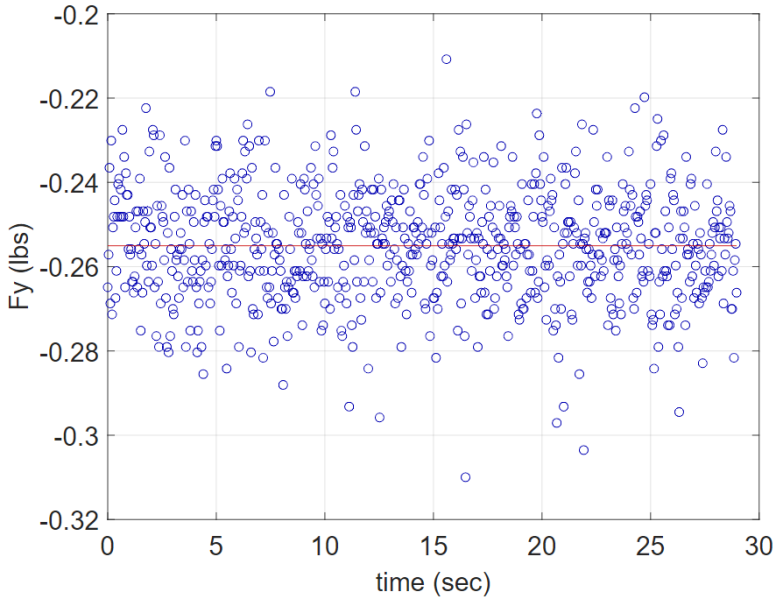

Figure 5.2. An example of static load fit data output (weight=0.30 lbs, signal on F_y).

The decaying sinusoidal signals collected during the oscillating segment of the time history were fit to

$$F_i = \alpha e^{(-\beta t)} \cos(\omega t + \phi) + \delta \tag{5.1}$$

in a least-squares sense, using a custom MATLAB script. The custom script performed multiple fittings with each curve fit using two cycles of data. Figure 5.3 shows an example of the resultant curve-fits to the dynamic load data for a validation weight of 0.15 lbs with the load on the F_y axis. Each of these two-cycle fits is color-coded for easy identification.

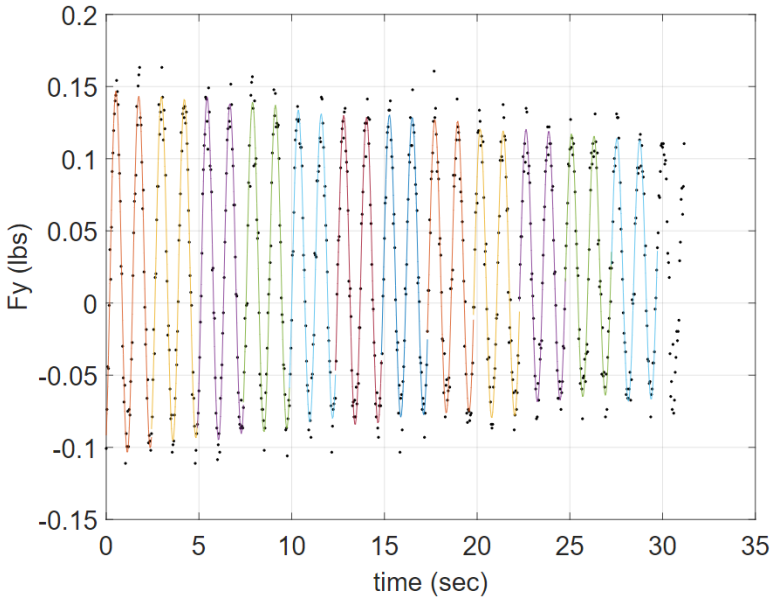

Figure 5.3. An example of dynamic load fit data output (weight=0.15 lbs, signal on F_y).

Solving Equation 5.1 for the coefficients α, β, ω, ϕ, and δ, in a least-squares sense, results in a nonlinear system of equations. This system requires that you iterate to determine the coefficient values. For the iterations to converge to the solution requires a suitable initial guess for each coefficient. The initial guess for α was the value of the first point in the oscillating data segment. The initial guess for β was estimated by looking at the decay of the second cycle compared to the first. The initial guess for ω was the Fourier transform frequency that contained the most energy. The initial guess for ϕ was π if the first point was negative and 0 if it was positive. Finally, the initial guess for δ was zero. Using these initial guesses, the custom-written script utilized an iterative approach to determine the coefficient values that best-fit Equation 5.1 to the collected decaying sine wave data. Once the curve-fitting process was complete, the parameter of interest was the α coefficient. This value represents the amplitude of the oscillating force signal. This value was then compared to the applied validation weight to determine the accuracy of the load cell when measuring a dynamic load. This accuracy was determined over the same load range as the static comparison, from 0.05 to 1.00 lbs.

5.3 Wave Amplitude and Wavelength

The wavenumber, k, for each of the two underlying wave components in the seaway was calculated using the finite depth, third-order dispersion relationship [7]

$$\omega_i^2 = g\, k_i\, \varphi_i \Big(1 + \frac{9 - 10\varphi_i^2 + 9\varphi_i^4}{8\varphi_i^4} (k_i\, a_{w_i})^2\Big), \tag{5.2}$$

where ω_i is the angular wave frequency, g is the gravitational constant, $\varphi_i = \tanh(k_i H)$, H is the water depth, and a_{w_i} is the wave amplitude. The subscript i refers to the fact that these parameters correspond to the i^{th} wave in the seaway. The wavenumber can be determined implicitly since the angular wave frequency is identical to the wedge oscillation frequency, which we know for each run. In Equation 5.2, $i = 1$ for the first wave and $i = 2$ for the second wave.

Because the custom MATLAB script had not evaluated the achieved wave height for the given test run at this stage in the data reduction process, the *desired* wave height was utilized in the computation. Since the waves were steep for certain conditions, and somewhat longer than twice the tank depth for others, the finite water depth, third-order dispersion relationship was utilized instead of the simplified linear deep-water dispersion equation. For high wave frequencies from 1.50 to 1.73 Hz, Klamo et al. [7] showed that the linear dispersion relationship predicts a shorter wavelength by 5%−7% than the finite depth, third-order relationship. Once the wave number, k, was estimated, the wavelength, λ, was calculated using

$$\lambda_i = \frac{2\pi}{k_i}, \tag{5.3}$$

where again $i = 1$ and $i = 2$ corresponds to the first and second wave, respectively.

This study measured the wave elevation in the towing tank during testing using four Senix probes denoted 1 – 4. Probe 4 was the most forward probe ahead of the body, and probe 1 was over the approximate mid point of the body. Figures 5.4 contains examples of wave elevation time histories from probe 4. Figure 5.4(a) shows a test run where the two wave frequencies, f_{w1}=1.017 Hz and f_{w2}=1.089 Hz, are very close to one another. It caused the wave amplitude pattern to resemble a classic beating pattern. Figure 5.4(b) shows a test run where the two waves frequencies, f_{w1}=1.017 Hz and f_{w2}=0.824 Hz are further apart from

each other. It caused the wave amplitude pattern to be a more irregular waveform.

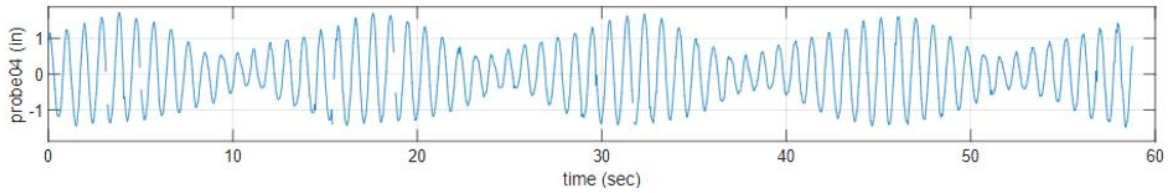

(a) f_{w_1} = 1.017 Hz and f_{w_2} = 1.089 Hz

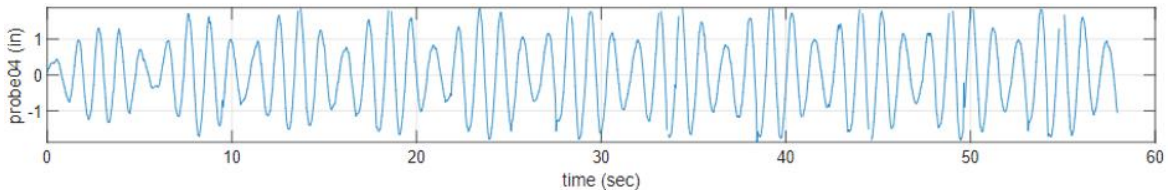

(b) f_{w_1} = 1.017 Hz and f_{w_2} = 0.824 Hz

Figure 5.4. Examples of wave time histories for probe 4.

The wave elevation time histories from probes 1 – 4 where each fit, in a least-squares sense, to the function [5]

$$\eta(x,t) = \sum_{i=1}^{2}(A_{1,i}\cos(k_i x_i - \omega_i t) + B_{1,i}\sin(k_i x_i - \omega_i t)) + C \tag{5.4}$$

where cosine and sine components of the linear amplitude are represented by the coefficients $A_{1,i}$ and $B_{1,i}$, respectively. These coefficients were combined to create a single wave amplitude ($a_{w,i}$) and phase angle ($\varphi_{w,i}$). The data set's mean is represented by C. The location of the probes, relative to the body origin, given by x_i, was measured before testing and its use in Equation 5.4 keeps the phase angle fixed across each wave probe. As discussed in Chapter 2, probe 1 was over the cylindrical body, and probes 2 – 4 were located ahead of the body.

For every wave component i, once the wavenumber, k_i, and wave amplitude, a_{w_i} was known, the wave height, h_i, was determined by computing the third-order Stokes wave height approximation [7]

$$h_i = 2a_{w_i}(1 + \frac{3}{8}(k_i\, a_{w_i})^2)\ . \tag{5.5}$$

Klamo et al. [15] found that this relationship accurately approximates the elevation time history of these steep waves in the tow tank. Because several of the shorter wavelengths examined were fairly steep, this approximation was utilized instead of merely doubling the wave amplitude. Twice the wave amplitude under predicts the wave height by around 3% at the higher test frequencies, between 1.50 and 1.73 Hz.

5.4 Wave-Induced Loads

For each test sequence, the wave 1 frequency (f_{w_1}) was held fixed and the wave 2 frequency f_{w_2} was varied for each test run. By keeping the f_{w_1} fixed and changing f_{w_2}, various irregular seaways were created, and the resultant wave-induced loads on the body were measured. Figure 5.5 shows examples of load time histories from one of the test sequences with a fixed wave 1 nondimensional wavelength, λ/L, of 2.0. Figure 5.5(a) shows the measured heave force when the two wave frequencies, f_{w_1}=1.017 Hz and f_{w_2}=0.931 Hz, are very close to each other. Figure 5.5(b) shows the measured heave force when there is a larger difference between the two wave frequencies, f_{w_1}=1.017 Hz and f_{w_2}=1.573 Hz.

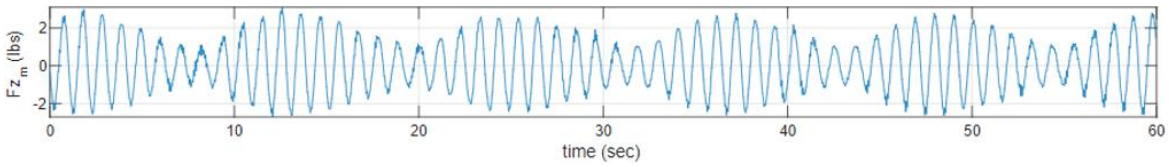

(a) f_{w_1} = 1.017 Hz and f_{w_2} = 0.931 Hz

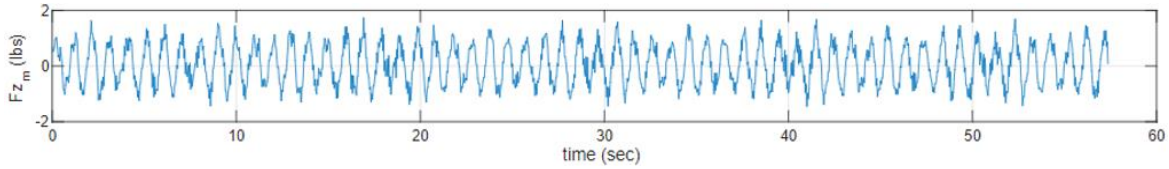

(b) f_{w_1} = 1.017 Hz and f_{w_2} = 1.573 Hz

Figure 5.5. Examples of load cell time histories for F_z.

The surge, heave, and pitch moment time history data were fitted in a least-squares sense to [5]

$$\begin{aligned} f(t) = &\sum_{i=1}^{2}(A_{1,i}\cos(-\omega_i t) + B_{1,i}\sin(-\omega_i t)) \\ &+ \sum_{i=1}^{2}(A_{2,i}\cos(-2\omega_i t) + B_{2,i}\sin(-2\omega_i t)) \\ &+ A_+\cos(-|\omega_1+\omega_2|t) + B_+\sin(-|\omega_1+\omega_2|t) \\ &+ A_-\cos(-|\omega_1-\omega_2|t) + B_-\sin(-|\omega_1-\omega_2|t) + C\ . \end{aligned} \tag{5.6}$$

The least-squares solution to solve the nine unknown coefficients, $A_{1,i}$, $B_{1,i}$, $A_{2,i}$, $B_{2,i}$, A_+, B_+, A_-, B_-, and C in Equation 5.6 is a linear system of equations. These coefficients can be explicitly written out and solved for in matrix form.

Each wave component creates an oscillating linear force that is captured by the $A_{1,i}$ and $B_{1,i}$ coefficients in Equation 5.6. These linear loads occur at the wave encounter frequency with the body. This implies that, while these loads are bigger than the nonlinear loads, they occur over a considerably shorter time scale. This time scale is generally too short for large underwater vehicles to respond to; thus, smaller underwater vehicles are more concerned with these linear loads.

Nonlinear loads arise due to waves interactions, even when a wave interacts with itself. This wave self-interaction produces the nonlinear loads that occur at twice the wave encounter frequency and the cosine and sine components of these loads are captured by the $A_{2,i}$ and $B_{2,i}$ coefficients, respectively. The wave interactions that occur between two different waves creates nonlinear loads at the frequency sum and difference of the interacting waves. The cosine and sine portions of these nonlinear loads are captured by the A_+ and B_+ coefficients for the frequency sum and the A_- and B_- coefficients for the frequency difference. Finally, the C coefficients captures both the remaining electrical offset in the load cell as well as the nonlinear mean loads of waves interacting with themselves at the frequency difference (0 Hz).

For this thesis, we are interested in the frequency difference nonlinear loads. These are important for large underwater vehicles since they occur over a very large time scale and

can affect the vehicle's stability and controllability.

The amplitude and phase for any of the linear or nonlinear loads can be calculated by converting the cosine and sine component coefficients into the equivalent amplitude and phase using Equations 5.7 and 5.8, respectively.

$$a_{*,i} = \sqrt{(A_{*,i})^2 + (B_{*,i})^2} \tag{5.7}$$

$$\phi = \tan^{-1}\left(\frac{B_{*,i}}{A_{*,i}}\right) \tag{5.8}$$

where $*$ represents either 1, 2, +, or − from Equation 5.6.

The study non-dimensionalized the linear forces using

$$C_{F,\text{linear}} = \frac{a_F}{\rho g A_o h} \tag{5.9}$$

where a_F is any linear surge or heave force amplitude given by Equation 5.7, ρ is the fluid density, g is the acceleration due to gravity, A_o is the cross-sectional area of the body, and h is the wave height. The moments were non-dimensionalized by

$$C_{M,\text{linear}} = \frac{a_M}{\rho g A_o h L} \tag{5.10}$$

where a_M is any linear pitch moment amplitude and L is the length of the body. The nondimensionalization of our linear force and moment amplitudes is consistent to that used by Cummins [4].

The nonlinear forces and moment amplitudes were non-dimensionalized using

$$C_{F,\text{nonlinear}} = \frac{a_F}{\rho g D h_1 h_2} \tag{5.11}$$

and

$$C_{M,\text{nonlinear}} = \frac{a_M}{\rho g D h_1 h_2 L}, \tag{5.12}$$

where a_F and a_M is any nonlinear surge or heave force amplitude or pitching moment amplitude given by Equation 5.7 and h_1 and h_2 are the wave heights of the two underlying wave components. Also, the nonlinear nondimensional terms use the diameter of the cylindrical body, D, instead of the cross-sectional area, A_o.

THIS PAGE INTENTIONALLY LEFT BLANK

CHAPTER 6:
Findings and Analysis

6.1 Dynamic Validation Results

This section discusses the results of the load cell accuracy study. A dynamic validation test matrix depicted in Table C.1 in Appendix C was developed to perform the validation process using eight different weights, tested 5 times each, in random order. While this study was more specifically interested in dynamic load validation, it also investigated static load validation results to make a comparison to the dynamic measurement accuracy. This investigation conducted the validation on both channels, F_x and F_y, but in this section, only the results for the F_y channel are discussed. The static and dynamic results for the F_x channel can be found in Appendix E.

Figure 6.1 shows the static validation results for the F_y channel. Figure 6.1a has a reference line with a slope of one. If the measured load exactly matched the applied load, the data would lie precisely on the line. However, this investigation found that the load cell, like any other sensor, has some measurement error. These errors are the vertical distances from the data points to the reference line. Figure 6.1b shows the difference between the measured load and the applied load. This difference is shown on the y-axis as a function of the applied load on the x-axis. For instance, five random validation runs for 1.00 lbs have a mean of approximately 0.07 lbs (7%) measurement error for this study, which was the largest error. Smaller applied loads had less error.

The error appears biased to always under measure the actual value of the force. One possible explanation for this is that the electrical offsets determined from the zero file collection was slightly too large compared to the offset of the load cell during testing.

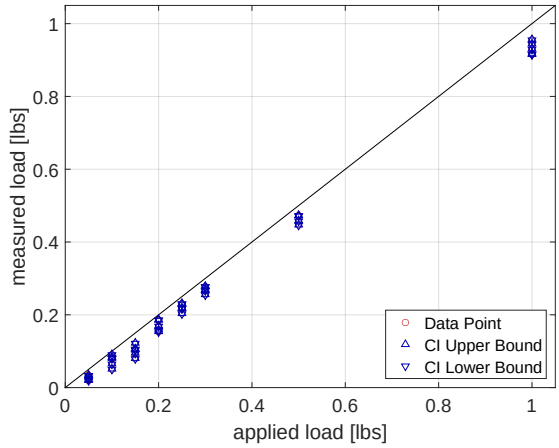

(a) static load results

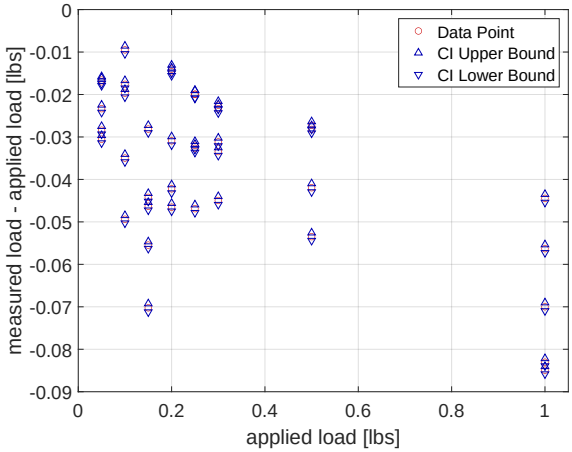

(b) static load difference results

Figure 6.1. Experimental validation static results of the load cell for F_y channel.

Since the linear and nonlinear wave-induced loads are dynamic oscillating loads, the focus of this validation study was on quantifying the load cell accuracy when measuring dynamic loads. Figure 6.2 depicts the dynamic experimental validation results for the F_y channel. Comparing results in Figure 6.2a to the static results, we can see that the data points are closer to the reference line. In Figure 6.2b, the differences between the measured and applied loads, for applied loads less than 0.5 lbs, are now between 0.02 lbs and -0.04 lbs which is a smaller error than was observed for the static loads. One possible reason for the better

accuracy is that the analysis of the oscillating load signal does not depend on the measured electrical offset, nor is the analysis affected by slight changes in the electrical offset value during testing. Overall, the dynamic validation investigation concluded that the load cell was sensitive enough to measure periodic oscillating forces as small as 0.05 lbs.

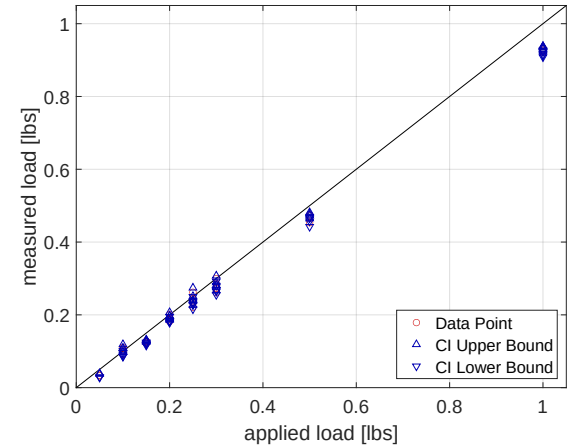

(a) dynamic load results

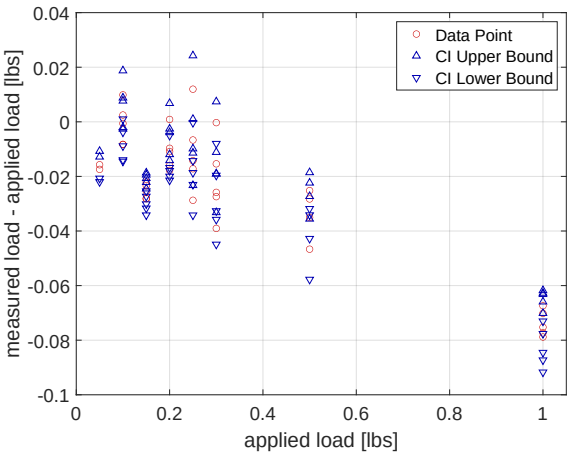

(b) dynamic load difference results

Figure 6.2. Experimental validation dynamic results of the load cell for F_y channel.

6.2 Generated Wave Environments

This investigation explored irregular seaways with two different wave heights. The first wave environment consisted of a 0.5-inch amplitude regular wave and a 1.0-inch amplitude regular wave. The second seaway consisted of two 1.0-inch amplitude regular waves. Figure 6.3 shows the wave amplitude of both underlying regular waves versus experimental test run numbers. The first wave is captured by the blue data and the second wave is denoted by the red data. Runs 1000 to 1265 show the 0.5 and 1.0-inch wave amplitude environments, while runs greater than 1265 show the results when both waves had an amplitude of 1.0 inch. As discussed in chapter 4, the majority of the actual wave amplitudes for all the intended 1-inch amplitude waves were between 0.8 and 1.1 inches. The majority of the actual wave amplitudes for all the required 0.5-inch waves were between 0.6 and 0.4 inches.

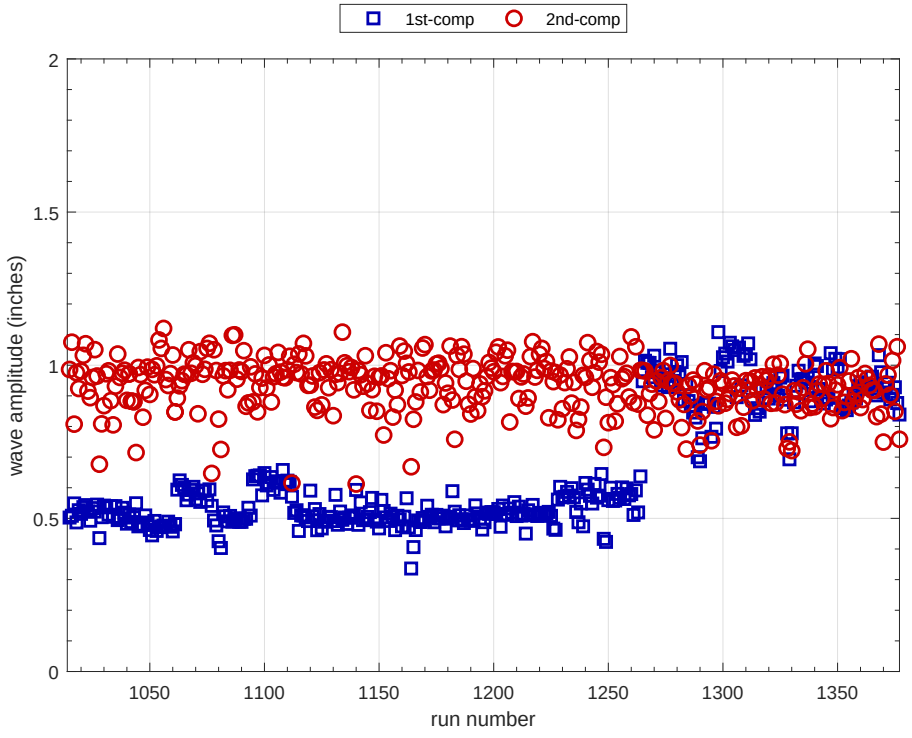

Figure 6.3. Wave amplitudes vs. experimental test run numbers.

6.3 F_z, F_x, and M_y Linear Load Results

Although our focus was on the nonlinear frequency difference loads, the linear loads are part of the collected load signal, so we compared them to theoretical predictions as a data quality check. When testing in a two-component seaway, there are two linear loads present, one from each of the regular waves. In this section, we examine F_z, F_x, and M_y for three different λ_1/L values. Only the results from three representative wave environments are shown in this chapter, while all the linear load results can be found in the Appendix F.

Figure 6.4 shows a comparison of current and previous experimental measurements along with the theoretical predicted non-dimensional linear force in F_z at various wavelengths. The new measurements, collected during this investigation, are shown as the blue-colored data markers. Previously collected data [6] are denoted as the red data points. The theoretical prediction using Cummins theory is shown as the dashed black line. Figure 6.4(a) contains non-dimensionalized linear F_z force results for a fixed wave 1 wavelength of $\lambda_1/L = 1.50$ and a wave 2 wavelength that was varied between $\lambda_2/L = 0.75$ and 3.00. Since the wavelength of wave 1 was held fixed during a test sequence, all the linear F_z forces due to wave 1 are clustered at that nondimensional wavelength, while the linear F_z forces due to wave 2 span the x-axis since the wavelength of wave 2 was varied.

Figure 6.4(b) shows the two linear F_z force results but now for a fixed wave 1 wavelength of $\lambda_1/L = 1.75$ and the same range of wavelengths for wave 2. The wave 1 force results now cluster around $\lambda_1/L = 1.75$. Figure 6.4(c) depicts the two linear nondimensional F_z results for $\lambda_1/L = 2.00$ and the same range of wavelengths for wave 2. Wave 1 force results are now clustered around $\lambda_1/L = 2.00$.

The linear F_z force results for all the wave environments that this investigation duplicated, and thus could compare, were consistent with Hermsen's [6] results, to the level of agreement shown in Figures 6.4(a) – 6.4(c). In this study, we examined 9 different wave 1 wavelengths whereas the previous Hermsen study [6] only looked at $\lambda_1/L = 1.0, 1.5, 2.0, 2.5$, and 3.0. Furthermore, the results are consistent with the theoretically predicted linear F_z force for every wave environment this study tested.

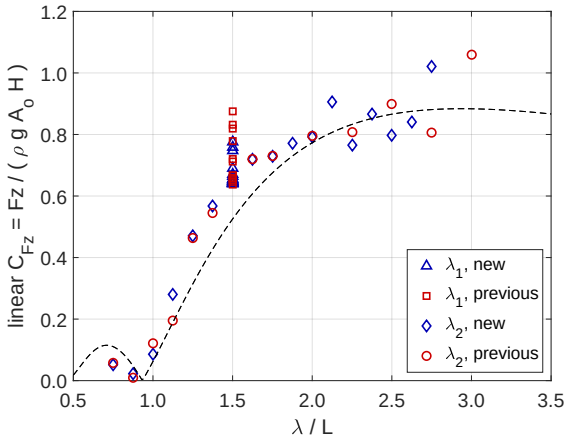

(a) $\lambda_1/L = 1.50; \lambda_2/L$ = various

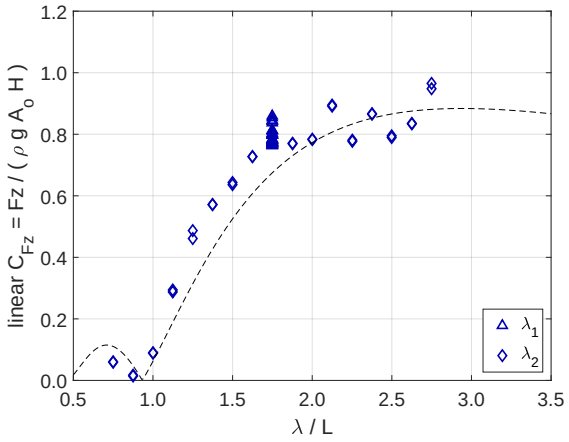

(b) $\lambda_1/L = 1.75; \lambda_2/L$ = various

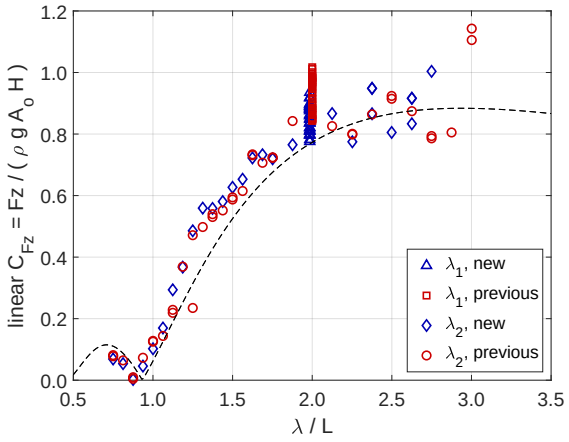

(c) $\lambda_1/L = 2.00; \lambda_2/L$ = various

Figure 6.4. Comparison of measured and predicted non-dimensional linear force on F_z at various wavelengths.

Figure 6.5 compares current and prior experimental measurements with the theoretically expected non-dimensional linear force in F_x at different wavelengths. The formatting of Figure 6.5 is the same as that used for Figure 6.4. Figure 6.5(a) contains non-dimensionalized linear F_x force results for a fixed wave 1 wavelength of $\lambda_1/L = 1.50$ and a wave 2 wavelength that was varied between $\lambda_2/L = 0.75$ and 3.00. Identical to Figure 6.4, since the wavelength of wave 1 was held fixed during the test sequence, all the linear F_x forces due to wave 1 are clustered at that nondimensional wavelength, while the linear F_x forces due to wave 2 span the x-axis since the wavelength of wave 2 was varied. Figure 6.5(b) shows the two linear F_x force results but now for a fixed wave 1 wavelength of $\lambda_1/L = 1.75$ while Figure 6.5(c) shows the results for $\lambda_1/L = 2.00$. The range of wave 2 wavelengths is the same as Figure 6.5(a).

For all the wave environments that this investigation duplicated to the previous study of Hermsen's [6], the linear F_x force results were consistent with those results, to the level of agreement indicated in Figure 6.5(a) – 6.5(c). Moreover, the results are in conformity with the theoretically predicted linear F_x force from Cummins' theory for each of the wave environments examined in this work.

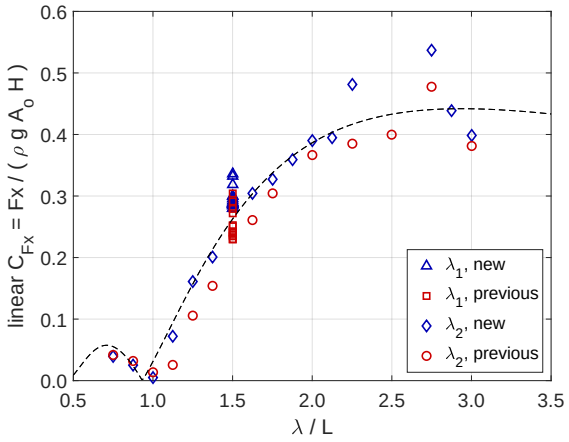

(a) $\lambda_1/L = 1.50; \lambda_2/L =$ various

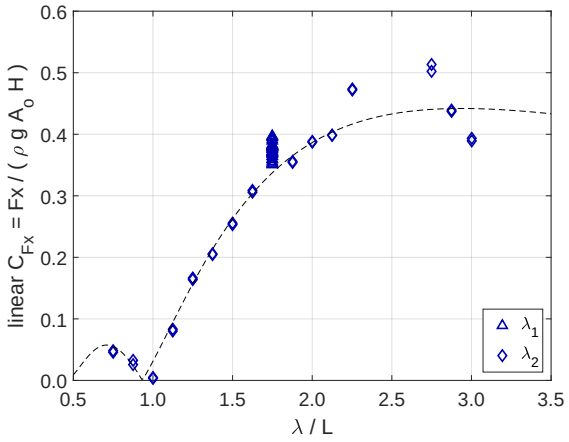

(b) $\lambda_1/L = 1.75; \lambda_2/L =$ various

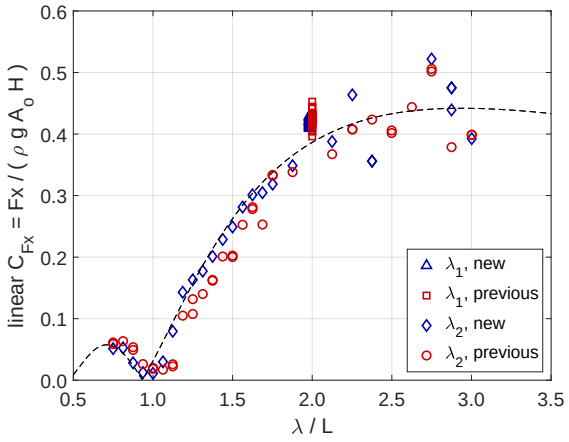

(c) $\lambda_1/L = 2.00; \lambda_2/L =$ various

Figure 6.5. Comparison of measured and predicted non-dimensional linear force on F_x at various wavelengths.

The current and previous experimental measurements along with the theoretical predicted nondimensional linear moment in M_y at various wavelengths are shown in Figure 6.6. The figure formatting is the same as that used in Figures 6.4 and 6.5. Figure 6.6(a) covers nondimensionalized linear M_y moment results for a fixed wave 1 wavelength of $\lambda_1/L = 1.50$, Figure 6.6(b) shows the two linear M_y moment results for a fixed wave 1 wavelength of $\lambda_1/L = 1.75$, and Figure 6.6(c) depicts the two linear M_y moments for $\lambda_1/L = 2.00$.

The linear M_y moment results were consistent with Hermsen's [6] results for wave environments where the previous results existed. The results are also consistent with the theoretically predicted linear M_y moment for every wave environment this study tested. The level of agreement shown in Figures 6.6(a) – 6.6(c) is representative of the level of agreement for all the wave environments that this research explored.

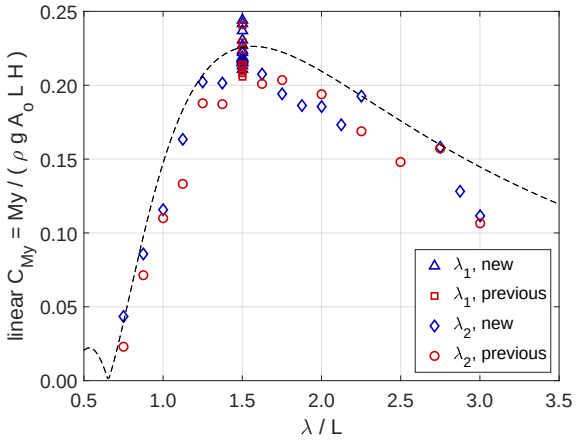

(a) $\lambda_1/L = 1.50; \lambda_2/L =$ various

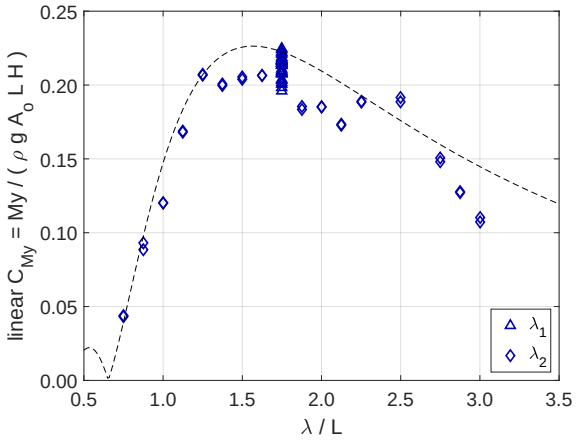

(b) $\lambda_1/L = 1.75; \lambda_2/L =$ various

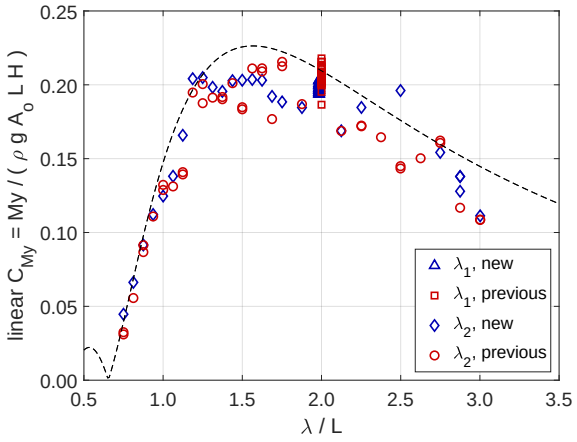

(c) $\lambda_1/L = 2.00; \lambda_2/L =$ various

Figure 6.6. Comparison of measured and predicted non-dimensional linear force on M_y at various wavelengths.

6.4 F_z, F_x, and M_y Nonlinear Load Results

The main focus of this study was on the experimental measurement of the nonlinear loads. In this section, we present the results for the baseline wave environment where wave 1 had an amplitude of 0.5 inch, and wave 2 had an amplitude of 1.0 inch. The same three test conditions that were shown in the linear load results section are shown here. All of the nonlinear force results, however, can be found in Appendix F.

Figure 6.7 shows a comparisons between the previous and current measured non-dimensional nonlinear force F_z at various wave 2 wavelengths. The blue-colored data markers represent the new measurements gathered during this study. The red data points represent previously gathered data [6]. Non-dimensionalized nonlinear F_z force values for a fixed wave 1 wavelength of $\lambda_1/L = 1.50$ and a wave 2 wavelength changing from $\lambda_2/L = 0.75$ to 3.00 are shown in Figure 6.7(a). Unlike the linear results where each wave produced a force, there is only one nonlinear force, and it occurs at the frequency difference between the two waves. However, the nonlinear force value is shown in Figure 6.7(a) against the wave 2 wavelength.

Figure 6.7(b) shows the non-dimensionalized nonlinear F_z force results but now for a fixed wave 1 wavelength of $\lambda_1/L = 1.75$ and the same range of wave 2 wavelengths. Figure 6.7(c) depicts the same results but for $\lambda_1/L = 2.00$. For all the wave environments that this research replicated, and therefore could compare, the nonlinear F_z force results were consistent with Hermsen's [6] results to the degree indicated in Figures 6.7(a) – 6.7(c).

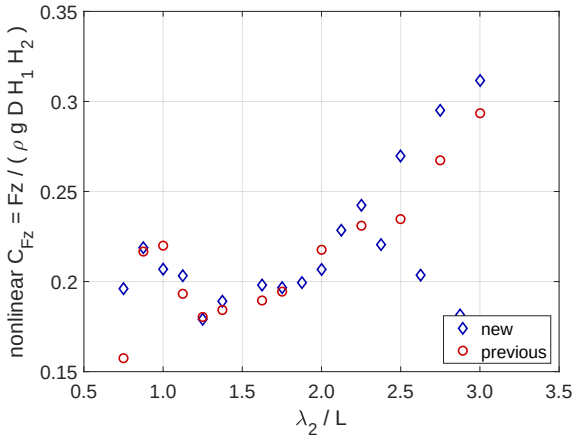

(a) $\lambda_1/L = 1.50; \lambda_2/L =$ various

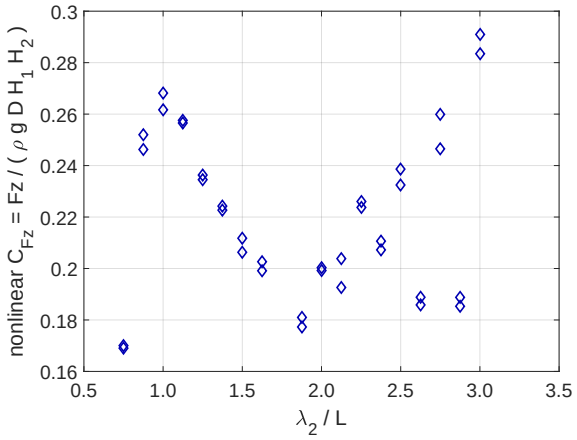

(b) $\lambda_1/L = 1.75; \lambda_2/L =$ various

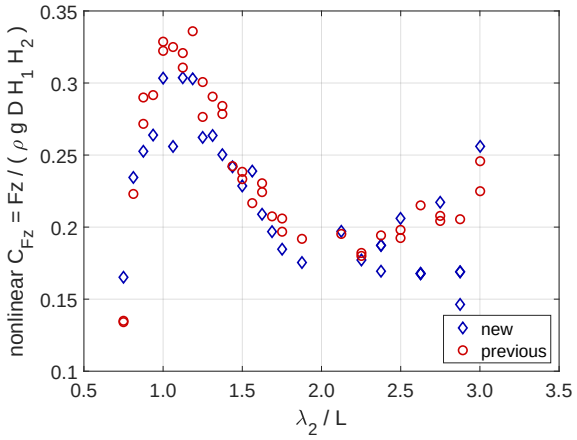

(c) $\lambda_1/L = 2.00; \lambda_2/L =$ various

Figure 6.7. Comparison of measured and predicted non-dimensional nonlinear forces on F_z at various wavelengths.

The comparisons of the measured non-dimensional nonlinear F_x forces at various wave 2 wavelengths are shown in Figure 6.8. The formatting of the figures is that same as Figure 6.7. Figure 6.8(a) depicts non-dimensionalized nonlinear F_x force values for a fixed wave 1 wavelength of $\lambda_1/L = 1.50$ and a wave 2 wavelength varying from $\lambda_2/L = 0.75$ to 3.00. Even though the one nonlinear force occurs at the frequency difference between the two waves the force value is shown in the figure against the wave 2 wavelength. In a similar fashion, Figure 6.8(b) contains the non-dimensionalized nonlinear F_x force results but now for a fixed wave 1 wavelength of $\lambda_1/L = 1.75$ while Figure 6.8(c) depicts the nonlinear force values for $\lambda_1/L = 2.00$.

The experimental measurements show that the nonlinear F_x loads are approximately half the magnitude of the F_z nonlinear loads. Also, all the nonlinear F_x force results that were measured in wave environments that Hermsen's [6] also tested in, were consistent to her results to the level shown in Figures 6.8(a) – 6.8(c).

Figure 6.9 depicts the comparisons of measured non-dimensional nonlinear M_y moments at various wavelengths. Figure 6.9(a) shows the non-dimensionalized nonlinear M_y moment results for a fixed wave 1 wavelength of $\lambda_1/L = 1.50$ and the same range of wave 2 wavelengths used for Figures 6.7 and 6.8. Figure 6.9(b) shows the non-dimensionalized nonlinear M_y moment results for a fixed wave 1 wavelength of $\lambda_1/L = 1.75$ and the same range of wave 2 wavelengths. Finally, Figure 6.9(c) depicts the non-dimensional nonlinear M_y moment results for $\lambda_1/L = 2.00$. As was the case with the previously discussed linear and nonlinear results, all the measured nonlinear M_y moment results were consistent with Hermsen's [6] results to the level shown in Figures 6.9(a) – 6.9(c).

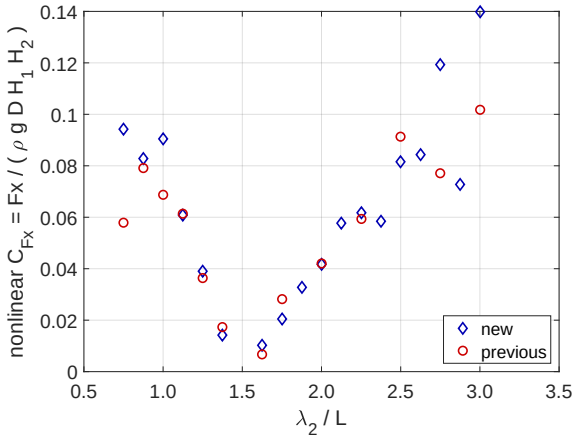

(a) $\lambda_1/L = 1.50; \lambda_2/L =$ various

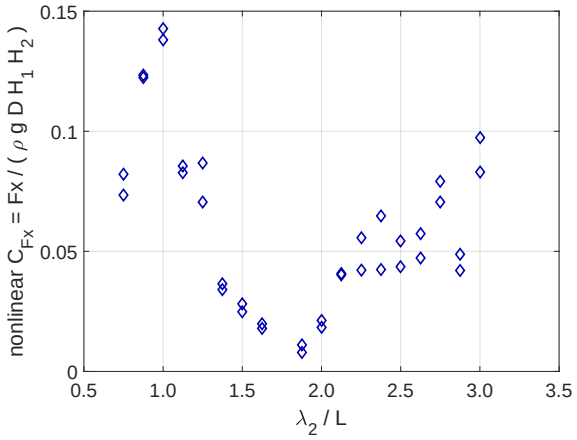

(b) $\lambda_1/L = 1.75; \lambda_2/L =$ various

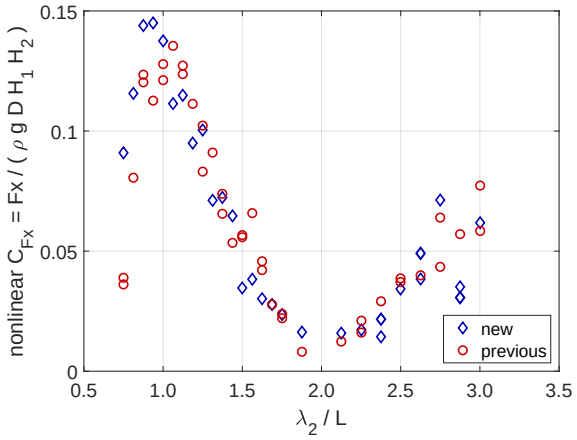

(c) $\lambda_1/L = 2.00; \lambda_2/L =$ various

Figure 6.8. Comparison of measured and predicted non-dimensional nonlinear forces on F_x at various wavelengths.

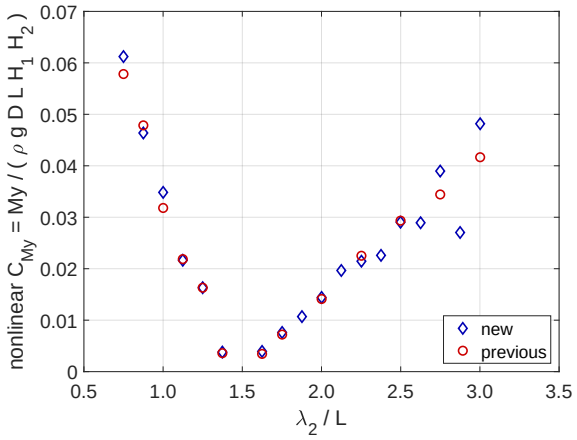

(a) $\lambda_1/L = 1.50; \lambda_2/L =$ various

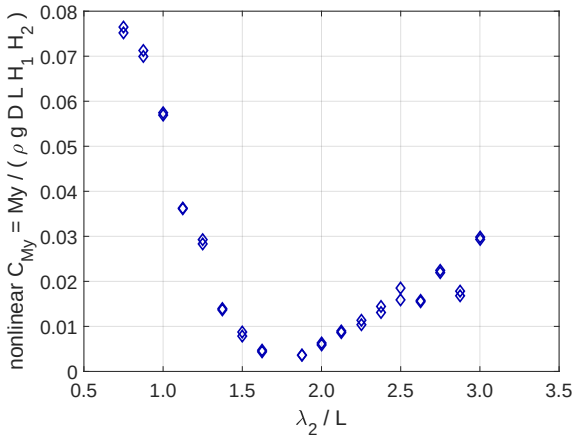

(b) $\lambda_1/L = 1.75; \lambda_2/L =$ various

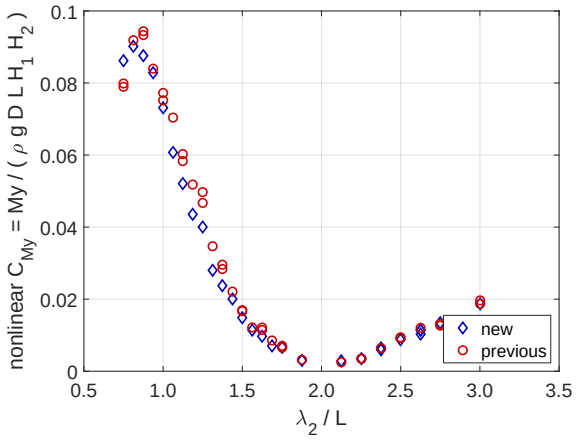

(c) $\lambda_1/L = 2.00; \lambda_2/L =$ various

Figure 6.9. Comparison of measured and predicted non-dimensional nonlinear forces on M_y at various wavelengths.

6.5 Larger Wave Height Results

This study also tested the same wavelengths a second time, but the amplitude of wave 1 was now 1.0 inches instead of 0.5 inches. The amplitude of wave 2 was still 1.0 inches. The smaller baseline wave height wave results can be compared to these larger wave height wave results to see if our nondimensionalization collapses the data and produces coefficient values that can be used to predict the loads on a body due to any size wave height.

Figure 6.10 shows a comparison between both the linear and nonlinear loads that this investigation measured in the smaller baseline wave environment and the larger wave height environment. The subfigures on the left side show the measured linear loads F_z, F_x, and M_y going from top to bottom. The right side subfigures show the corresponding frequency difference nonlinear loads in the same two wave environments, again F_z, F_x, and M_y going top to bottom. The baseline wave environment results are shown as the blue colored data points while the large wave height environment data is denoted with the green colored data points. As it was previously discussed, there are two linear force results shown in each figure, one corresponding to each of the two waves. These figures all show a wave environment where wave 1 had a fixed wavelength of $\lambda_1/L = 2.50$ and hence there is a cluster of wave 1 results at that wavelength.

From the theoretical solution for the linear loads, we know that our nondimensionalization should collapse the linear data results. The subfigures on the left show that the linear loads data collapses to a single result curve when non-dimensionalized using the wave height of the particular wave associated with the linear load. For the nonlinear loads, the subfigures on the right appear to show that the results collapse as well onto a single result curve when the product of wave 1 height and wave 2 height is used to non-dimensionalize the results. When the wave height varies, these nonlinear loads will vary as well. However, even though the physical loads change, when we appropriately non-dimensionalize these nonlinear loads, the non-dimensionalized nonlinear loads do not change.

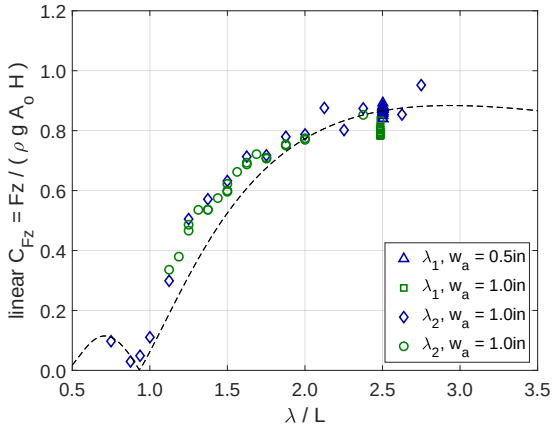

(a) F_z, $\lambda_1/L = 2.50; \lambda_2/L$ = various

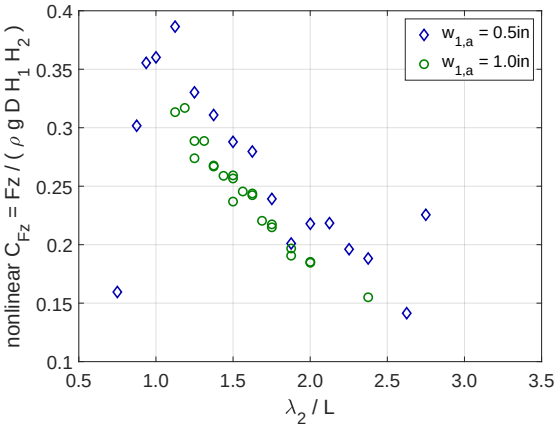

(b) F_z, $\lambda_1/L = 2.50; \lambda_2/L$ = various

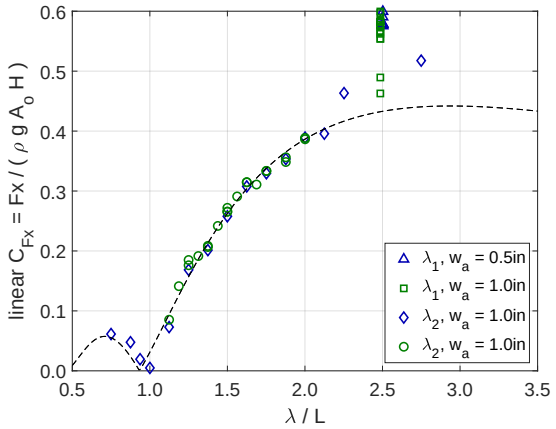

(c) F_x, $\lambda_1/L = 2.50; \lambda_2/L$ = various

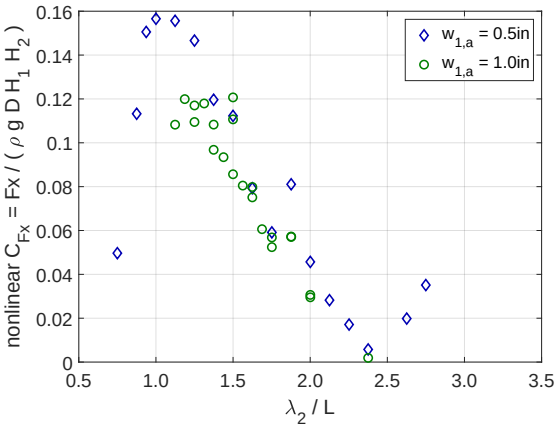

(d) F_x, $\lambda_1/L = 2.50; \lambda_2/L$ = various

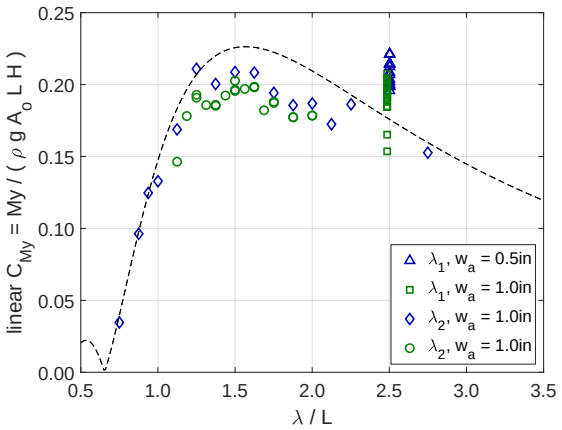

(e) M_y, $\lambda_1/L = 2.50; \lambda_2/L$ = various

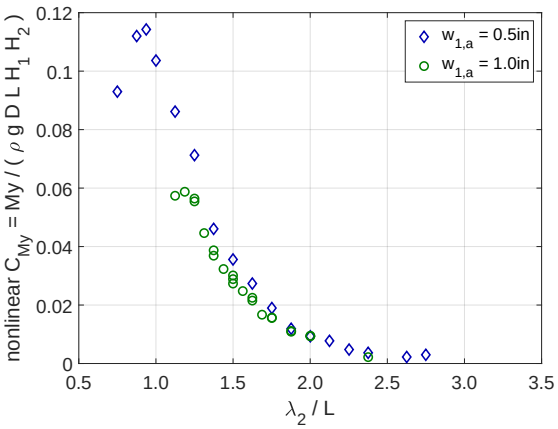

(f) M_y, $\lambda_1/L = 2.50; \lambda_2/L$ = various

Figure 6.10. Comparison of measured non-dimensional linear and nonlinear forces at 0.5 inch and 1.00 inch wave amplitudes.

6.6 Nonlinear Load Maps

This investigation conducted 9 different testing sequences where each sequence used a fixed frequency for wave 1 and varied the frequency of wave 2. By combining all of these test sequences together, we essentially spanned the entire frequency spaces of wave 1 and wave 2. These loads can be shown in this two-dimensional parameter space as a contour map where the contour value represents the local value of the nonlinear load at that particular combination of wave 1 and wave 2 wavelengths. Contour maps are developed for the baseline wave environment. Figures 6.11, 6.12, and 6.13 contain contour mappings of the measured non-dimensional nonlinear loads for F_z, F_x, and M_y, respectively.

The contour maps display a number of interesting findings. First, the order of wave 1 and wave 2 should not matter and therefore the contour map should be symmetric about a line with a slope of 1. This line is shown as the black dashed line in all three contour maps. All three nonlinear load results appear to show this symmetry. Second, along this symmetry line, F_x and M_y are zero valued while F_z appears to be roughly 0.2. Third, the results for all three nonlinear loads appear to have lines of constant value. This is most easily seen with the pitching moment results. The constant valued load lines suggest that possibly the data could be collapsed by using only the value of the frequency difference between the two waves and not the actual individual frequency, or wavelength, of each wave itself. And finally, these maps represent an empirically derived mathematical model that can be used to predict the nonlinear loads on an underwater vehicle as a function of the two underlying wavelengths and wave heights. These predicted loads could be utilized in a maneuvering or stability model as part of a model-based systems engineering approach when designing an underwater vehicle.

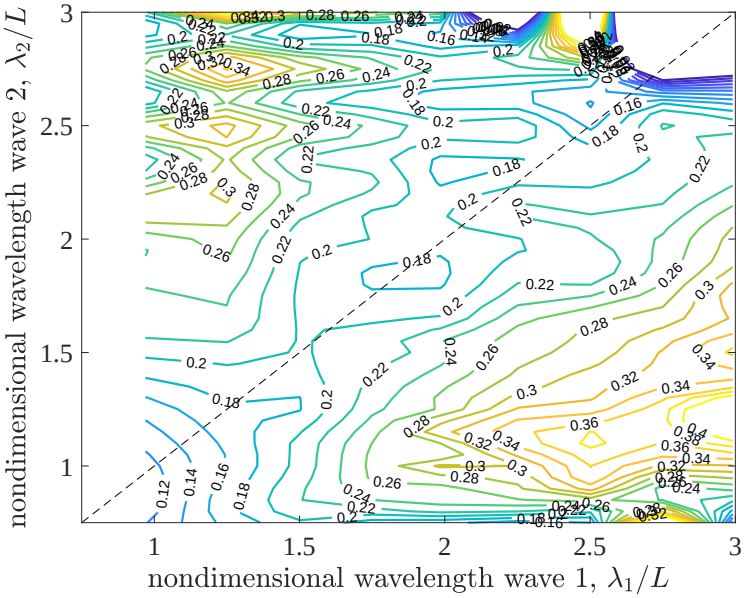

Figure 6.11. Contour mapping showing the measured frequency difference nonlinear forces F_z after being non-dimensionalized in the baseline wave environment.

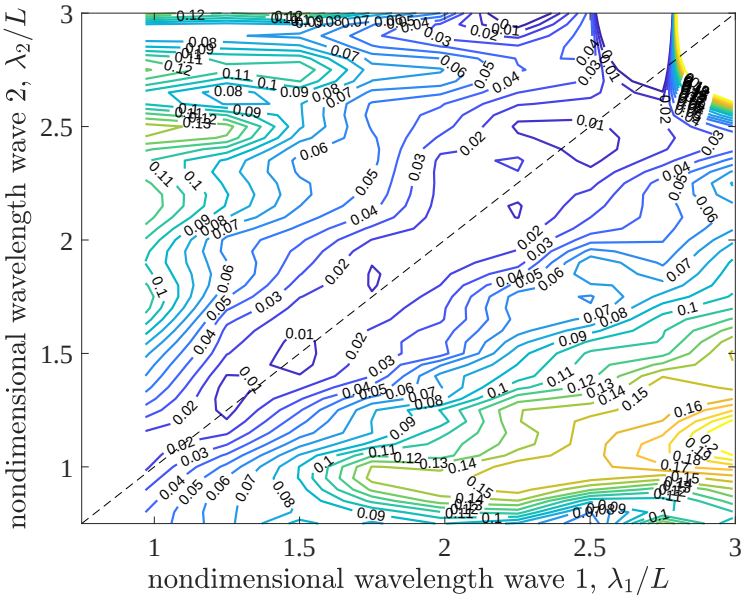

Figure 6.12. Contour mapping showing the measured frequency difference nonlinear forces F_x after being non-dimensionalized in the baseline wave environment.

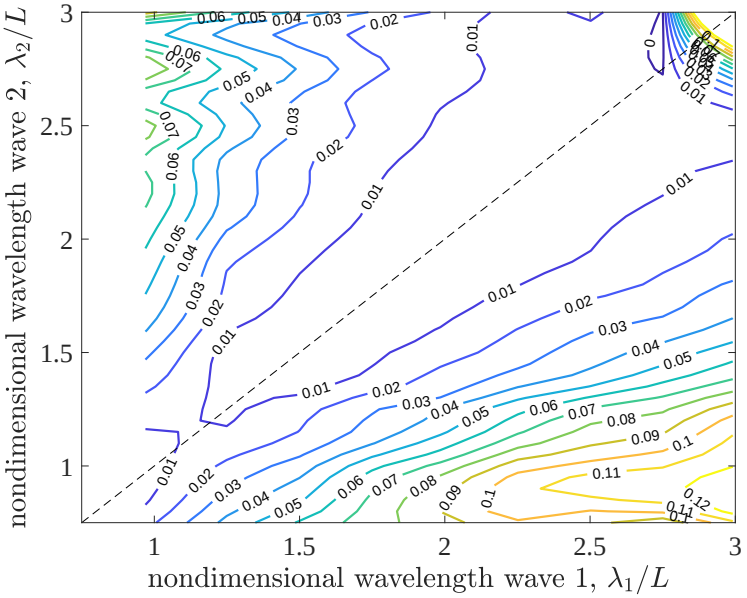

Figure 6.13. Contour mapping showing the measured frequency difference nonlinear forces M_y after being non-dimensionalized in the baseline wave environment.

This analysis also looked at the possibility of collapsing the nonlinear load data using a single parameter instead of wave 1 and wave 2 wavelengths. That parameter is the frequency difference value between the two underlying waves. Figure 6.14 shows results of non-dimensional nonlinear loads versus the frequency difference of the two underlying waves in the baseline wave environments we tested. Although the F_z results contain a little more scatter, the F_x and M_y results seem to suggest that the nonlinear loads collapse onto a single results curve that is a function of only the frequency difference between the waves. In Figures 6.14(a) and 6.14(b), the non-dimensionalized loads on F_z and F_x have the same tendency of having a maximum value around 0.5 Hz. For M_y in Figure 6.14(c), the non-dimensionalized force has a maximum value around 0.75 Hz.

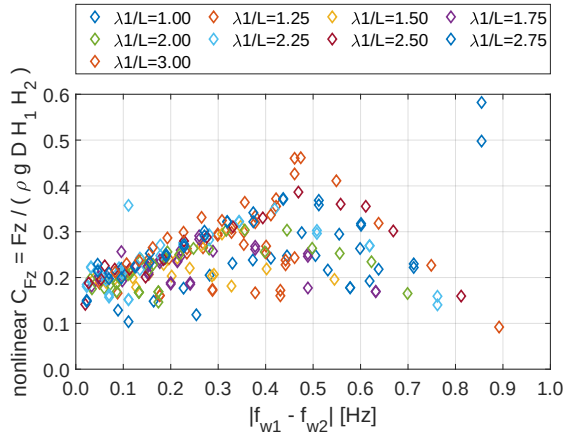

(a) F_z

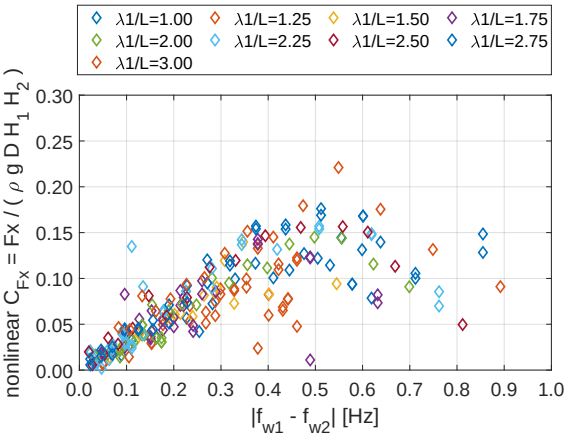

(b) F_x

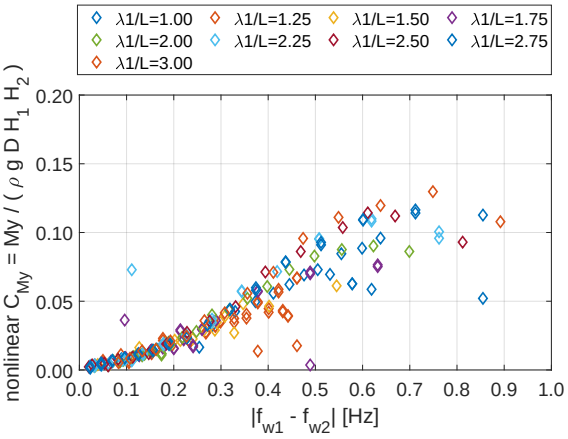

(c) M_y

Figure 6.14. Results of the non-dimensional nonlinear forces vs. frequency differences at various wavelengths and 0.5 inch wave amplitude.

THIS PAGE INTENTIONALLY LEFT BLANK

CHAPTER 7:
Conclusions and Recommendations

7.1 Conclusions

This study investigated the linear and nonlinear wave-induced loads on an underwater cylindrical body to empirically develop a mathematical model for predicting these loads. First, a dynamic validation test was conducted to evaluate the load cell's capability to measure small dynamic, oscillatory forces. Then, the experimental test runs were performed using the validated load cell attached to the cylindrical body.

The dynamic validation for the load cell consisted of static and dynamic load measurements. The results were compared to examine the load cell's measurement accuracy for both static and dynamic forces. Of principal interest was validating the load cell's dynamic measurement accuracy since the measured wave-induced forces on the cylindrical body are oscillatory. The results of the validation led to the conclusion that the load cell's dynamic measurements were precise, and the accuracy was not affected by having to remove the electrical offset of the load cell. Overall, the waterproof load cell used for the experimental test runs was sensitive enough to measure forces with a mean of less than 8% measurement error.

This investigation, through experimental test runs, measured the linear and nonlinear wave-induced loads on an underwater circular cylindrical body. The two-component waves at desired 0.5-inch and 1.0-inch wave amplitudes that were generated for this investigation traveled over the body and created the loads experienced by the body. The linear loads were non-dimensionalized by employing Cummins's theoretical solution, and the nonlinear loads were non-dimensionalized using the wave height of each underlying wave. From the experimental results, the behavior of the non-dimensionalized linear forces agrees with the previous study performed by Hermsen [6]. These linear forces are also consistent with the theoretical predictions of Cummins's theory. From the results of the non-dimensionalized nonlinear loads, this study developed a mathematical model by creating maps as a function of the wavelength of each of the two underlying waves. These maps in Figures 6.12, 6.11,

and 6.13 can be applied for predicting loads on an underwater vehicle in a maneuvering simulation as part of the model-based systems engineering design process.

7.2 Recommendations

This study recommends enhancing the capabilities of the test facility wavemaker to generate larger wave heights and longer wavelengths. Improving the wave maker's ability to create more wave environment combinations will allow researchers to produce more combinations wave frequency differences for experimental test runs and will enable them to have a higher confidence level that the frequency difference nonlinear results, in fact, do collapse onto a single results curve when plotted against the value of the frequency difference.

This investigation also recommends studying the linear and nonlinear wave-induced loads interacting with other cross-sectional shaped bodies such as a square and rectangular. Since no theoretical predictions exist for nonlinear loads on arbitrary shaped geometries, experimental testing is essential to understand how vehicle geometry affects nonlinear loads. Then, from the results, models can be developed to predict the loads on an underwater vehicle of arbitrary shape for a variety of wave heights.

APPENDIX A:
Engineering Drawings of the Load Cell Adapters

Figures A.1 and A.2 show the engineering drawings for the load cell's connector side and the payload side adapters, respectively. All measurements are in inches on the drawings. SolidWorks modeling design software was used to draw the design of the adapters according to the load cell dimensions shown in Figure 2.2.

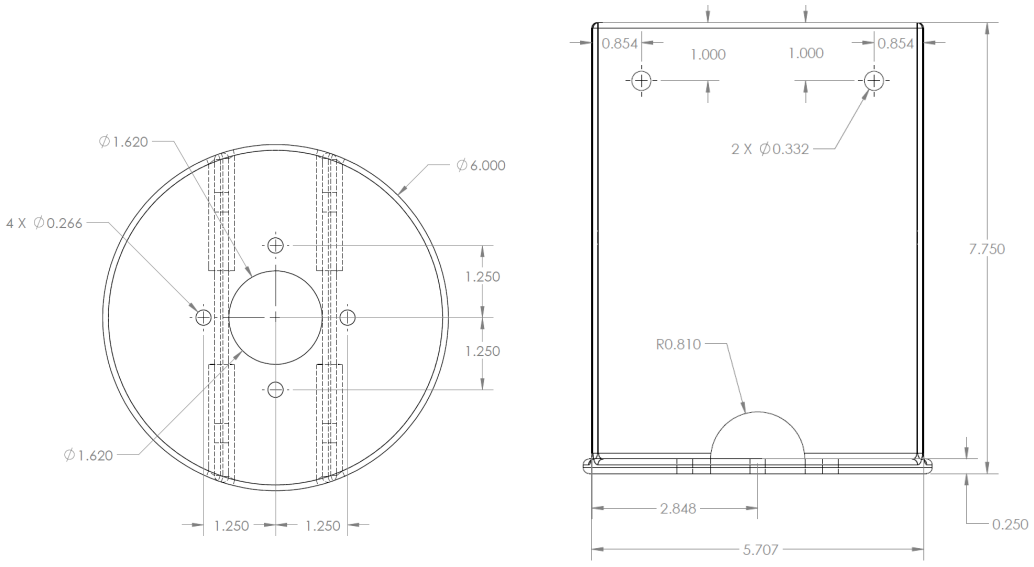

(a) Front view (b) Side view

Figure A.1. Engineering Drawings of load cell connector side adapter.

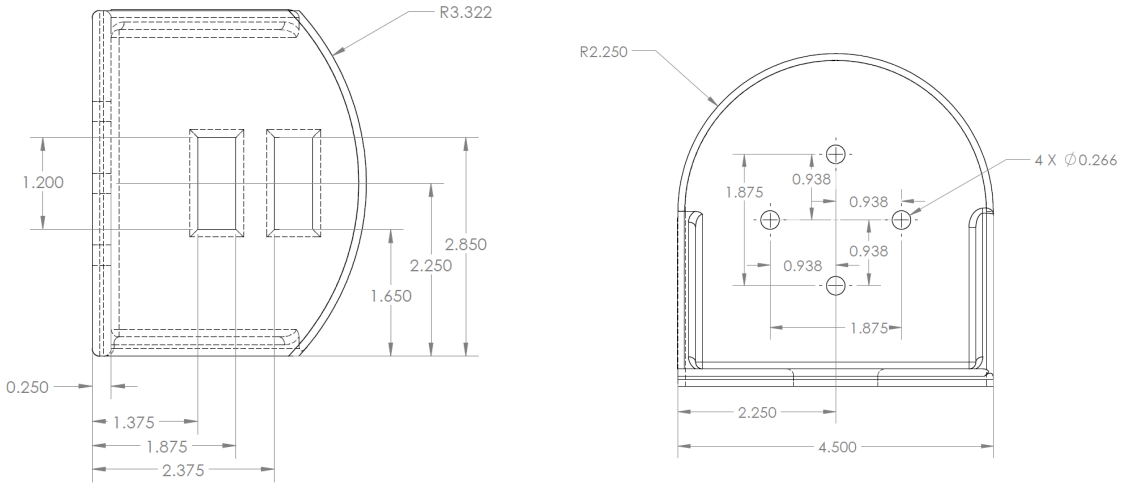

(a) Bottom view

(b) Rear view

Figure A.2. Engineering Drawings of load cell connector side adapter.

APPENDIX B:
Probes Settings on SenixVIEW Software Graphical User Interface

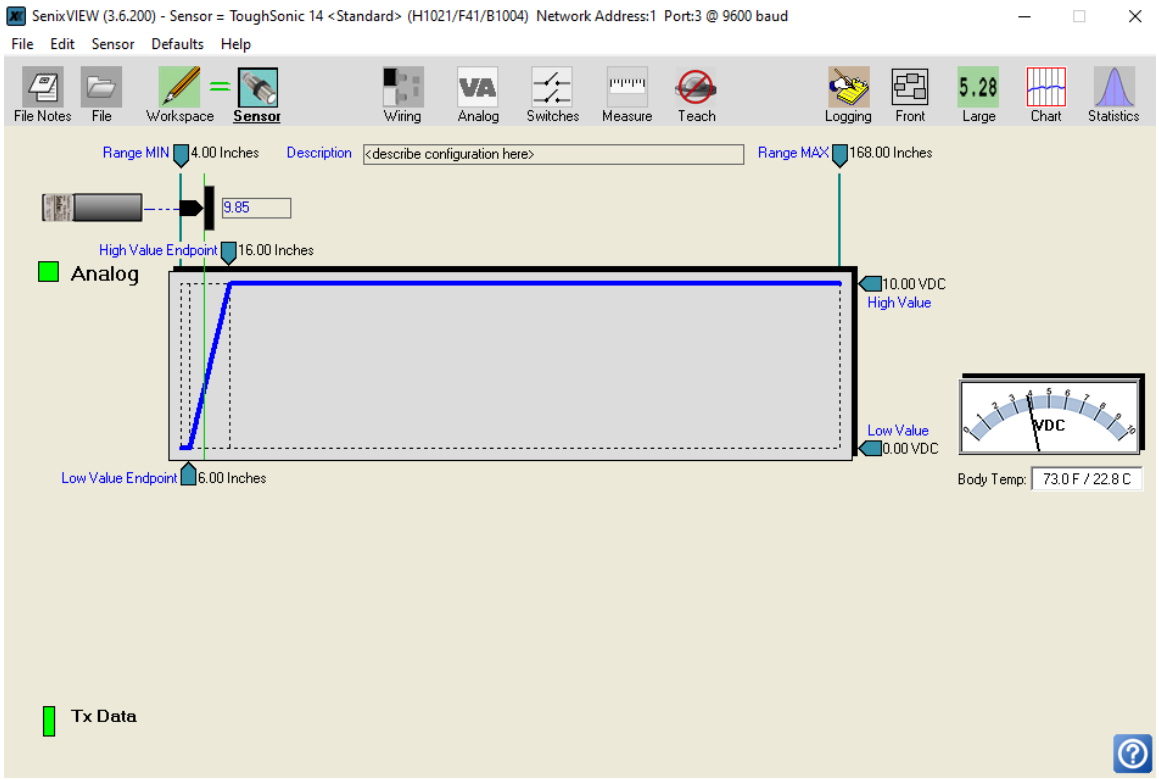

Figure B.1. Real-time SenixVIEW GUI settings for probe 1.

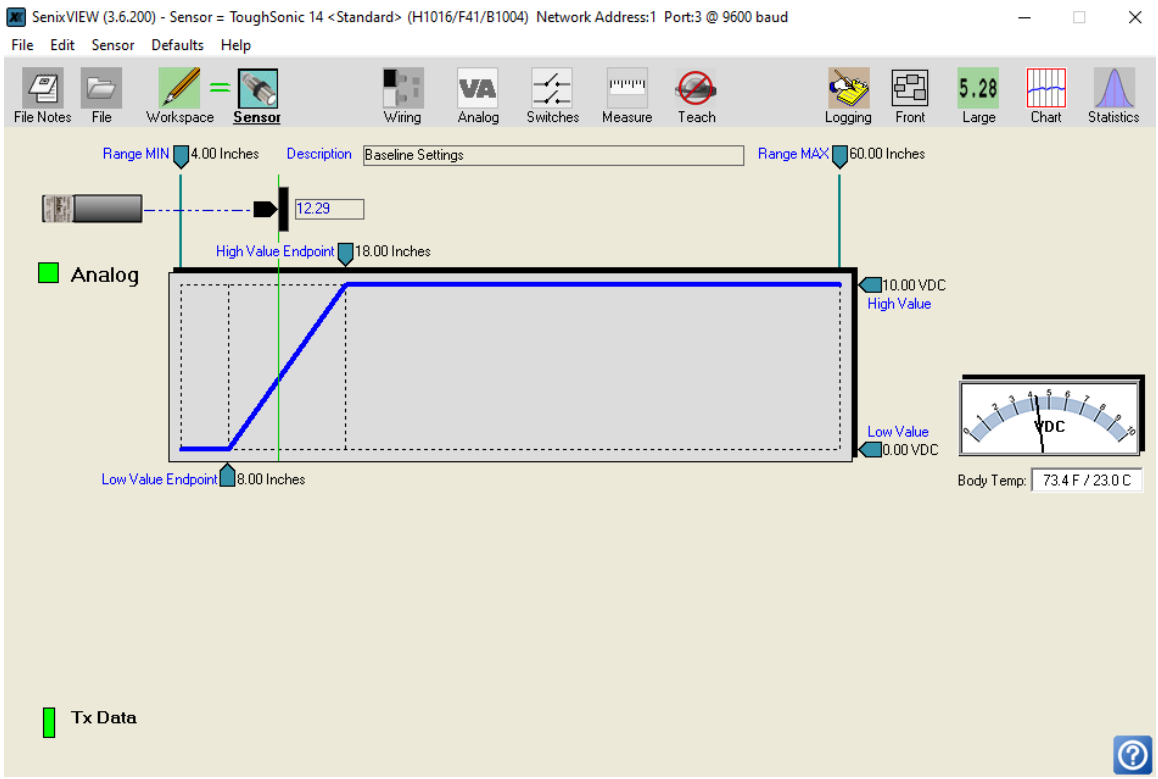

Figure B.2. Real-time SenixVIEW GUI settings for probe 2.

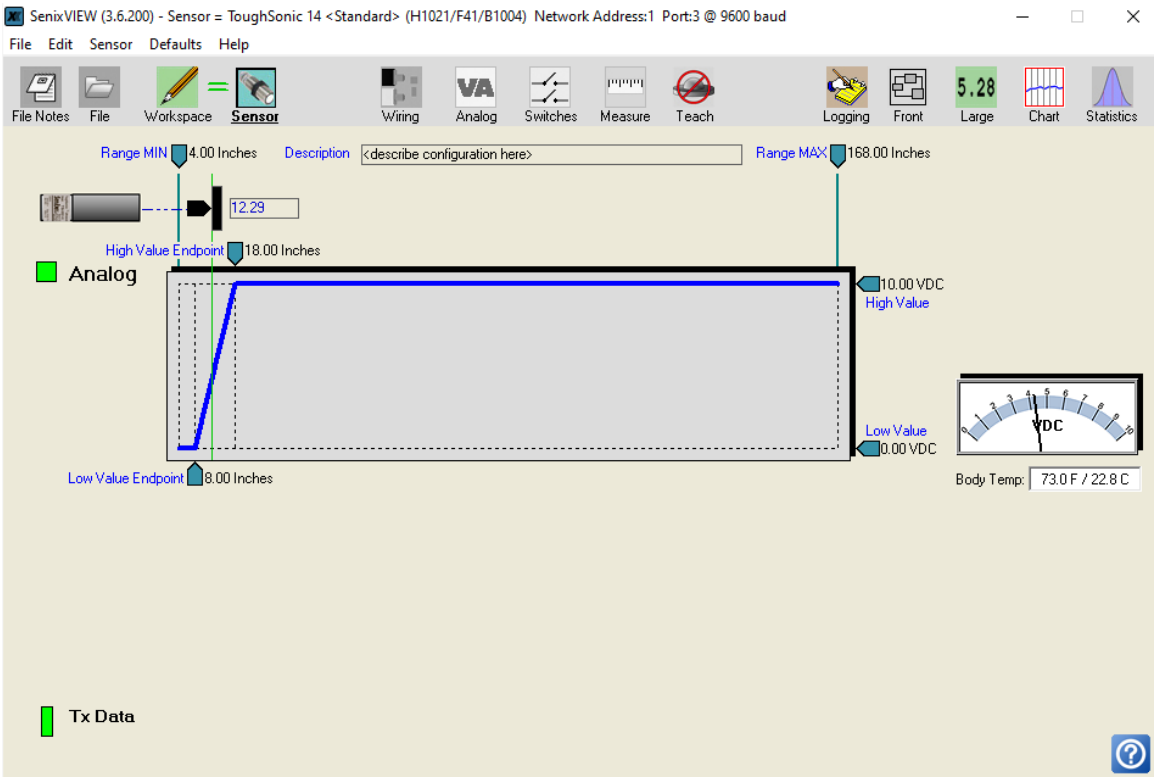

Figure B.3. Real-time SenixVIEW GUI settings for probe 3.

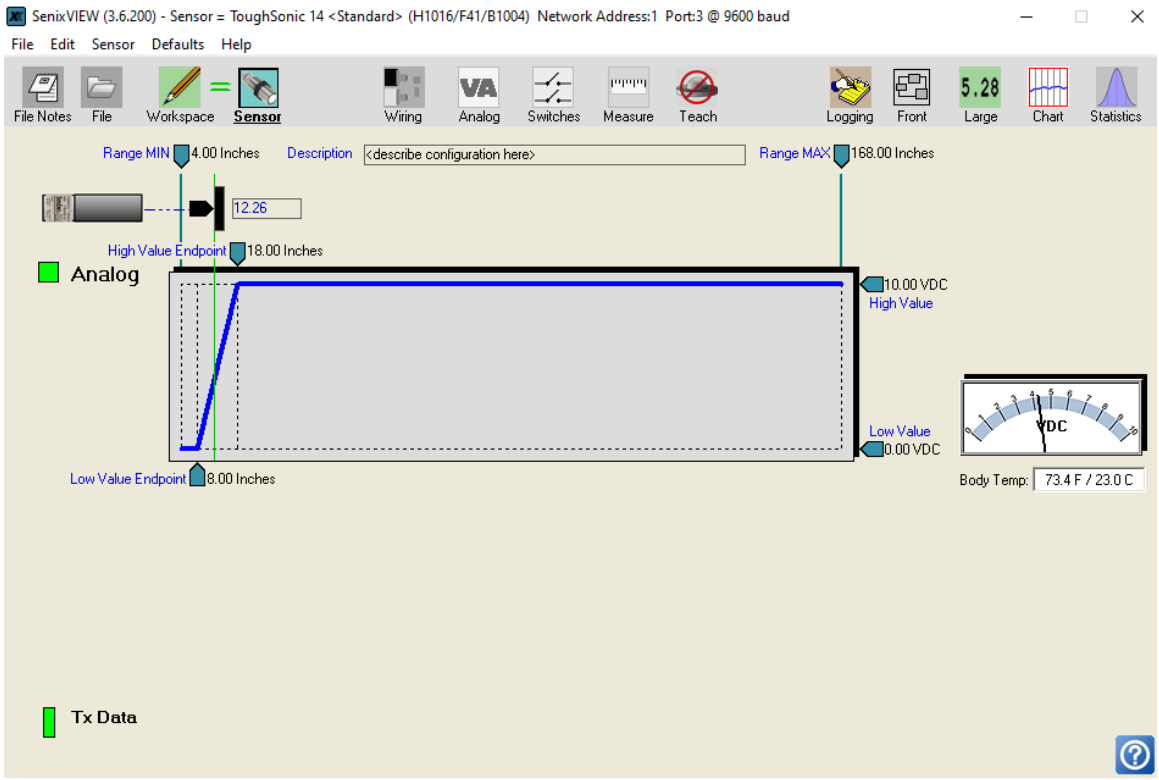

Figure B.4. Real-time SenixVIEW GUI settings for probe 4.

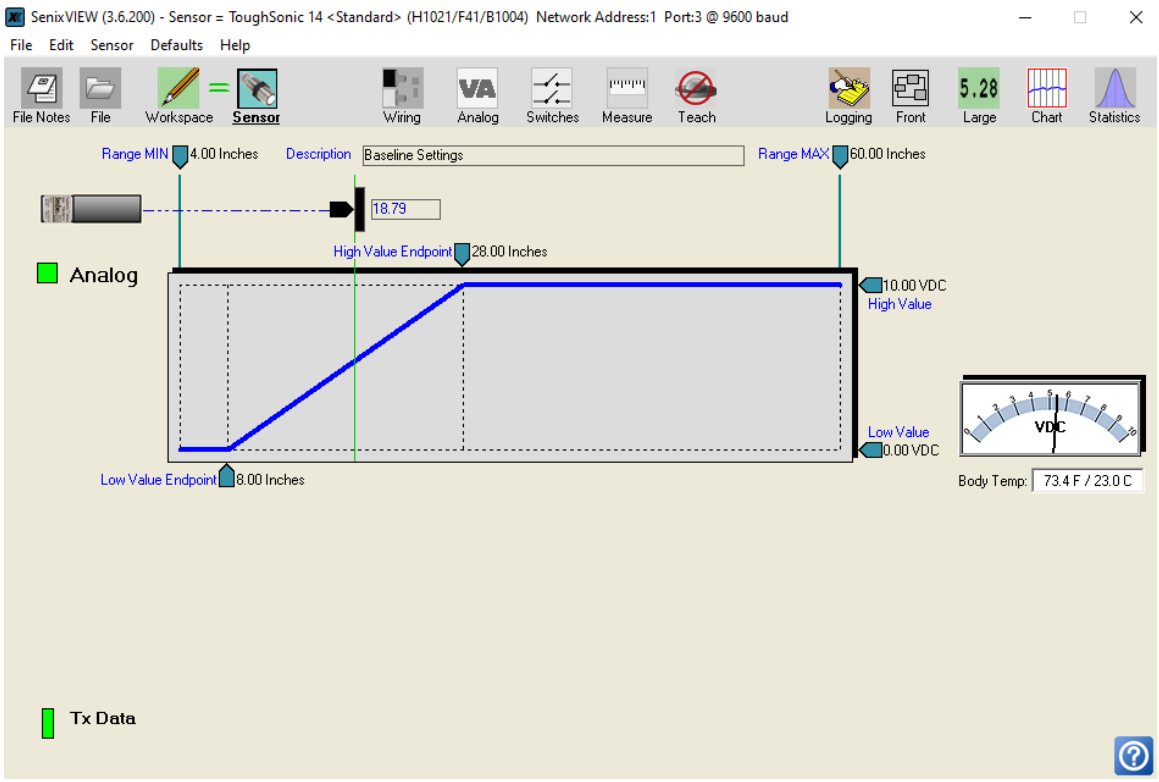

Figure B.5. Real-time SenixVIEW GUI settings for wedge probe.

THIS PAGE INTENTIONALLY LEFT BLANK

APPENDIX C:
Dynamic Validation Test Matrix

Table C.1. Dynamic validation test matrix.

Beginning of Table							
Run Number	Weight (lbs)	Sampling Rate (Hz)	Static Collection Length (sec)	Dynamic Collection Length (sec)	Zero Before Run (Y or N)	Load Cell Capacity (lbs)	Notes
Load Cell Orientation: $+F_x$ (left), $+F_y$ (up), $+F_z$ (in)							
14	0.00	25	0	30	Y	500	poke test
15	0.50	25	30	60	Y	500	signal on F_y
16	0.25	25	30	60	Y	500	signal on F_y
17	0.15	25	30	60	N	500	signal on F_y
18	1.00	25	30	60	N	500	signal on F_y
19	0.20	25	30	60	N	500	signal on F_y
20	0.10	25	30	60	N	500	signal on F_y
21	0.30	25	30	60	Y	500	signal on F_y
22	0.05	25	30	60	N	500	signal on F_y
23	0.50	25	30	60	N	500	signal on F_y
24	0.25	25	30	60	N	500	signal on F_y
25	0.15	25	30	60	N	500	signal on F_y
26	1.00	25	30	60	Y	500	signal on F_y
27	0.20	25	30	60	N	500	signal on F_y
28	0.10	25	30	60	N	500	signal on F_y
29	0.30	25	30	60	N	500	signal on F_y
30	0.05	25	30	60	N	500	signal on F_y
31	0.50	25	30	60	Y	500	signal on F_y
32	0.25	25	30	60	N	500	signal on F_y

Continuation of Table C.1							
Run Number	Weight (lbs)	Sampling Rate (Hz)	Static Collection Length (sec)	Dynamic Collection Length (sec)	Zero Before Run (Y or N)	Load Cell Capacity (lbs)	Notes
33	0.15	25	30	60	N	500	signal on F_y
34	1.00	25	30	60	N	500	signal on F_y
35	0.20	25	30	60	N	500	signal on F_y
36	0.10	25	30	60	Y	500	signal on F_y
37	0.30	25	30	60	N	500	signal on F_y
38	0.05	25	30	60	N	500	signal on F_y
39	0.50	25	30	60	N	500	signal on F_y
40	0.25	25	30	60	N	500	signal on F_y
41	0.15	25	30	60	Y	500	signal on F_y
42	1.00	25	30	60	N	500	signal on F_y
43	0.20	25	30	60	N	500	signal on F_y
44	0.10	25	30	60	N	500	signal on F_y
45	0.30	25	30	60	N	500	signal on F_y
46	0.05	25	30	60	Y	500	signal on F_y
47	0.50	25	30	60	N	500	signal on F_y
48	0.25	25	30	60	N	500	signal on F_y
49	0.15	25	30	60	N	500	signal on F_y
50	1.00	25	30	60	N	500	signal on F_y
51	0.20	25	30	60	Y	500	signal on F_y
52	0.10	25	30	60	N	500	signal on F_y
53	0.30	25	30	60	N	500	signal on F_y
54	0.05	25	30	60	N	500	signal on F_y
Load Cell Orientation: $+F_x$ (down), $+F_y$ (left), $+F_z$ (in)							
55	0.00	25	0	30	N	500	poke test
56	0.10	25	30	60	Y	500	signal on F_x
57	0.30	25	30	60	N	500	signal on F_x
58	0.50	25	30	60	N	500	signal on F_x
59	0.25	25	30	60	N	500	signal on F_x

Continuation of Table C.1							
Run Number	Weight (lbs)	Sampling Rate (Hz)	Static Collection Length (sec)	Dynamic Collection Length (sec)	Zero Before Run (Y or N)	Load Cell Capacity (lbs)	Notes
60	0.15	25	30	60	N	500	signal on F_x
61	1.00	25	30	60	Y	500	signal on F_x
62	0.20	25	30	60	N	500	signal on F_x
63	0.10	25	30	60	N	500	signal on F_x
64	0.30	25	30	60	N	500	signal on F_x
65	0.50	25	30	60	N	500	signal on F_x
66	0.25	25	30	60	Y	500	signal on F_x
67	0.15	25	30	60	N	500	signal on F_x
68	1.00	25	30	60	N	500	signal on F_x
69	0.20	25	30	60	N	500	signal on F_x
70	0.10	25	30	60	N	500	signal on F_x
71	0.30	25	30	60	Y	500	signal on F_x
72	0.50	25	30	60	N	500	signal on F_x
73	0.25	25	30	60	N	500	signal on F_x
74	0.15	25	30	60	N	500	signal on F_x
75	1.00	25	30	60	N	500	signal on F_x
76	0.20	25	30	60	Y	500	signal on F_x
End of Table							

THIS PAGE INTENTIONALLY LEFT BLANK

APPENDIX D:
Experimental Test Matrices

Table D.1. Test Matrix: d=1.5D, $\lambda/L = 1.0$.

water depth =	3.166666667	(ft)	
max wave lenth =	6.333333333	(ft)	
Desired Wave Height =	2	(inches)	
model length =	30	(inches)	

a_wave / a_wedge = Af^2+Bf+C	
A =	-0.2253755
B =	1.5621619
C =	-0.5258382

	desired lambda / L (---)	required wave length (ft)	steepness (---)	k (1/ft)	sigma (---)	omega (rad/s)	freq (Hz)	wedge actual (in)	wedge CMD (mm)	ITERATED wedge CMD (mm)	Run # 1044 1249
Constant	1.0000	2.500	30	2.51327	1	9.04150508	1.462	0.398272073	20.232		
1	0.7500	1.875	11.25	3.35103	1	10.7807157	1.716	0.670680076	34.071	33.500	1044
2	0.8125	2.031	12.1875	3.09326	1	10.3022067	1.640	0.699473393	35.533	37.670	
3	0.8750	2.188	13.125	2.87231	1	9.88475919	1.573	0.727819508	36.973	38.756	1048
4	0.9375	2.344	14.0625	2.68083	1	9.51617748	1.515	0.75577166	38.393	39.830	1191
5	1.0000	2.500	15	2.51327	1	9.18744091	1.462	0.783380019	39.796	40.893	
6	1.0625	2.656	15.9375	2.36543	1	8.89171561	1.415	0.810690233	41.183	41.947	1203
7	1.1250	2.813	16.875	2.23402	1	8.62371633	1.373	0.837743225	42.557	42.991	1051
8	1.1875	2.969	17.8125	2.11644	1	8.37928146	1.334	0.864575507	43.920	44.028	1214
9	1.2500	3.125	18.75	2.01062	0.99999	8.155082	1.298	0.891219679	45.274	45.057	1055
10	1.3125	3.281	19.6875	1.91488	0.99999	7.94841767	1.265	0.917704976	46.619	46.081	1226
11	1.3750	3.438	20.625	1.82784	0.99998	7.75707078	1.235	0.944057786	47.958	47.098	1057
12	1.4375	3.594	21.5625	1.74836	0.99997	7.57919965	1.206	0.970302118	49.291	48.111	1227
13	1.5000	3.750	22.5	1.67552	0.99995	7.41325948	1.180	0.996460026	50.620	49.119	1053
14	1.5625	3.906	23.4375	1.6085	0.99992	7.2579427	1.155	1.022551968	51.946	50.124	1239
15	1.6250	4.063	24.375	1.54663	0.99989	7.11213341	1.132	1.048597118	53.269	51.125	1060
16	1.6875	4.219	25.3125	1.48935	0.99984	6.97487217	1.110	1.07461363	54.590	52.123	1249
17	1.7500	4.375	26.25	1.43616	0.99978	6.84532845	1.089	1.100618867	55.911	53.119	1046
18	1.8750	4.688	28.125	1.34041	0.99959	6.60658946	1.051	1.152662076	58.555	55.105	1052
19	2.0000	5.000	30	1.25664	0.9993	6.39112414	1.017	1.204856127	61.207	57.085	1049
20	2.1250	5.313	31.875	1.18272	0.99888	6.1951865	0.986	1.257326777	63.872	59.063	1054
21	2.2500	5.625	33.75	1.11701	0.99831	6.01579912	0.957	1.31019867	66.558	61.040	1059
22	2.3750	5.938	35.625	1.05822	0.99755	5.85056233	0.931	1.363596931	69.271	63.018	1047
23	2.5000	6.250	37.5	1.00531	0.99657	5.69751952	0.907	1.417648141	72.017	65.000	1056
24	2.6250	6.563	39.375	0.95744	0.99536	5.55505966	0.884	1.472480932	74.802	66.987	1061
25	2.7500	6.875	41.25	0.91392	0.99389	5.42184524	0.863	1.528226372	77.634	68.980	1050
26	2.8750	7.188	43.125	0.87418	0.99215	5.29675793	0.843	1.585018248	80.519	70.980	1058
27	3.0000	7.500	45	0.83776	0.99012	5.17885678	0.824	1.642993332	83.464	72.990	1045

Table D.2. Test Matrix: d=1.5D, $\lambda/L = 1.25$.

water depth =	3.166666667	(ft)	
max wave lenth =	6.333333333	(ft)	
Desired Wave Height =	2	(inches)	
model length =	30	(inches)	

a_wave / a_wedge = Af^2+Bf+C	
A =	-0.2253755
B =	1.5621619
C =	-0.5258382

	desired lambda / L (---)	required wave length (ft)	steepness (---)	k (1/ft)	sigma (---)	omega (rad/s)	freq (Hz)	wedge actual (in)	wedge CMD (mm)	ITERATED wedge CMD (mm)	Run # 1112 1130	Run # 1132 1150
Constant	1.2500	3.750	45	1.67552	0.99995	7.35990172	1.285	0.502620416	22.904			
1	0.7500	1.875	11.25	3.35103	1	10.7807157	1.716	0.670680076	34.071	33.500	1112	1140
2	0.8125	2.031	12.1875	3.09326	1	10.3022067	1.640	0.699473393	35.533	37.670		
3	0.8750	2.188	13.125	2.87231	1	9.88475919	1.573	0.727819508	36.973	38.756	1123	1147
4	0.9375	2.344	14.0625	2.68083	1	9.51617748	1.515	0.75577166	38.393	39.830		
5	1.0000	2.500	15	2.51327	1	9.18744091	1.462	0.783380019	39.796	40.893	1125	1132
6	1.0625	2.656	15.9375	2.36543	1	8.89171561	1.415	0.810690233	41.183	41.947		
7	1.1250	2.813	16.875	2.23402	1	8.62371633	1.373	0.837743225	42.557	42.991	1116	1141
8	1.1875	2.969	17.8125	2.11644	1	8.37928146	1.334	0.864575507	43.920	44.028		
9	1.2500	3.125	18.75	2.01062	0.99999	8.155082	1.298	0.891219679	45.274	45.057		
10	1.3125	3.281	19.6875	1.91488	0.99999	7.94841767	1.265	0.917704976	46.619	46.081		
11	1.3750	3.438	20.625	1.82784	0.99998	7.75707078	1.235	0.944057786	47.958	47.098	1121	1145
12	1.4375	3.594	21.5625	1.74836	0.99997	7.57919965	1.206	0.970302118	49.291	48.111		
13	1.5000	3.750	22.5	1.67552	0.99995	7.41325948	1.180	0.996460026	50.620	49.119	1127	1136
14	1.5625	3.906	23.4375	1.6085	0.99992	7.2579427	1.155	1.022551968	51.946	50.124		
15	1.6250	4.063	24.375	1.54663	0.99989	7.11213341	1.132	1.048597118	53.269	51.125	1118	1144
16	1.6875	4.219	25.3125	1.48935	0.99984	6.97487217	1.110	1.07461363	54.590	52.123		
17	1.7500	4.375	26.25	1.43616	0.99978	6.84532845	1.089	1.100618867	55.911	53.119	1114	1133
18	1.8750	4.688	28.125	1.34041	0.99959	6.60658946	1.051	1.152662076	58.555	55.105	1124	1148
19	2.0000	5.000	30	1.25664	0.9993	6.39112414	1.017	1.204856127	61.207	57.085	1129	1137
20	2.1250	5.313	31.875	1.18272	0.99888	6.1951865	0.986	1.257326777	63.872	59.063	1117	1150
21	2.2500	5.625	33.75	1.11701	0.99831	6.01579912	0.957	1.31019867	66.558	61.040	1126	1138
22	2.3750	5.938	35.625	1.05822	0.99755	5.85056233	0.931	1.363596931	69.271	63.018	1130	1146
23	2.5000	6.250	37.5	1.00531	0.99657	5.69751952	0.907	1.417648141	72.017	65.000	1115	1134
24	2.6250	6.563	39.375	0.95744	0.99536	5.55505966	0.884	1.472480932	74.802	66.987	1122	1149
25	2.7500	6.875	41.25	0.91392	0.99389	5.42184524	0.863	1.528226372	77.634	68.980	1119	1139
26	2.8750	7.188	43.125	0.87418	0.99215	5.29675793	0.843	1.585018248	80.519	70.980	1128	1143
27	3.0000	7.500	45	0.83776	0.99012	5.17885678	0.824	1.642993332	83.464	72.990	1113	1135

Table D.3. Test Matrix: d=1.5D, $\lambda/L = 1.50$.

water depth =	3.166666667	(ft)	
max wave lenth =	6.333333333	(ft)	
Desired Wave Height =	2	(inches)	
model length =	30	(inches)	

a_wave / a_wedge = Af^2+Bf+C	
A =	-0.2253755
B =	1.5621619
C =	-0.5258382

	desired lambda / L (---)	required wave length (ft)	steepness (---)	k (1/ft)	sigma (---)	omega (rad/s)	freq (Hz)	wedge actual (in)	wedge CMD (mm)	ITERATED wedge CMD (mm)	Run # 1077 1094
Constant	1.5000	3.750	45	1.67552	0.99995	7.35990172	1.171	0.502620416	25.533		
1	0.7500	1.875	11.25	3.35103	1	10.7807157	1.716	0.670680076	34.071	33.500	1077
2	0.8125	2.031	12.1875	3.09326	1	10.3022067	1.640	0.699473393	35.533	37.670	
3	0.8750	2.188	13.125	2.87231	1	9.88475919	1.573	0.727819508	36.973	38.756	1093
4	0.9375	2.344	14.0625	2.68083	1	9.51617748	1.515	0.75577166	38.393	39.830	
5	1.0000	2.500	15	2.51327	1	9.18744091	1.462	0.783380019	39.796	40.893	1082
6	1.0625	2.656	15.9375	2.36543	1	8.89171561	1.415	0.810690233	41.183	41.947	
7	1.1250	2.813	16.875	2.23402	1	8.62371633	1.373	0.837743225	42.557	42.991	1089
8	1.1875	2.969	17.8125	2.11644	1	8.37928146	1.334	0.864575507	43.920	44.028	
9	1.2500	3.125	18.75	2.01062	0.99999	8.155082	1.298	0.891219679	45.274	45.057	1079
10	1.3125	3.281	19.6875	1.91488	0.99999	7.94841767	1.265	0.917704976	46.619	46.081	
11	1.3750	3.438	20.625	1.82784	0.99998	7.75707078	1.235	0.944057786	47.958	47.098	1085
12	1.4375	3.594	21.5625	1.74836	0.99997	7.57919965	1.206	0.970302118	49.291	48.111	
13	1.5000	3.750	22.5	1.67552	0.99995	7.41325948	1.180	0.996460026	50.620	49.119	
14	1.5625	3.906	23.4375	1.6085	0.99992	7.2579427	1.155	1.022551968	51.946	50.124	
15	1.6250	4.063	24.375	1.54663	0.99989	7.11213341	1.132	1.048597118	53.269	51.125	1091
16	1.6875	4.219	25.3125	1.48935	0.99984	6.97487217	1.110	1.07461363	54.590	52.123	
17	1.7500	4.375	26.25	1.43616	0.99978	6.84532845	1.089	1.100618867	55.911	53.119	1080
18	1.8750	4.688	28.125	1.34041	0.99959	6.60658946	1.051	1.152662076	58.555	55.105	1094
19	2.0000	5.000	30	1.25664	0.9993	6.39112414	1.017	1.204856127	61.207	57.085	1083
20	2.1250	5.313	31.875	1.18272	0.99888	6.1951865	0.986	1.257326777	63.872	59.063	1087
21	2.2500	5.625	33.75	1.11701	0.99831	6.01579912	0.957	1.31019867	66.558	61.040	1090
22	2.3750	5.938	35.625	1.05822	0.99755	5.85056233	0.931	1.363596931	69.271	63.018	1081
23	2.5000	6.250	37.5	1.00531	0.99657	5.69751952	0.907	1.417648141	72.017	65.000	1086
24	2.6250	6.563	39.375	0.95744	0.99536	5.55505966	0.884	1.472480932	74.802	66.987	1092
25	2.7500	6.875	41.25	0.91392	0.99389	5.42184524	0.863	1.528226372	77.634	68.980	1084
26	2.8750	7.188	43.125	0.87418	0.99215	5.29675793	0.843	1.585018248	80.519	70.980	1088
27	3.0000	7.500	45	0.83776	0.99012	5.17885678	0.824	1.642993332	83.464	72.990	1078

Table D.4. Test Matrix: d=1.5D, $\lambda/L = 1.75$.

water depth =	3.166666667	(ft)	
max wave lenth =	6.333333333	(ft)	
Desired Wave Height =	2	(inches)	
model length =	30	(inches)	

a_wave / a_wedge = Af^2+Bf+C	
A =	-0.2253755
B =	1.5621619
C =	-0.5258382

	desired lambda / L (---)	required wave length (ft)	steepness (---)	k (1/ft)	sigma (---)	omega (rad/s)	freq (Hz)	wedge actual (in)	wedge CMD (mm)	ITERATED wedge CMD (mm)	Run # 1152 1170	Run # 1172 1190
Constant	1.7500	3.750	45	1.67552	0.99995	7.35990172	1.084	0.502620416	28.148			
1	0.7500	1.875	11.25	3.35103	1	10.7807157	1.716	0.670680076	34.071	33.500	1152	1183
2	0.8125	2.031	12.1875	3.09326	1	10.3022067	1.640	0.699473393	35.533	37.670		
3	0.8750	2.188	13.125	2.87231	1	9.88475919	1.573	0.727819508	36.973	38.756	1168	1172
4	0.9375	2.344	14.0625	2.68083	1	9.51617748	1.515	0.75577166	38.393	39.830		
5	1.0000	2.500	15	2.51327	1	9.18744091	1.462	0.783380019	39.796	40.893	1157	1189
6	1.0625	2.656	15.9375	2.36543	1	8.89171561	1.415	0.810690233	41.183	41.947		
7	1.1250	2.813	16.875	2.23402	1	8.62371633	1.373	0.837743225	42.557	42.991	1160	1177
8	1.1875	2.969	17.8125	2.11644	1	8.37928146	1.334	0.864575507	43.920	44.028		
9	1.2500	3.125	18.75	2.01062	0.99999	8.155082	1.298	0.891219679	45.274	45.057	1170	1186
10	1.3125	3.281	19.6875	1.91488	0.99999	7.94841767	1.265	0.917704976	46.619	46.081		
11	1.3750	3.438	20.625	1.82784	0.99998	7.75707078	1.235	0.944057786	47.958	47.098	1154	1179
12	1.4375	3.594	21.5625	1.74836	0.99997	7.57919965	1.206	0.970302118	49.291	48.111		
13	1.5000	3.750	22.5	1.67552	0.99995	7.41325948	1.180	0.996460026	50.620	49.119	1163	1176
14	1.5625	3.906	23.4375	1.6085	0.99992	7.2579427	1.155	1.022551968	51.946	50.124		
15	1.6250	4.063	24.375	1.54663	0.99989	7.11213341	1.132	1.048597118	53.269	51.125	1161	1181
16	1.6875	4.219	25.3125	1.48935	0.99984	6.97487217	1.110	1.07461363	54.590	52.123		
17	1.7500	4.375	26.25	1.43616	0.99978	6.84532845	1.089	1.100618867	55.911	53.119		
18	1.8750	4.688	28.125	1.34041	0.99959	6.60658946	1.051	1.152662076	58.555	55.105	1155	1173
19	2.0000	5.000	30	1.25664	0.9993	6.39112414	1.017	1.204856127	61.207	57.085	1165	1185
20	2.1250	5.313	31.875	1.18272	0.99888	6.1951865	0.986	1.257326777	63.872	59.063	1159	1187
21	2.2500	5.625	33.75	1.11701	0.99831	6.01579912	0.957	1.31019867	66.558	61.040	1167	1174
22	2.3750	5.938	35.625	1.05822	0.99755	5.85056233	0.931	1.363596931	69.271	63.018	1156	1190
23	2.5000	6.250	37.5	1.00531	0.99657	5.69751952	0.907	1.417648141	72.017	65.000	1169	1184
24	2.6250	6.563	39.375	0.95744	0.99536	5.55505966	0.884	1.472480932	74.802	66.987	1158	1178
25	2.7500	6.875	41.25	0.91392	0.99389	5.42184524	0.863	1.528226372	77.634	68.980	1164	1180
26	2.8750	7.188	43.125	0.87418	0.99215	5.29675793	0.843	1.585018248	80.519	70.980	1166	1188
27	3.0000	7.500	45	0.83776	0.99012	5.17885678	0.824	1.642993332	83.464	72.990	1153	1175

Table D.5. Test Matrix: d=1.5D, $\lambda/L = 2.0$.

water depth =	3.166666667	(ft)	
max wave lenth =	6.333333333	(ft)	
Desired Wave Height =	2	(inches)	
model length =	30	(inches)	

a_wave / a_wedge = Af^2+Bf+C	
A =	-0.2253755
B =	1.5621619
C =	-0.5258382

	desired lambda / L (---)	required wave length (ft)	steepness (---)	k (1/ft)	sigma (---)	omega (rad/s)	freq (Hz)	wedge actual (in)	wedge CMD (mm)	ITERATED wedge CMD (mm)	Run # 1004 1013	Run # 1015 1040	Run # 1041 1043
Constant	2.0000	5.000	60	1.25664	0.9993	6.36503751	1.017	0.605775337	30.773				
1	0.7500	1.875	11.25	3.35103	1	10.7807157	1.716	0.670680076	34.071	33.500	1005	1017	
2	0.8125	2.031	12.1875	3.09326	1	10.3022067	1.640	0.699473393	35.533	37.670		1029	
3	0.8750	2.188	13.125	2.87231	1	9.88475919	1.573	0.727819508	36.973	38.756		1024	
4	0.9375	2.344	14.0625	2.68083	1	9.51617748	1.515	0.75577166	38.393	39.830		1037	
5	1.0000	2.500	15	2.51327	1	9.18744091	1.462	0.783380019	39.796	40.893	1011	1019	
6	1.0625	2.656	15.9375	2.36543	1	8.89171561	1.415	0.810690233	41.183	41.947		1035	
7	1.1250	2.813	16.875	2.23402	1	8.62371633	1.373	0.837743225	42.557	42.991		1027	
8	1.1875	2.969	17.8125	2.11644	1	8.37928146	1.334	0.864575507	43.920	44.028		1033	
9	1.2500	3.125	18.75	2.01062	0.99999	8.155082	1.298	0.891219679	45.274	45.057	1009	1022	
10	1.3125	3.281	19.6875	1.91488	0.99999	7.94841767	1.265	0.917704976	46.619	46.081		1031	
11	1.3750	3.438	20.625	1.82784	0.99998	7.75707078	1.235	0.944057786	47.958	47.098		1025	
12	1.4375	3.594	21.5625	1.74836	0.99997	7.57919965	1.206	0.970302118	49.291	48.111		1038	
13	1.5000	3.750	22.5	1.67552	0.99995	7.41325948	1.180	0.996460026	50.620	49.119	1007	1015	
14	1.5625	3.906	23.4375	1.6085	0.99992	7.2579427	1.155	1.022551968	51.946	50.124		1040	
15	1.6250	4.063	24.375	1.54663	0.99989	7.11213341	1.132	1.048597118	53.269	51.125		1026	
16	1.6875	4.219	25.3125	1.48935	0.99984	6.97487217	1.110	1.07461363	54.590	52.123		1039	
17	1.7500	4.375	26.25	1.43616	0.99978	6.84532845	1.089	1.100618867	55.911	53.119	1012	1020	
18	1.8750	4.688	28.125	1.34041	0.99959	6.60658946	1.051	1.152662076	58.555	55.105		1032	
19	2.0000	5.000	30	1.25664	0.9993	6.39112414	1.017	1.204856127	61.207	57.085	1010		
20	2.1250	5.313	31.875	1.18272	0.99888	6.1951865	0.986	1.257326777	63.872	59.063		1036	
21	2.2500	5.625	33.75	1.11701	0.99831	6.01579912	0.957	1.31019867	66.558	61.040	1004	1018	
22	2.3750	5.938	35.625	1.05822	0.99755	5.85056233	0.931	1.363596931	69.271	63.018		1034	1043
23	2.5000	6.250	37.5	1.00531	0.99657	5.69751952	0.907	1.417648141	72.017	65.000	1008	1016	
24	2.6250	6.563	39.375	0.95744	0.99536	5.55505966	0.884	1.472480932	74.802	66.987		1030	1042
25	2.7500	6.875	41.25	0.91392	0.99389	5.42184524	0.863	1.528226372	77.634	68.980	1013	1023	
26	2.8750	7.188	43.125	0.87418	0.99215	5.29675793	0.843	1.585018248	80.519	70.980		1028	1041
27	3.0000	7.500	45	0.83776	0.99012	5.17885678	0.824	1.642993332	83.464	72.990	1006	1021	

Table D.6. Test Matrix: d=1.5D, $\lambda/L = 2.25$.

water depth =	3.166666667	(ft)	
max wave lenth =	6.333333333	(ft)	
Desired Wave Height =	2	(inches)	
model length =	30	(inches)	

a_wave / a_wedge = Af^2+Bf+C	
A =	-0.2253755
B =	1.5621619
C =	-0.5258382

	desired lambda / L (---)	required wave length (ft)	steepness (---)	k (1/ft)	sigma (---)	omega (rad/s)	freq (Hz)	wedge actual (in)	wedge CMD (mm)	ITERATED wedge CMD (mm)	Run # 1228 1245	Run # 1246 1263
Constant	2.2500	3.750	45	1.67552	0.99995	7.35990172	0.954	0.502620416	33.433			
1	0.7500	1.875	11.25	3.35103	1	10.7807157	1.716	0.670680076	34.071	33.500	1228	1253
2	0.8125	2.031	12.1875	3.09326	1	10.3022067	1.640	0.699473393	35.533	37.670		
3	0.8750	2.188	13.125	2.87231	1	9.88475919	1.573	0.727819508	36.973	38.756	1237	1261
4	0.9375	2.344	14.0625	2.68083	1	9.51617748	1.515	0.75577166	38.393	39.830		
5	1.0000	2.500	15	2.51327	1	9.18744091	1.462	0.783380019	39.796	40.893	1243	1252
6	1.0625	2.656	15.9375	2.36543	1	8.89171561	1.415	0.810690233	41.183	41.947		
7	1.1250	2.813	16.875	2.23402	1	8.62371633	1.373	0.837743225	42.557	42.991	1232	1257
8	1.1875	2.969	17.8125	2.11644	1	8.37928146	1.334	0.864575507	43.920	44.028		
9	1.2500	3.125	18.75	2.01062	0.99999	8.155082	1.298	0.891219679	45.274	45.057	1245	1255
10	1.3125	3.281	19.6875	1.91488	0.99999	7.94841767	1.265	0.917704976	46.619	46.081		
11	1.3750	3.438	20.625	1.82784	0.99998	7.75707078	1.235	0.944057786	47.958	47.098	1235	1263
12	1.4375	3.594	21.5625	1.74836	0.99997	7.57919965	1.206	0.970302118	49.291	48.111		
13	1.5000	3.750	22.5	1.67552	0.99995	7.41325948	1.180	0.996460026	50.620	49.119	1242	1246
14	1.5625	3.906	23.4375	1.6085	0.99992	7.2579427	1.155	1.022551968	51.946	50.124		
15	1.6250	4.063	24.375	1.54663	0.99989	7.11213341	1.132	1.048597118	53.269	51.125	1233	1260
16	1.6875	4.219	25.3125	1.48935	0.99984	6.97487217	1.110	1.07461363	54.590	52.123		
17	1.7500	4.375	26.25	1.43616	0.99978	6.84532845	1.089	1.100618867	55.911	53.119	1229	1251
18	1.8750	4.688	28.125	1.34041	0.99959	6.60658946	1.051	1.152662076	58.555	55.105	1244	1258
19	2.0000	5.000	30	1.25664	0.9993	6.39112414	1.017	1.204856127	61.207	57.085	1240	1256
20	2.1250	5.313	31.875	1.18272	0.99888	6.1951865	0.986	1.257326777	63.872	59.063	1236	1247
21	2.2500	5.625	33.75	1.11701	0.99831	6.01579912	0.957	1.31019867	66.558	61.040		
22	2.3750	5.938	35.625	1.05822	0.99755	5.85056233	0.931	1.363596931	69.271	63.018	1230	1250
23	2.5000	6.250	37.5	1.00531	0.99657	5.69751952	0.907	1.417648141	72.017	65.000	1241	1262
24	2.6250	6.563	39.375	0.95744	0.99536	5.55505966	0.884	1.472480932	74.802	66.987	1234	1254
25	2.7500	6.875	41.25	0.91392	0.99389	5.42184524	0.863	1.528226372	77.634	68.980	1238	1259
26	2.8750	7.188	43.125	0.87418	0.99215	5.29675793	0.843	1.585018248	80.519	70.980	1231	1248
27	3.0000	7.500	45	0.83776	0.99012	5.17885678	0.824	1.642993332	83.464	72.990		

Table D.7. Test Matrix: d=1.5D, $\lambda/L = 2.5$.

water depth =	3.16666667	(ft)	
max wave lenth =	6.33333333	(ft)	
Desired Wave Height =	2	(inches)	
model length =	30	(inches)	

a_wave / a_wedge = Af^2+Bf+C	
A =	-0.2253755
B =	1.5621619
C =	-0.5258382

	desired lambda / L (---)	required wave length (ft)	steepness (---)	k (1/ft)	sigma (---)	omega (rad/s)	freq (Hz)	wedge actual (in)	wedge CMD (mm)	ITERATED wedge CMD (mm)	Run # 1095 1110	Run # 1264 1264
Constant	2.5000	6.250	75	1.00531	0.99657	5.68250626	0.904	0.711605675	36.150			
1	0.7500	1.875	11.25	3.35103	1	10.7807157	1.716	0.670680076	34.071	33.500	1095	
2	0.8125	2.031	12.1875	3.09326	1	10.3022067	1.640	0.699473393	35.533	37.670		
3	0.8750	2.188	13.125	2.87231	1	9.88475919	1.573	0.727819508	36.973	38.756	1109	
4	0.9375	2.344	14.0625	2.68083	1	9.51617748	1.515	0.75577166	38.393	39.830		1264
5	1.0000	2.500	15	2.51327	1	9.18744091	1.462	0.783380019	39.796	40.893	1101	
6	1.0625	2.656	15.9375	2.36543	1	8.89171561	1.415	0.810690233	41.183	41.947		
7	1.1250	2.813	16.875	2.23402	1	8.62371633	1.373	0.837743225	42.557	42.991	1107	
8	1.1875	2.969	17.8125	2.11644	1	8.37928146	1.334	0.864575507	43.920	44.028		
9	1.2500	3.125	18.75	2.01062	0.99999	8.155082	1.298	0.891219679	45.274	45.057	1099	
10	1.3125	3.281	19.6875	1.91488	0.99999	7.94841767	1.265	0.917704976	46.619	46.081		
11	1.3750	3.438	20.625	1.82784	0.99998	7.75707078	1.235	0.944057786	47.958	47.098	1104	
12	1.4375	3.594	21.5625	1.74836	0.99997	7.57919965	1.206	0.970302118	49.291	48.111		
13	1.5000	3.750	22.5	1.67552	0.99995	7.41325948	1.180	0.996460026	50.620	49.119	1102	
14	1.5625	3.906	23.4375	1.6085	0.99992	7.2579427	1.155	1.022551968	51.946	50.124		
15	1.6250	4.063	24.375	1.54663	0.99989	7.11213341	1.132	1.048597118	53.269	51.125	1106	
16	1.6875	4.219	25.3125	1.48935	0.99984	6.97487217	1.110	1.07461363	54.590	52.123		
17	1.7500	4.375	26.25	1.43616	0.99978	6.84532845	1.089	1.100618867	55.911	53.119	1096	
18	1.8750	4.688	28.125	1.34041	0.99959	6.60658946	1.051	1.152662076	58.555	55.105	1110	
19	2.0000	5.000	30	1.25664	0.9993	6.39112414	1.017	1.204856127	61.207	57.085	1105	
20	2.1250	5.313	31.875	1.18272	0.99888	6.1951865	0.986	1.257326777	63.872	59.063	1100	
21	2.2500	5.625	33.75	1.11701	0.99831	6.01579912	0.957	1.31019867	66.558	61.040	1108	
22	2.3750	5.938	35.625	1.05822	0.99755	5.85056233	0.931	1.363596931	69.271	63.018	1097	
23	2.5000	6.250	37.5	1.00531	0.99657	5.69751952	0.907	1.417648141	72.017	65.000		
24	2.6250	6.563	39.375	0.95744	0.99536	5.55505966	0.884	1.472480932	74.802	66.987	1103	
25	2.7500	6.875	41.25	0.91392	0.99389	5.42184524	0.863	1.528226372	77.634	68.980	1098	
26	2.8750	7.188	43.125	0.87418	0.99215	5.29675793	0.843	1.585018248	80.519	70.980		
27	3.0000	7.500	45	0.83776	0.99012	5.17885678	0.824	1.642993332	83.464	72.990		

Table D.8. Test Matrix: d=1.5D, $\lambda/L = 2.75$.

water depth =	3.166666667	(ft)	
max wave lenth =	6.333333333	(ft)	
Desired Wave Height =	2	(inches)	
model length =	30	(inches)	

a_wave / a_wedge = Af^2+Bf+C	
A =	-0.2253755
B =	1.5621619
C =	-0.5258382

	desired lambda / L (---)	required wave length (ft)	steepness (---)	k (1/ft)	sigma (---)	omega (rad/s)	freq (Hz)	wedge actual (in)	wedge CMD (mm)	ITERATED wedge CMD (mm)	Run # 1192 1208	Run # 1209 1225
Constant	2.7500	3.750	45	1.67552	0.99995	7.35990172	0.861	0.502620416	38.949			
1	0.7500	1.875	11.25	3.35103	1	10.7807157	1.716	0.670680076	34.071	33.500	1192	1215
2	0.8125	2.031	12.1875	3.09326	1	10.3022067	1.640	0.699473393	35.533	37.670		
3	0.8750	2.188	13.125	2.87231	1	9.88475919	1.573	0.727819508	36.973	38.756	1200	1225
4	0.9375	2.344	14.0625	2.68083	1	9.51617748	1.515	0.75577166	38.393	39.830		
5	1.0000	2.500	15	2.51327	1	9.18744091	1.462	0.783380019	39.796	40.893	1204	1209
6	1.0625	2.656	15.9375	2.36543	1	8.89171561	1.415	0.810690233	41.183	41.947		
7	1.1250	2.813	16.875	2.23402	1	8.62371633	1.373	0.837743225	42.557	42.991	1194	1219
8	1.1875	2.969	17.8125	2.11644	1	8.37928146	1.334	0.864575507	43.920	44.028		
9	1.2500	3.125	18.75	2.01062	0.99999	8.155082	1.298	0.891219679	45.274	45.057	1206	1221
10	1.3125	3.281	19.6875	1.91488	0.99999	7.94841767	1.265	0.917704976	46.619	46.081		
11	1.3750	3.438	20.625	1.82784	0.99998	7.75707078	1.235	0.944057786	47.958	47.098	1196	1213
12	1.4375	3.594	21.5625	1.74836	0.99997	7.57919965	1.206	0.970302118	49.291	48.111		
13	1.5000	3.750	22.5	1.67552	0.99995	7.41325948	1.180	0.996460026	50.620	49.119	1198	1223
14	1.5625	3.906	23.4375	1.6085	0.99992	7.2579427	1.155	1.022551968	51.946	50.124		
15	1.6250	4.063	24.375	1.54663	0.99989	7.11213341	1.132	1.048597118	53.269	51.125	1201	1216
16	1.6875	4.219	25.3125	1.48935	0.99984	6.97487217	1.110	1.07461363	54.590	52.123		
17	1.7500	4.375	26.25	1.43616	0.99978	6.84532845	1.089	1.100618867	55.911	53.119	1195	1218
18	1.8750	4.688	28.125	1.34041	0.99959	6.60658946	1.051	1.152662076	58.555	55.105	1208	1222
19	2.0000	5.000	30	1.25664	0.9993	6.39112414	1.017	1.204856127	61.207	57.085	1199	1210
20	2.1250	5.313	31.875	1.18272	0.99888	6.1951865	0.986	1.257326777	63.872	59.063	1205	1220
21	2.2500	5.625	33.75	1.11701	0.99831	6.01579912	0.957	1.31019867	66.558	61.040	1197	1212
22	2.3750	5.938	35.625	1.05822	0.99755	5.85056233	0.931	1.363596931	69.271	63.018	1207	1224
23	2.5000	6.250	37.5	1.00531	0.99657	5.69751952	0.907	1.417648141	72.017	65.000	1202	1217
24	2.6250	6.563	39.375	0.95744	0.99536	5.55505966	0.884	1.472480932	74.802	66.987	1193	1211
25	2.7500	6.875	41.25	0.91392	0.99389	5.42184524	0.863	1.528226372	77.634	68.980		
26	2.8750	7.188	43.125	0.87418	0.99215	5.29675793	0.843	1.585018248	80.519	70.980		
27	3.0000	7.500	45	0.83776	0.99012	5.17885678	0.824	1.642993332	83.464	72.990		

Table D.9. Test Matrix: d=1.5D, $\lambda/L = 3.0$.

water depth =	3.166666667	(ft)	
max wave lenth =	6.333333333	(ft)	
Desired Wave Height =	2	(inches)	
model length =	30	(inches)	

a_wave / a_wedge = Af^2+Bf+C	
A =	-0.2253755
B =	1.5621619
C =	-0.5258382

	desired lambda / L (---)	required wave length (ft)	steepness (---)	k (1/ft)	sigma (---)	omega (rad/s)	freq (Hz)	wedge actual (in)	wedge CMD (mm)	ITERATED wedge CMD (mm)	Run # 1062 1076	Run # 1071 1182
Constant	3.0000	7.500	90	0.83776	0.99012	5.16923617	0.824	0.823965385	41.857			
1	0.7500	1.875	11.25	3.35103	1	10.7807157	1.716	0.670680076	34.071	33.500	1062	
2	0.8125	2.031	12.1875	3.09326	1	10.3022067	1.640	0.699473393	35.533	37.670		1071
3	0.8750	2.188	13.125	2.87231	1	9.88475919	1.573	0.727819508	36.973	38.756	1068	
4	0.9375	2.344	14.0625	2.68083	1	9.51617748	1.515	0.75577166	38.393	39.830		1111
5	1.0000	2.500	15	2.51327	1	9.18744091	1.462	0.783380019	39.796	40.893	1065	
6	1.0625	2.656	15.9375	2.36543	1	8.89171561	1.415	0.810690233	41.183	41.947		1182
7	1.1250	2.813	16.875	2.23402	1	8.62371633	1.373	0.837743225	42.557	42.991	1073	
8	1.1875	2.969	17.8125	2.11644	1	8.37928146	1.334	0.864575507	43.920	44.028		1120
9	1.2500	3.125	18.75	2.01062	0.99999	8.155082	1.298	0.891219679	45.274	45.057	1075	
10	1.3125	3.281	19.6875	1.91488	0.99999	7.94841767	1.265	0.917704976	46.619	46.081		1142
11	1.3750	3.438	20.625	1.82784	0.99998	7.75707078	1.235	0.944057786	47.958	47.098	1066	
12	1.4375	3.594	21.5625	1.74836	0.99997	7.57919965	1.206	0.970302118	49.291	48.111		1131
13	1.5000	3.750	22.5	1.67552	0.99995	7.41325948	1.180	0.996460026	50.620	49.119	1070	
14	1.5625	3.906	23.4375	1.6085	0.99992	7.2579427	1.155	1.022551968	51.946	50.124		1151
15	1.6250	4.063	24.375	1.54663	0.99989	7.11213341	1.132	1.048597118	53.269	51.125	1072	
16	1.6875	4.219	25.3125	1.48935	0.99984	6.97487217	1.110	1.07461363	54.590	52.123		1162
17	1.7500	4.375	26.25	1.43616	0.99978	6.84532845	1.089	1.100618867	55.911	53.119	1063	
18	1.8750	4.688	28.125	1.34041	0.99959	6.60658946	1.051	1.152662076	58.555	55.105	1074	
19	2.0000	5.000	30	1.25664	0.9993	6.39112414	1.017	1.204856127	61.207	57.085	1069	
20	2.1250	5.313	31.875	1.18272	0.99888	6.1951865	0.986	1.257326777	63.872	59.063	1076	
21	2.2500	5.625	33.75	1.11701	0.99831	6.01579912	0.957	1.31019867	66.558	61.040	1064	
22	2.3750	5.938	35.625	1.05822	0.99755	5.85056233	0.931	1.363596931	69.271	63.018	1071	
23	2.5000	6.250	37.5	1.00531	0.99657	5.69751952	0.907	1.417648141	72.017	65.000	1067	
24	2.6250	6.563	39.375	0.95744	0.99536	5.55505966	0.884	1.472480932	74.802	66.987		
25	2.7500	6.875	41.25	0.91392	0.99389	5.42184524	0.863	1.528226372	77.634	68.980		
26	2.8750	7.188	43.125	0.87418	0.99215	5.29675793	0.843	1.585018248	80.519	70.980		
27	3.0000	7.500	45	0.83776	0.99012	5.17885678	0.824	1.642993332	83.464	72.990		

THIS PAGE INTENTIONALLY LEFT BLANK

APPENDIX E:
Static and Dynamic Load Results (Signal on F_x)

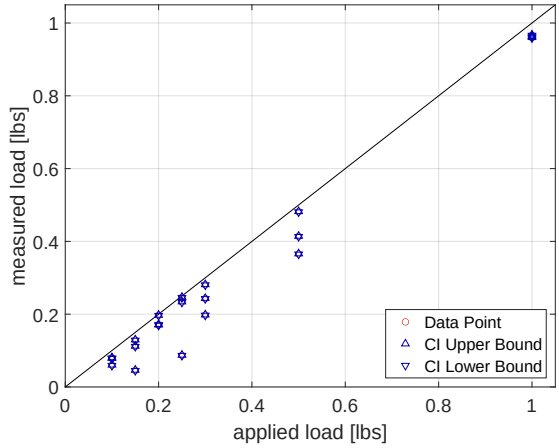

(a) static load results

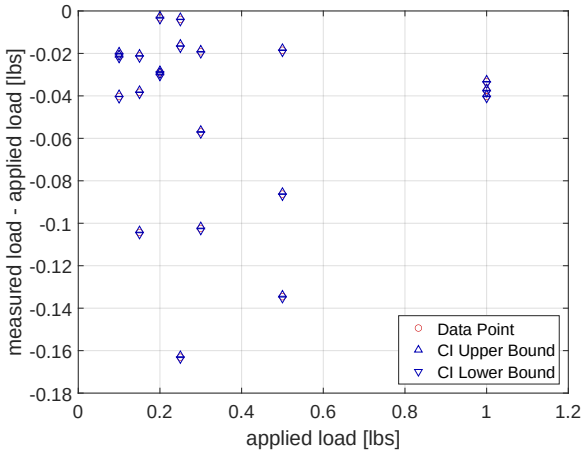

(b) static load difference results

Figure E.1. 500-lbs load cell experimental validation static results for F_x channel.

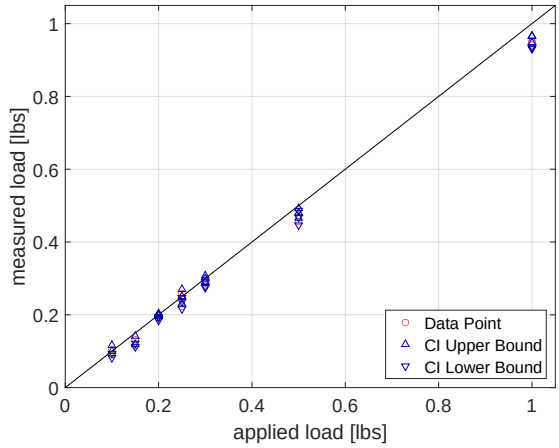

(a) dynamic load results

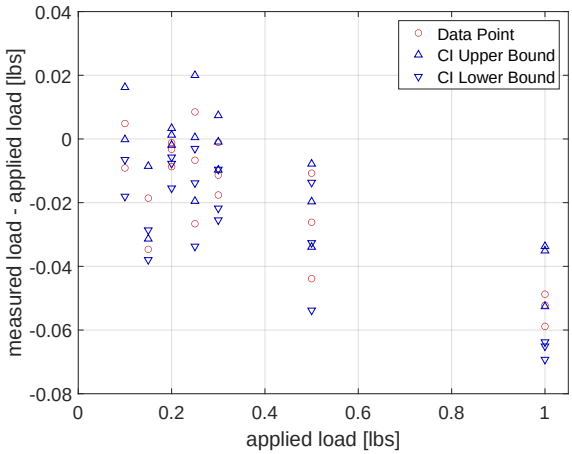

(b) dynamic load difference results

Figure E.2. 500-lbs load cell experimental validation dynamic results for F_x channel.

APPENDIX F:
Linear and Nonlinear Load Results for All Test Conditions from the Baseline Wave Environments

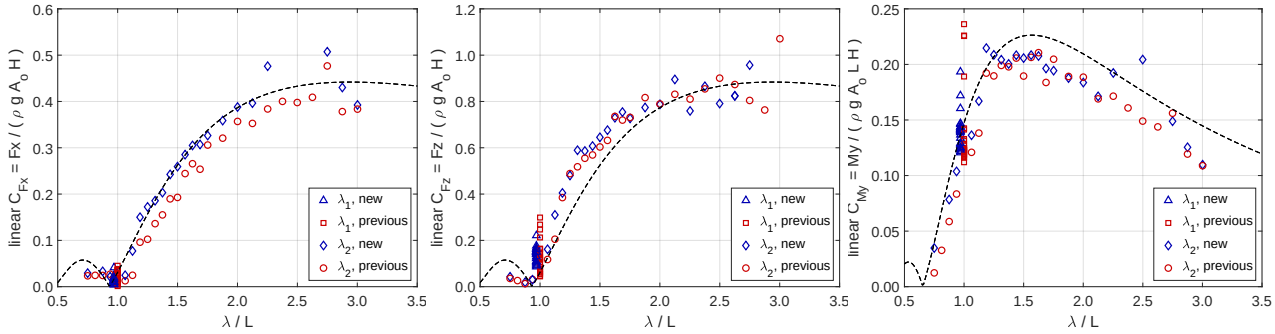

(a) F_x (b) F_z (c) M_y

Figure F.1. Comparison of measured and predicted non-dimensional linear force at $\lambda_1/L = 1.00; \lambda_2/L =$ various.

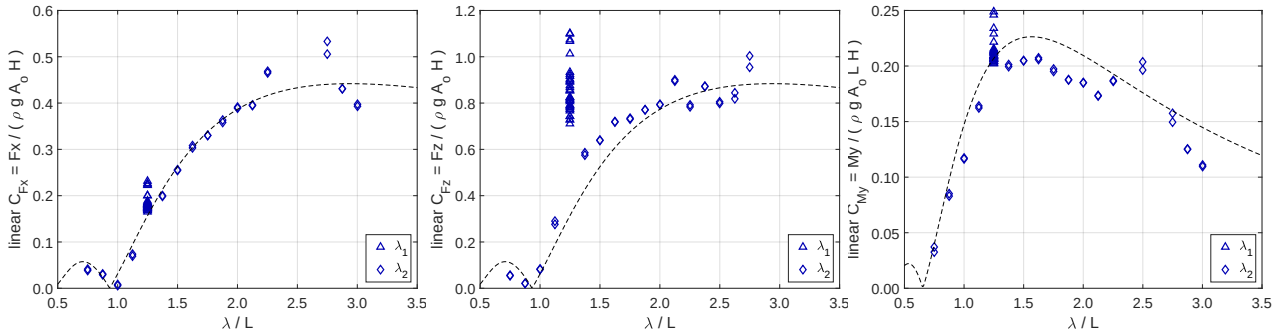

(a) F_x (b) F_z (c) M_y

Figure F.2. Comparison of measured and predicted non-dimensional linear force at $\lambda_1/L = 1.25; \lambda_2/L =$ various.

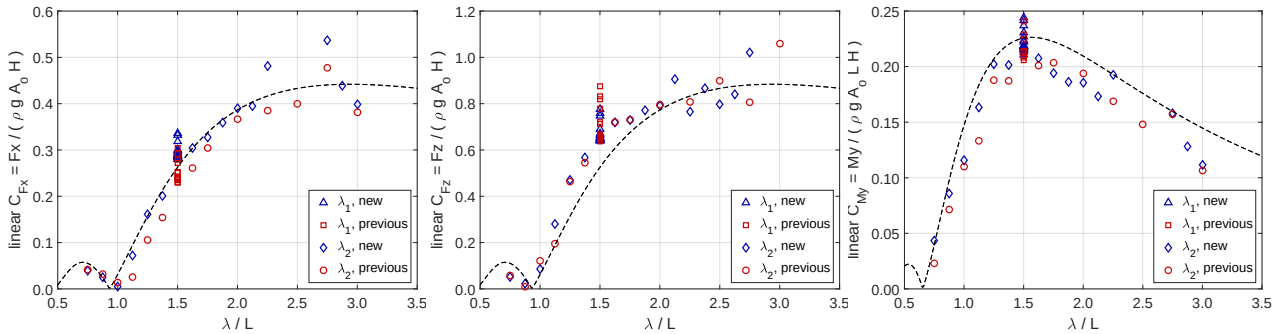

(a) F_x (b) F_z (c) M_y

Figure F.3. Comparison of measured and predicted non-dimensional linear force at $\lambda_1/L = 1.50; \lambda_2/L =$ various.

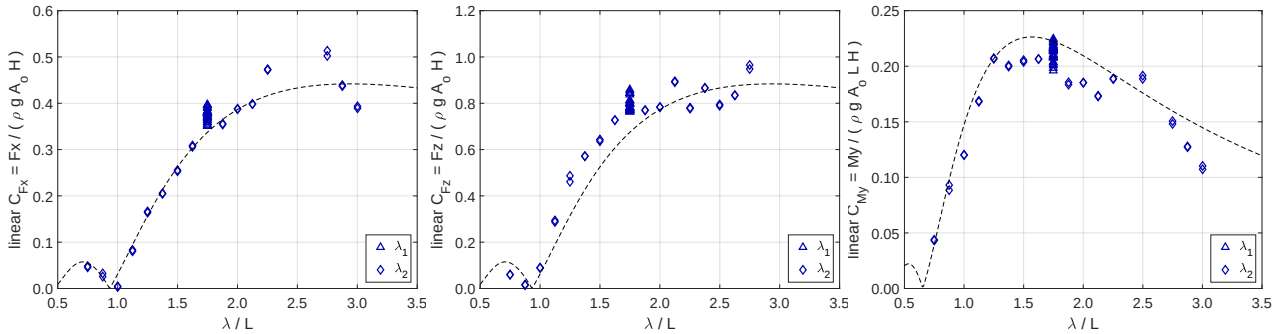

(a) F_x (b) F_z (c) M_y

Figure F.4. Comparison of measured and predicted non-dimensional linear force at $\lambda_1/L = 1.75; \lambda_2/L =$ various.

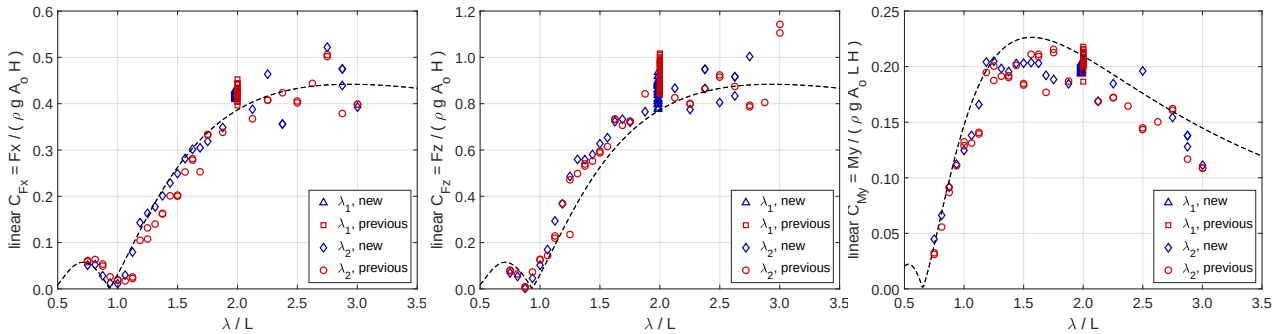

(a) F_x (b) F_z (c) M_y

Figure F.5. Comparison of measured and predicted non-dimensional linear force at $\lambda_1/L = 2.00; \lambda_2/L =$ various.

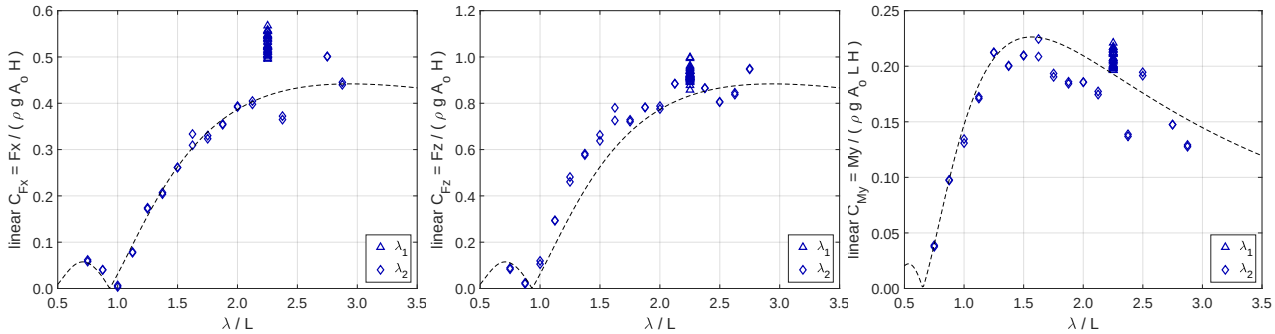

(a) F_x (b) F_z (c) M_y

Figure F.6. Comparison of measured and predicted non-dimensional linear force at $\lambda_1/L = 2.25; \lambda_2/L =$ various.

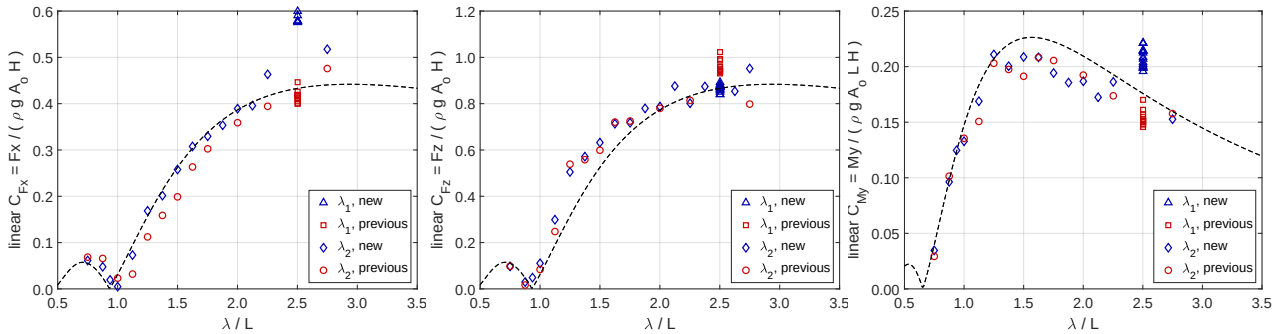

(a) F_x (b) F_z (c) M_y

Figure F.7. Comparison of measured and predicted non-dimensional linear force at $\lambda_1/L = 2.50; \lambda_2/L =$ various.

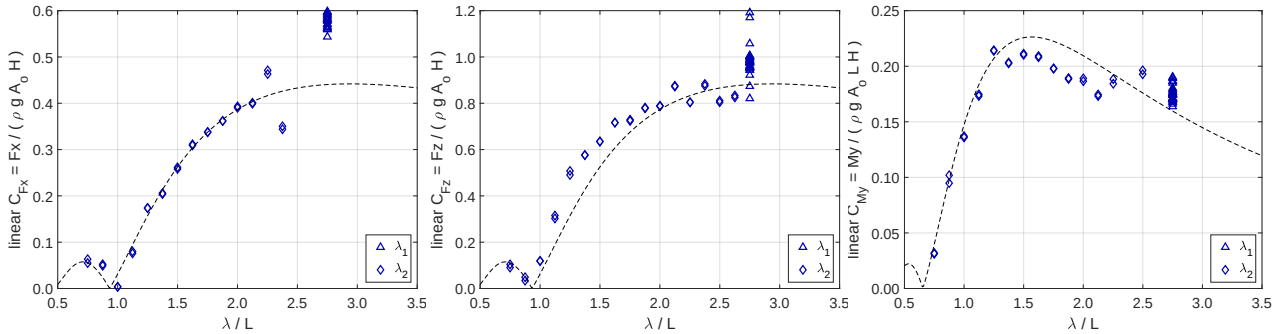

(a) F_x (b) F_z (c) M_y

Figure F.8. Comparison of measured and predicted non-dimensional linear force at $\lambda_1/L = 2.75; \lambda_2/L =$ various.

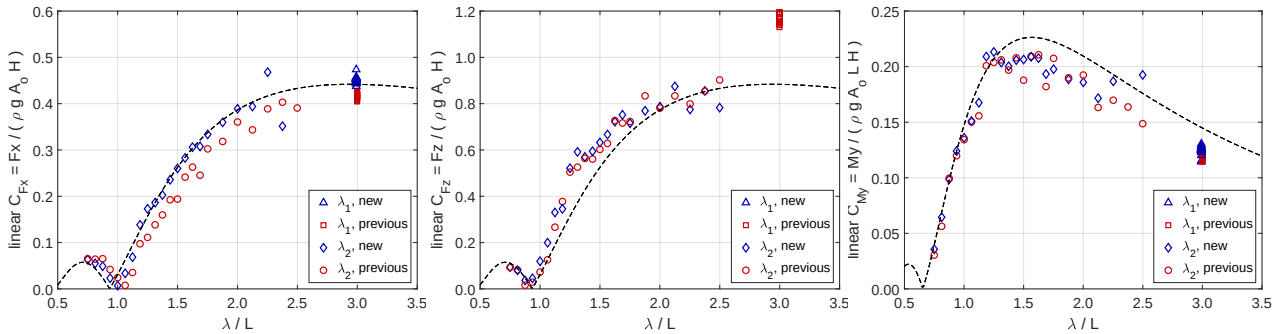

(a) F_x (b) F_z (c) M_y

Figure F.9. Comparison of measured and predicted non-dimensional linear force at $\lambda_1/L = 3.00; \lambda_2/L =$ various.

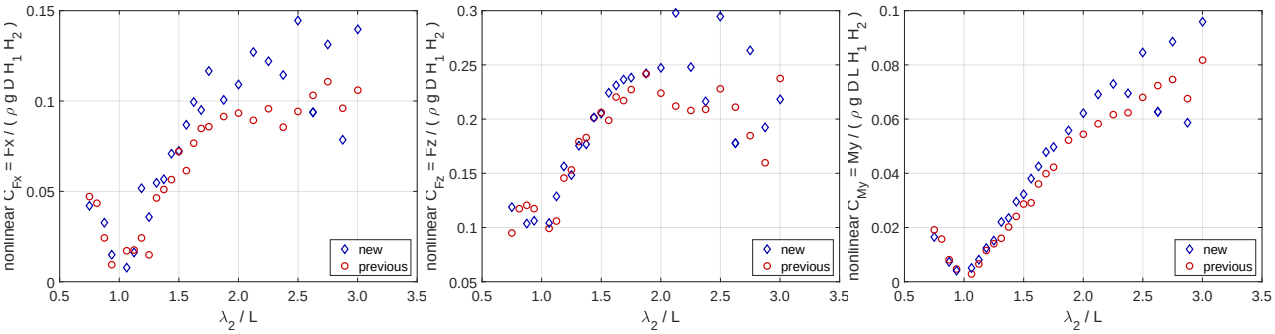

(a) F_x (b) F_z (c) M_y

Figure F.10. Comparison of measured and predicted non-dimensional non-linear force at $\lambda_1/L = 1.00; \lambda_2/L =$ various.

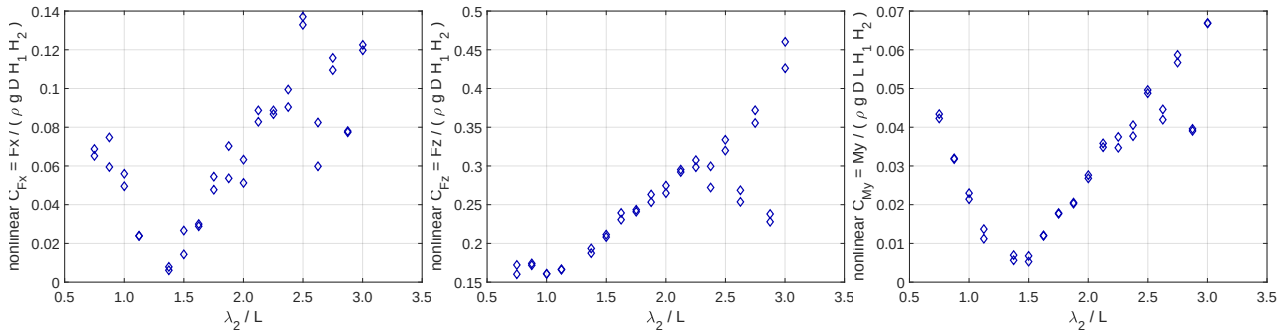

(a) F_x (b) F_z (c) M_y

Figure F.11. Comparison of measured and predicted non-dimensional non-linear force at $\lambda_1/L = 1.25; \lambda_2/L =$ various.

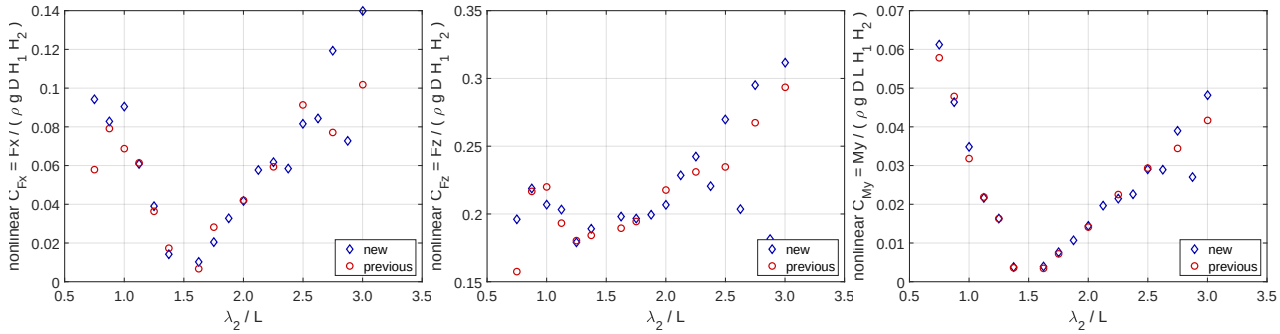

(a) F_x (b) F_z (c) M_y

Figure F.12. Comparison of measured and predicted non-dimensional non-linear force at $\lambda_1/L = 1.50; \lambda_2/L =$ various.

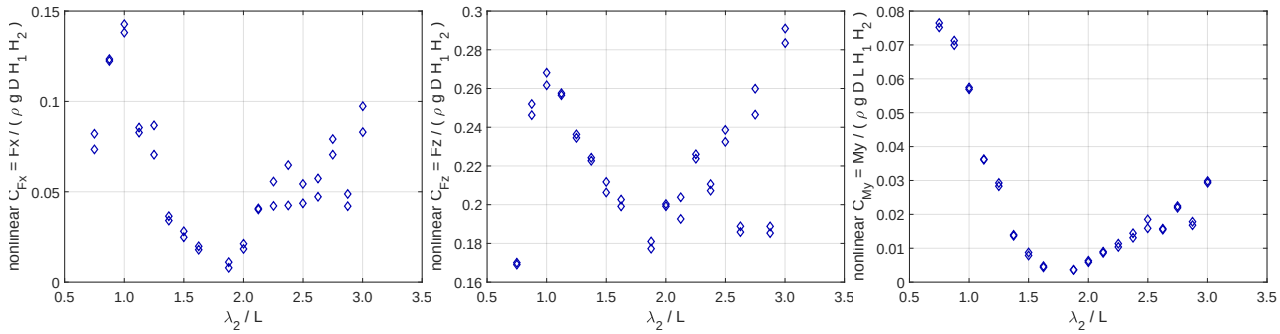

(a) F_x (b) F_z (c) M_y

Figure F.13. Comparison of measured and predicted non-dimensional non-linear force at $\lambda_1/L = 1.75; \lambda_2/L =$ various.

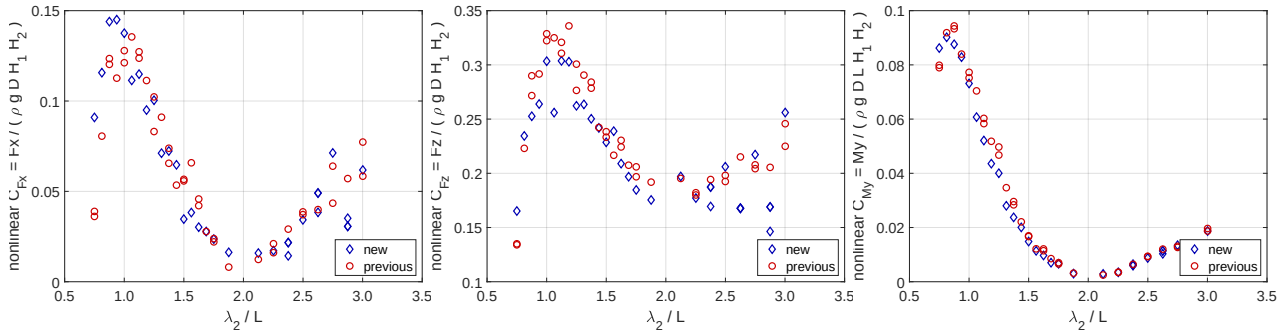

(a) F_x (b) F_z (c) M_y

Figure F.14. Comparison of measured and predicted non-dimensional non-linear force at $\lambda_1/L = 2.00; \lambda_2/L =$ various.

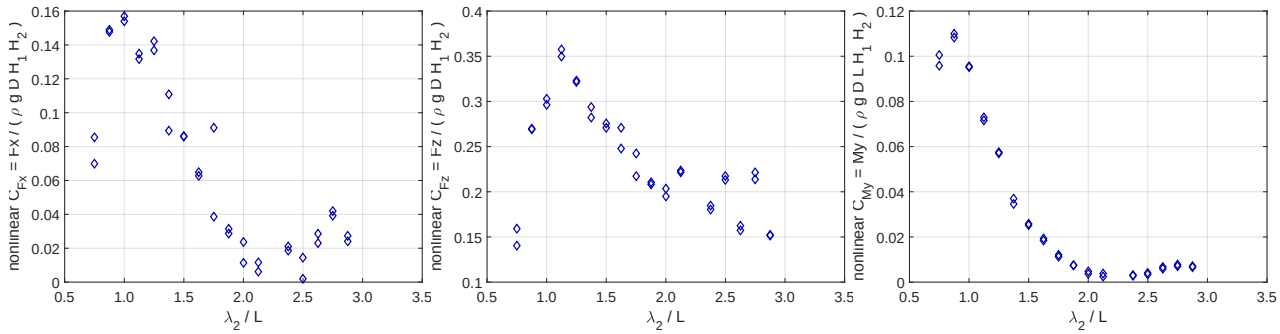

(a) F_x (b) F_z (c) M_y

Figure F.15. Comparison of measured and predicted non-dimensional non-linear force at $\lambda_1/L = 2.25; \lambda_2/L =$ various.

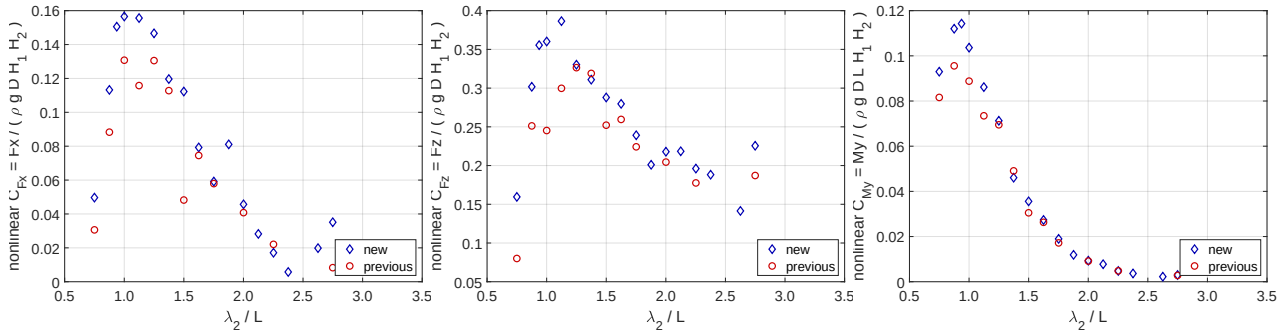

(a) F_x (b) F_z (c) M_y

Figure F.16. Comparison of measured and predicted non-dimensional non-linear force at $\lambda_1/L = 2.50; \lambda_2/L =$ various.

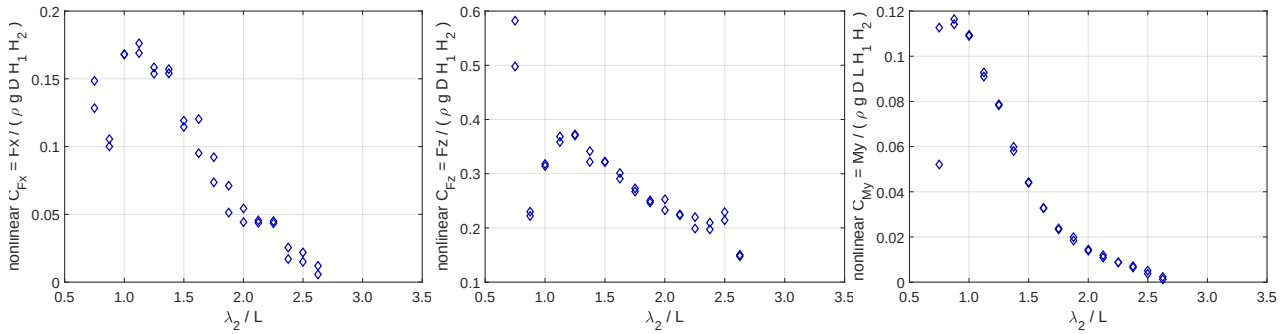

(a) F_x (b) F_z (c) M_y

Figure F.17. Comparison of measured and predicted non-dimensional nonlinear force at $\lambda_1/L = 2.75; \lambda_2/L =$ various.

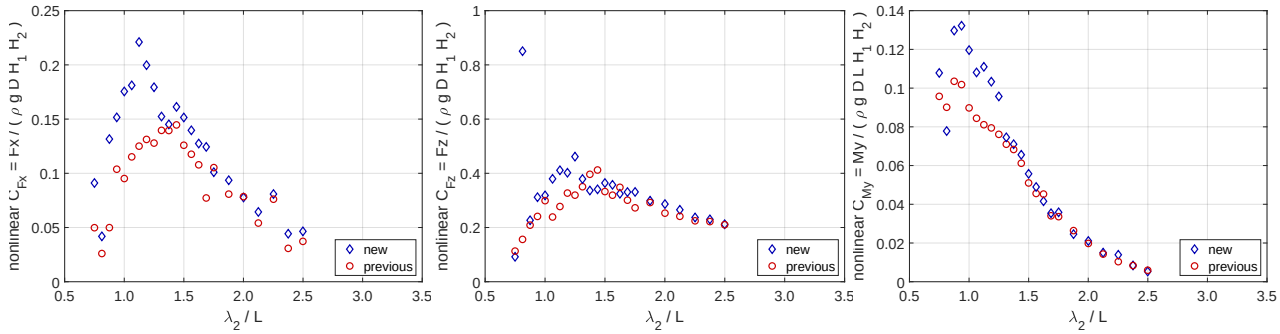

(a) F_x (b) F_z (c) M_y

Figure F.18. Comparison of measured and predicted non-dimensional nonlinear force at $\lambda_1/L = 3.00; \lambda_2/L =$ various.

THIS PAGE INTENTIONALLY LEFT BLANK

APPENDIX G:
Comparison of Linear and Nonlinear Load Results from the Baseline and Large Wave Environments

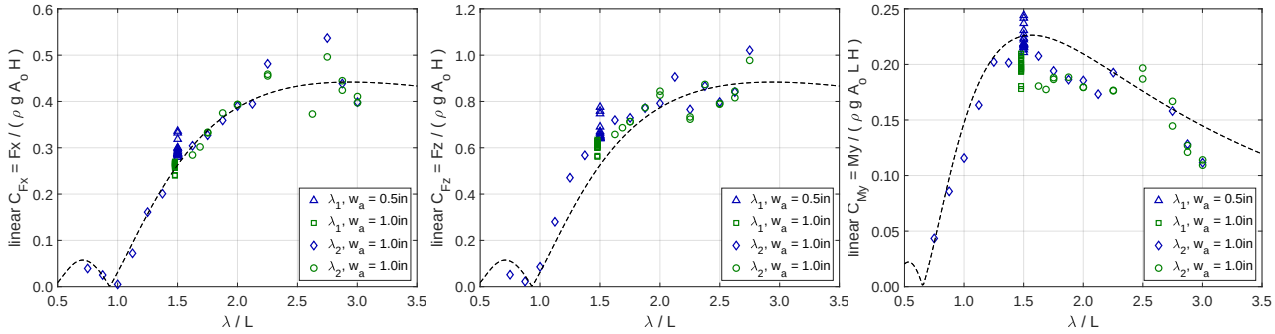

(a) F_x (b) F_z (c) M_y

Figure G.1. Comparison of measured and predicted non-dimensional linear 0.5 inch and 1.00 inch wave amplitude results at $\lambda_1/L = 1.50; \lambda_2/L =$ various.

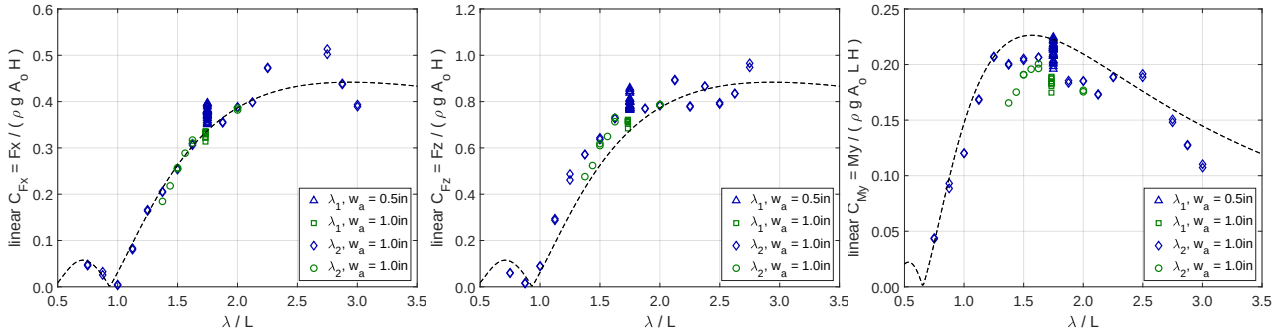

(a) F_x (b) F_z (c) M_y

Figure G.2. Comparison of measured and predicted non-dimensional linear 0.5 inch and 1.00 inch wave amplitude results at $\lambda_1/L = 1.75; \lambda_2/L =$ various.

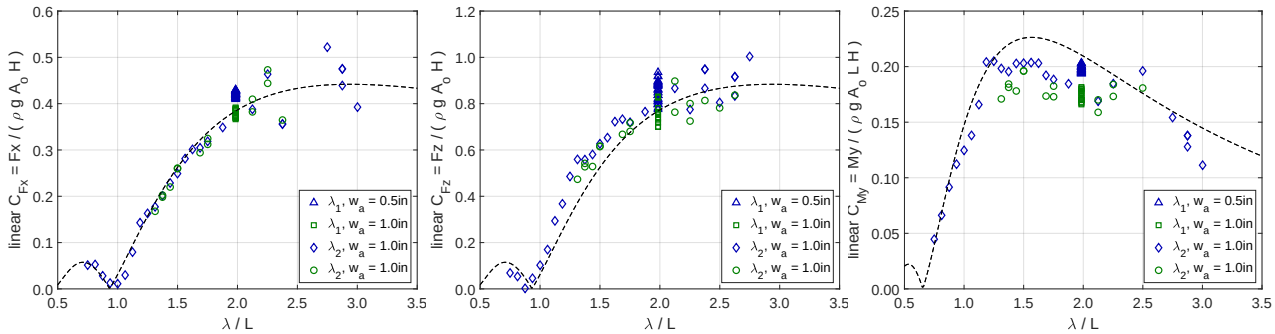

(a) F_x (b) F_z (c) M_y

Figure G.3. Comparison of measured and predicted non-dimensional linear 0.5 inch and 1.00 inch wave amplitude results at $\lambda_1/L = 2.00; \lambda_2/L =$ various.

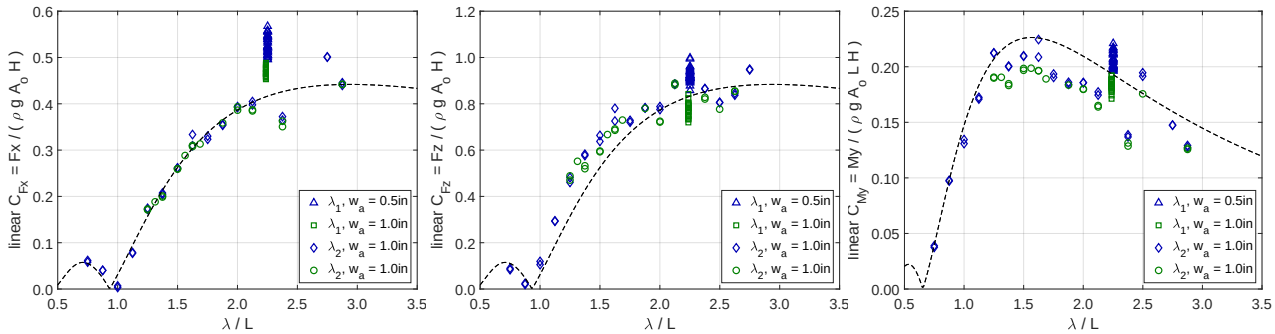

(a) F_x (b) F_z (c) M_y

Figure G.4. Comparison of measured and predicted non-dimensional linear 0.5 inch and 1.00 inch wave amplitude results at $\lambda_1/L = 2.25; \lambda_2/L =$ various.

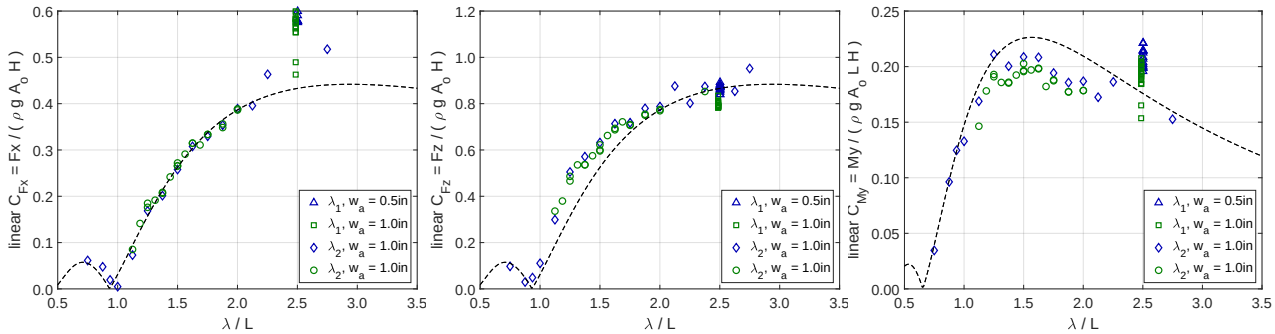

(a) F_x (b) F_z (c) M_y

Figure G.5. Comparison of measured and predicted non-dimensional linear 0.5 inch and 1.00 inch wave amplitude results at $\lambda_1/L = 2.50; \lambda_2/L =$ various.

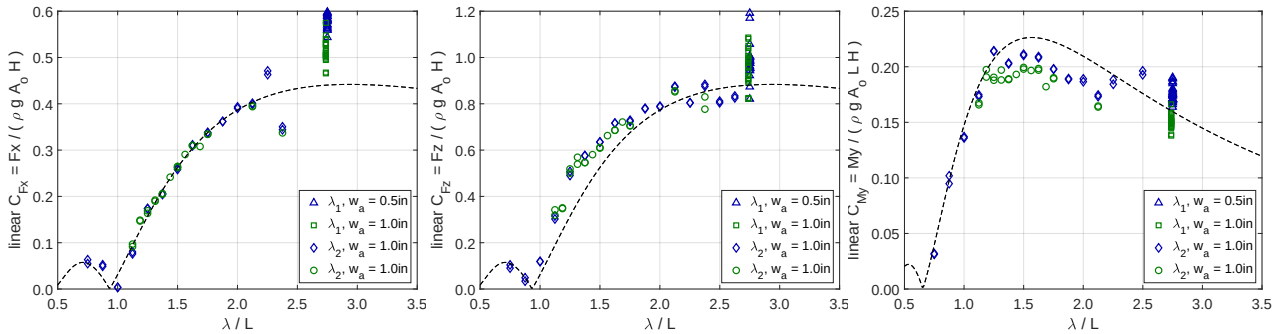

(a) F_x (b) F_z (c) M_y

Figure G.6. Comparison of measured and predicted non-dimensional linear 0.5 inch and 1.00 inch wave amplitude results at $\lambda_1/L = 2.75; \lambda_2/L =$ various.

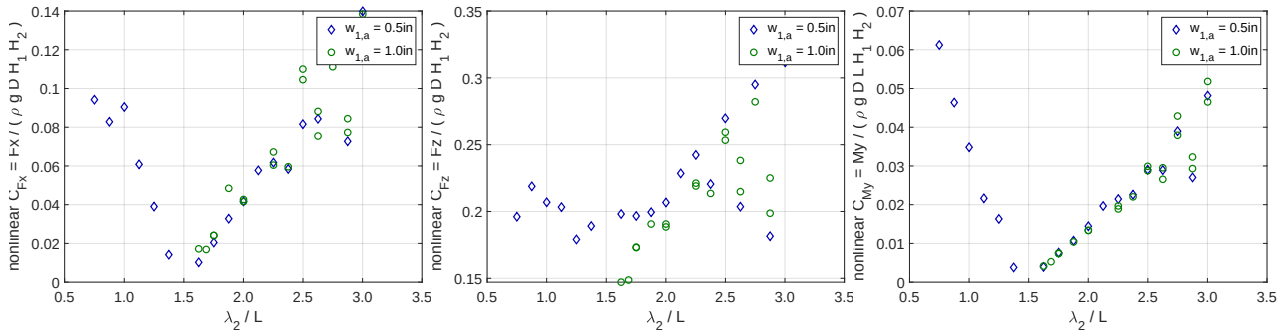

(a) F_x (b) F_z (c) M_y

Figure G.7. Comparison of measured non-dimensional nonlinear 0.5 inch and 1.00 inch wave amplitude results at $\lambda_1/L = 1.50; \lambda_2/L =$ various.

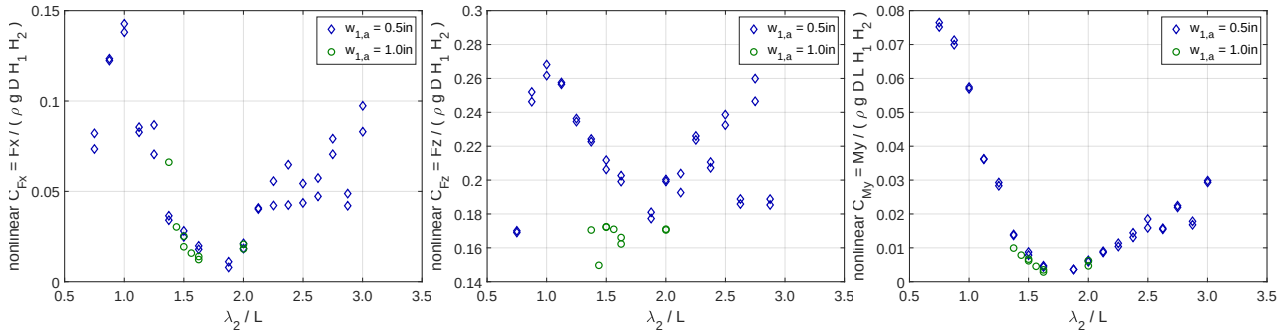

(a) F_x (b) F_z (c) M_y

Figure G.8. Comparison of measured non-dimensional nonlinear 0.5 inch and 1.00 inch wave amplitude results at $\lambda_1/L = 1.75; \lambda_2/L =$ various.

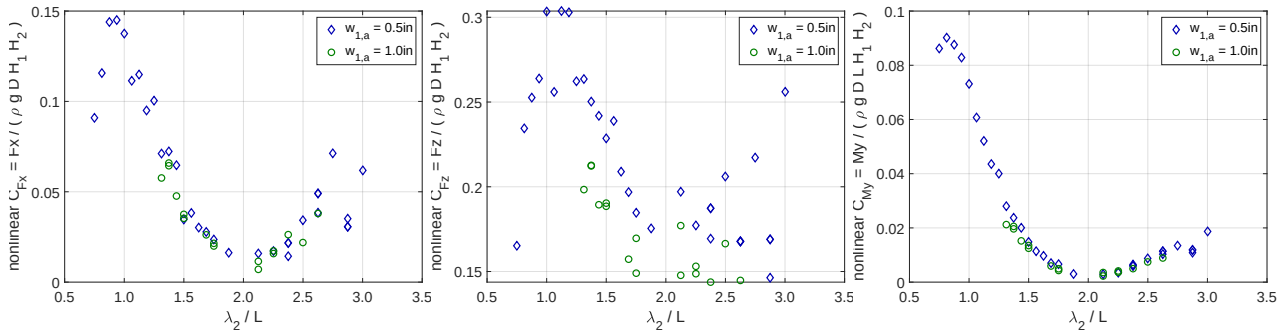

(a) F_x (b) F_z (c) M_y

Figure G.9. Comparison of measured non-dimensional nonlinear 0.5 inch and 1.00 inch wave amplitude results at $\lambda_1/L = 2.00; \lambda_2/L =$ various.

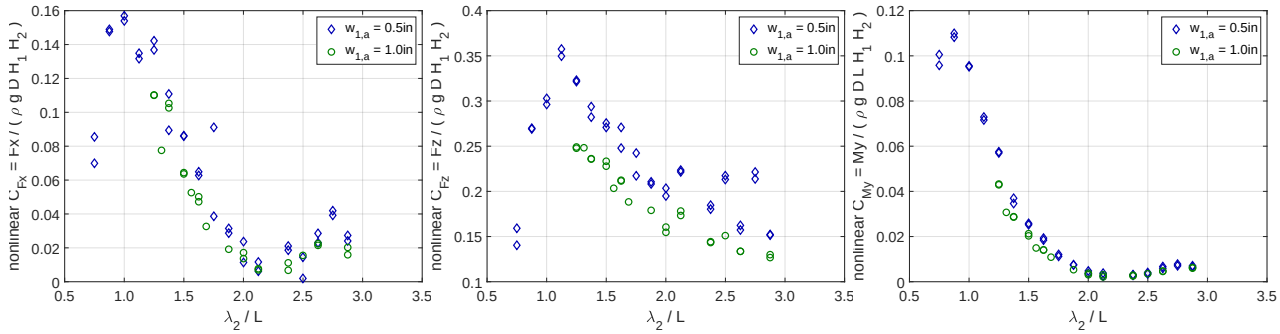

(a) F_x (b) F_z (c) M_y

Figure G.10. Comparison of measured non-dimensional nonlinear 0.5 inch and 1.00 inch wave amplitude results at $\lambda_1/L = 2.25; \lambda_2/L =$ various.

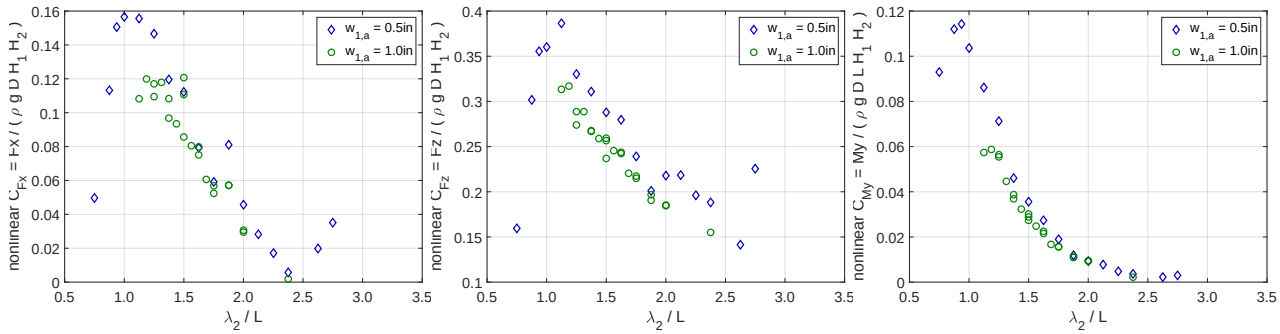

(a) F_x (b) F_z (c) M_y

Figure G.11. Comparison of measured non-dimensional nonlinear 0.5 inch and 1.00 inch wave amplitude results at $\lambda_1/L = 2.50; \lambda_2/L =$ various.

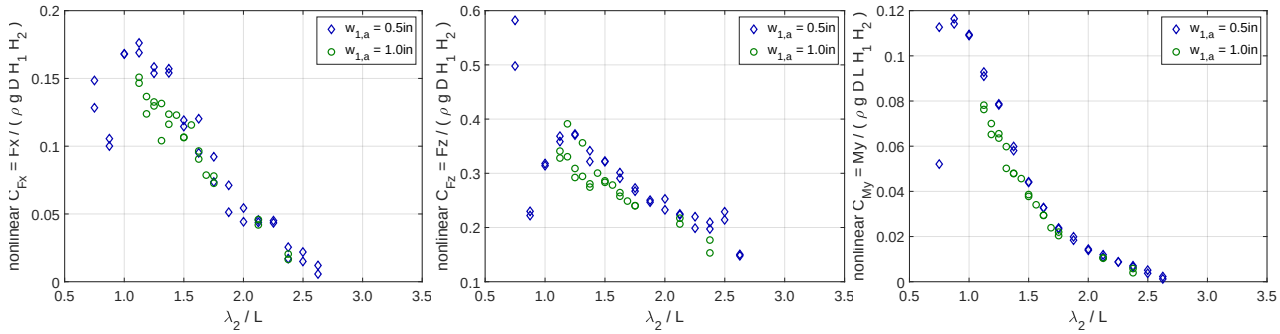

(a) F_x (b) F_z (c) M_y

Figure G.12. Comparison of measured non-dimensional nonlinear 0.5 inch and 1.00 inch wave amplitude results at $\lambda_1/L = 2.75; \lambda_2/L =$ various.

APPENDIX H:
Results of Non-dimensional Nonlinear Forces vs. Frequency differences in Large Wave Environments

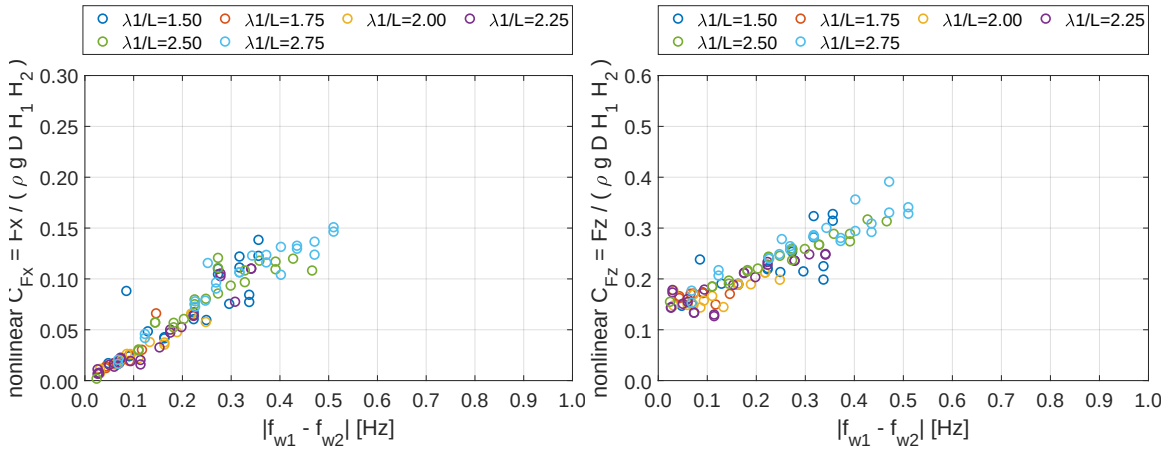

(a) F_x

(b) F_z

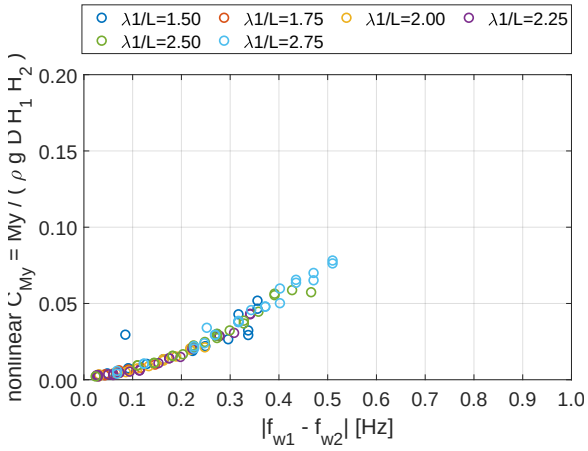

(c) M_y

Figure H.1. Results of non-dimensional nonlinear forces vs. frequency differences at various wavelengths for 0.5 inch amplitude waves.

THIS PAGE INTENTIONALLY LEFT BLANK

List of References

[1] P. Crossland, "Profiles of excess mass for a generic submarine operating under waves," Pacific 2013 International Maritime Conference, QinetiQ Ltd, UK, 2013.

[2] G. M. Khalil, "Experimental investigation of wave forces on submerged horizontal cylinders," *Indian Journal of Engineering and Materials Sciences*, vol. 8, pp. 59–65, April 2001.

[3] A. Whitmer, "Predicting wave-induced loads in complex seaways on shallowly submerged vessels," M.S. thesis, Dept. of Mech. Eng., Naval Postgraduate School, Monterey, CA, 2018 [Online]. Available: https://hdl.handle.net/10945/59622.

[4] W. Cummins, "Hydrodynamic forces and moments acting on a slender body of revolution moving under a regular train of waves," David W. Taylor Model Basin, Washington D.C., Tech. Rep. 910, December 1954.

[5] A. R. Whitmer, J. T. Klamo, and Y. W. Kwon, "On the validity of predicting wave-induced loads on a submerged body using the superposition of regular wave results," in *OCEANS 2019 MTS/IEEE SEATTLE*, 2019 [Online]. Available: DOI:10.23919/OCEANS40490.2019.8962807

[6] B. L. Hermsen, "Analysis of wave-induced forcing on a submerged body at various pitch angles," M.S. thesis, Dept. of Mech. Eng., Naval Postgraduate School, Monterey, CA, 2020 [Online]. Available: http://hdl.handle.net/10945/65544.

[7] J. T. Klamo, T. M. Turner, C. Y. Cool, K. I. Yeager, and Y. W. Kwon, "On the accuracy of an analytical solution to model wave-induced loads on an underwater vehicle in real-time," *Journal of Offshore Mechanics and Arctic Engineering*, vol. 143, no. 031202-1, June 2021 [Online]. DOI: 10.1115/1.4049119.

[8] T. M. Turner, J. T. Klamo, and Y. W. Kwon, "Comparison of wave-induced loads on a near surface slender body from inviscid flow linear solution and an experimental model test," in *Proceedings of the 37th International Conference on Ocean, Offshore, and Arctic Engineering*, Madrid, Spain, Jun 2018, vol. 7A: Ocean Engineering, p. V07AT06A015; 13 pages.

[9] J. T. Klamo, K. I. Yeager, C. Y. Cool, and T. M. Turner, "The effects of cross-sectional geometry on wave-induced loads for underwater vehicles," *IEEE Journal of Oceanic Engineering*, vol. 46, no. 3, pp. 765–784, July 2021.

[10] Y. J. Cho, W. Seok, K. Cheon, and S. H. Rhee, "Maneuvering simulation of an x-plane submarine using computational fluid dynamics," *Naval Architecture and Ocean Engineering*, vol. 12, pp. 843–855, October 2020.

[11] M. Hayatdavoodi and R. C. Ertekin, "Nonlinear forces on a submerged, horizontal plate: The g-n theory," 2012 [Online]. Available: http://www.iwwwfb.org/Abstracts/iwwwfb27/iwwwfb27_19.pdf

[12] R. C. Ertekin, "Soliton generation by moving disturbances in shallow water: Theory, computation and experiment," Ph.D. dissertation, University of California at Berkeley, Berkeley, CA, USA, 1984.

[13] R. C. Ertekin, W. C. Webster, and J. V. Wehausen, "Waves caused by a moving disturbance in a shallow channel of finite width," *Journal of Fluid Mechanics*, vol. 169, August 1986 [Online]. https://doi.org/10.1017/S0022112086000630.

[14] "UDW3," Advanced Mechanical Technology INC., August 23, 2016 [Online]. Available: https://www.amti.biz/

[15] J. T. Klamo, L. M. Jones, Y. W. Kwon, and J. M. Didoszak, "Upgrades to and current research efforts involving the tow tank facility at the Naval Postgraduate School," Proceedings of the 30th American Towing Tank Conference, SNAME, West Bethesda, MD, 2017.

[16] T. M. Turner, "Analyzing UUV hull cross-sections for minimizing wave loads when operating near surface," M.S. thesis, Dept. of Systems Eng., Naval Postgraduate School, Monterey, CA, 2018 [Online]. Available: https://hdl.handle.net/10945/59606.

Initial Distribution List

1. Defense Technical Information Center
   Ft. Belvoir, Virginia

2. Dudley Knox Library
   Naval Postgraduate School
   Monterey, California